Laser ablation and matter sizing

A focused view on molecules, sub-micron particles, and aerosols

Christian Prüfert

cumulative dissertation

in fulfillment of the requirements for the degree of

doctor rerum naturalium

in the subject of

Physical Chemistry

presented to the

Faculty of Science Institute of Chemistry at the
University of Potsdam, Potsdam, Germany

April 20th 2022

Reviewers: Prof. Dr. Hans-Gerd Löhmannsröben
Prof. Dr. Stefanie Sielemann
Prof. Dr. Michael Linscheid

Published online on the
Publication Server of the University of Potsdam:
https://doi.org/10.25932/publishup-55974
https://nbn-resolving.org/urn:nbn:de:kobv:517-opus4-559745

Contents

Paper

Prüfert, C; Urban, RD; Fischer, TG; Villatoro, J; Riebe, D; Beitz, T; Belder, D; Zeitler, K; Löhmannsröben, HG; *In situ monitoring of photocatalyzed isomerization reactions on a microchip flow reactor by IR-MALDI ion mobility spectrometry*, J. Anal. Bioanal. Chem., Nov 2020, 412 (28), 7899–7911

Prüfert, C; Villatoro, J; Zühlke, M; Beitz, T; Löhmannsröben, HG; *Liquid phase IR-MALDI and differential mobility analysis of nano- and sub-micron particles*, Phys. Chem. Chem. Phys., Jan 2022, 24 (4), 2275–86

Prüfert, C; Beitz, T; Löhmannsröben, HG; *Counting and identifying metal-bearing aerosols in-flight using laser-induced breakdown spectroscopy (LIBS), laser-induced incandescence (LII) and optical imaging*, Spectrochim. Acta B, Apr 2022, *submitted*

Zühlke, M; König, J; **Prüfert, C**; Sass, S; Beitz, T; Löhmannsröben, HG; Raddatz, CR; Zimmermann, S; Urban, RD; Warneke, J; Abel, B *Electrospray mediated Mannich reaction*, *manuscript*

Conference talks

2022 - Mar	Anwendertreffen Ionenmobilitätsspektrometrie, Unna, Germany *Acceleration of Mannich reaction in electrospray droplets*
2021 - Mar	Anwendertreffen Ionenmobilitätsspektrometrie, virtual *IR-MALDI als alternative Ladungsquelle für die differentielle Mobilitätsanalyse (DMA) von Nanopartikeln*
2019 - Sep	World of Nanoparticles, Vienna, Germany *IR-MALDI coupled differential mobility analysis (invited)*
2019 - Jul	International Society of Ion Mobility Spectrometry, Hanover, Germany *Online-monitoring of a photo-activated isomerisation in a microfluidic reactor by IR-MALDI-ion mobility spectrometry*
2018 - Mar	Anwendertreffen Ionenmobilitätsspektrometrie, Reutlingen, Germany *Characterisation of nanoparticle size distributions by IR-MALDI DMA*
2018 - Jul	International Society of Ion Mobility Spectrometry, Calgary, Canada *Differential mobility analysis of bionanoparticles and synthetic polymers*

Conference posters

2021 - Jul Euro-Mediterranean Symposium on Laser-Induced Breakdown Spectroscopy, Gijon, Spain
Characterization of industrial aerosol particles (poster price

2020 - Sep European Aerosol Conference, virtual
IR-MALDI as charging source for differential mobility analysis of nanoparticles

2019 - Sep World of Nanoparticles, Vienna, Germany
IR-MALDI coupled differential mobility analysis

2019 - Aug Eurpean Aerosol Conference, Gothenburg, Sweden
Nanoparticle characterisation with IR-MALDI coupled differential mobility analysis

2019 - Jul International Society of Ion Mobility Spectrometry, Hanover, Germany
Differential mobility analysis of submicron particles using IR-MALDI as ionisation method

2019 - May Bunsentagung, Jena, Germany
Accelerated reactions in confined microenvironments

2019 - Mar Anakon, Münster, Germany
IR-MALDI as an alternative ionisation source for differential mobility analysis

2018 - Jun Aerosol Technology, Bilbao, Spain
Characterisation of nanoparticle Size Distributions by IR-MALDI DMA

2017 - Jul International Society of Ion Mobility Spectrometry, Warsaw, Poland
Nano-ESI or IR-MALDI combined with DMA to characterize Glycans and Synthetic (Bio)-Polymers

Nomenclature

α	collision integral correction factor [1]
α_{th}	thermal accommodation coefficient [1]
χ_i	mixture of composition i [1]
ΔV	difference in potential [V]
$\dot{m}$	mass flow [kg s^{-1}]
ϵ_0	dielectric constant [A s V^{-1} m^{-1}]
η	viscosity [kg m^{-1} s^{-1}]
γ_s	third spherical angle [°]
κ_B	Boltzmann constant [J K^{-1}]
λ	mean free path [m]
μ_i	chemical potential of component i [J mol^{-1}]
μ_{red}	reduced mass [kg]
ν	collision frequency [s^{-1}]
Ω	collision integral [m^2]
$\Omega_{ave}^{(1,1)}$	calculated first order approximation of the collision integral [m^2]
ρ	density [kg m^{-3}]
σ	surface tension [kg s^{-2}]
σ_{SB}	Stefan-Boltzmann constant [W m^{-2} K^{-4}]
$\mathbf{v}$	velocity vector [m s^{-1}]
θ	solid angle [°]
θ_s	first spherical geometry angle [°]
θ_T	solid Taylor cone angle [°]
ε_0	vacuum permittivity [A^2 s^4 kg^{-1} m^{-3}]
ε_λ	wavelength- dependent emissivity factor [1]
ε_φ	depth of potential well [V]
φ	potential [V]
φ_s	second spherical angle [°]
$\vec{E}$	electric field [V m^{-1}]
$\vec{E}_{DM}$	differential mobility electric field [V m^{-1}]
A	absorptance [1]
A_{ij}	$i \rightarrow j$ transition probability [1]
$a_{N,i}$	polynomial term of order i [1]
B	mobility [s kg^{-1}]
b	impact parameter [m]
b_{min}	minimum impact parameter [m]
c	concentration [mol m^{-3}]
C_C	Cunningham slip correction factor [1]
C_D	drag coefficient [1]
$C_{abs,\lambda}$	wavelength-specific absorption cross section [m^2]
c_{heat}	specific heat capacity [J kg^{-1}]
c_{rms}	mean square molecular velocity [m s^{-1}]
c_{vap}	velocity of evaporating atoms [m s^{-1}]
d_c	distance from the center [m]
D_i	diffusion coefficient of i [m^2 s^{-1}]
D_P	particle diameter [m]
d_{coll}	collision diameter [m]
e	elementary charge [C]
E_i	Energy of state i [J]
E_n	normal electric field [V m^{-1}]
E_s	tangential electric field [V m^{-1}]
E_g	energy of the gas state [J]
E_{puls}	laser puls energy [J]
$f(t)$	temporal profile of a pulse [s^{-1}]
F_0	fluence [J m^{-2}]
F_{es}	electrostatic force [N]
F_{fr}	frictional force [N]
F_{in}	inertial force [N]
G	Gibbs free energy [J]
g_i	statistical weight of i [1]

I	electric current [A]
I_{ij}^{I}	$i \rightarrow j$ transition of a neutral atom [1]
J	emission intensity [1]
J_x	momentum flux in the x-direction [kg m^{-1} s^{-2}]
J_{ion}	ion flux [m^{-2} s^{-1}]
K	ion mobility [m^2 V^{-1} s^{-1}]
L	axial length [m]
M	function with output 0 or 1 [1]
m	mass [kg]
M_g	molar weight of the gas [kg mol^{-1}]
m_P	particle mass [kg]
m_{ion}	mass of the ion [kg]
N	charge state [1]
n	number density [m^{-3}]
n^{I}	number density of state I [m^{-3}]
n^{II}	number density of state II [m^{-3}]
N_A	Avogadro number [1]
n_j	amount of substance [mol]
n_φ	order of potential [1]
P	size distribution density [m^{-1}]
p	pressure [Pa]
p_r	vapour pressure at radius r [Pa]
p_∞	vapour pressure in bulk [Pa]
q	absolute charge [C]
Q_a	aerosol gas stream [kg s^{-1}]
Q_s	sheath gas stream [m^3 s^{-1}]
q_{evap}	heat of evaporation [J]
R	radial length [m]
r	radius [m]
R_a	radius of the atom [m]
r_a	radial distance from the center of the atom [m]
R_g	universal gas constant [J mol^{-1} K^{-1}]
r_m	mean radius [m]
R_P	radius of the particle [m]
R_{th}	thermal response [1]
Re	Reynolds number [1]
Res_{Ch}	DM channel resolution [1]
T	temperature [K]
t	time [s]
T_C	critical temperature [K]
T_{eff}	effective temperature [K]
U^{I}	partition function of state I [1]
U_P	internal energy of the particle [J]
V	Volume [m^3]
v	velocity [m s^{-1}]
V_m	molar Volume [m^3 mol^{-1}]
v_{diff}	diffusive velocity [m s^{-1}]
v_{dt}	drift tube velocity [m s^{-1}]
v_{ion}	velocity of the ion [m s^{-1}]
v_{TE}	electrical terminal velocity [m s^{-1}]
W	weighing factor of DM channel [1]
z	distance orthogonal to x [m]
Z_+	positive charge fraction [1]
Z_-	negative charge fraction [1]
DM	differential mobility
ES	electrospray
IM	ion mobility
IR	infrared
LIBS	laser-induced breakdown spectroscopy
LII	laser-induced incandescence
MALDI	matrix-assisted laser desorption ionization
xES	soft X-ray coupled electrospray

Abstract

The doctoral thesis presented provides a comprehensive view of laser-based ablation techniques promoted to new fields of operation, including, but not limited to, size, composition, and concentration analyses. It covers various applications of laser ablation techniques over a wide range of sizes, from single molecules all the way to aerosol particles. The research for this thesis started with broadening and deepening the field of application and the fundamental understanding of liquid-phase IR-MALDI. Here, the hybridization of ion mobility spectrometry and microfluidics was realized by using IR-MALDI as the coupling technique for the first time. The setup was used for monitoring the photocatalytic performance of the *E*-*Z* isomerization of olefins. Using this hybrid, measurement times were so drastically reduced that such photocatalyst screenings became a matter of minutes rather than hours. With this on hand, triple measurements screenings could not only be performed within ten minutes, but also with a minimum amount of resources highlighting its potential as a green chemistry alternative to batch-sized reactions. Along the optimizing process of the IR-MALDI source for microfluidics came its application for another liquid sample supply method, the hanging drop. This demarcated one of the first applications of IR-MALDI for the charging of sub-micron particles directly from suspensions via their gas-phase transfer, followed by their characterization with differential mobility analysis. Given the high spectral quality of the data up to octuply charged particles became experimentally accessible, this laid the foundation for deriving a new charge distribution model for IR-MALDI in that size regime. Moving on to even larger analyte sizes, LIBS and LII were employed as ablation techniques for the solid phase, namely the aerosol particles themselves. Both techniques produce light-emitting events and were used to quantify and classify different aerosols. The unique configuration of stroboscopic imaging, photoacoustics, LII, and LIBS measurements opened new realms for analytical synergies and their potential application in industry. The concept of using low fluences, below 100 J/cm^2, and high repetition rates of up to 500 Hz for LIBS makes for an excellent phase-selective LIBS setup. This concept was combined with a new approach to the photoacoustic normalization of LIBS. Also, it was possible to acquire statistically relevant amounts of data in a matter of seconds, showing its potential as a real-time optimization technique. On the same time axis, but at much lower fluences, LII was used with a similar methodology to quickly quantify and classify airborne particles of different compositions. For the first time, aerosol particles were evaluated on their LII susceptibility by using a fluence screening approach.

Zusammenfassung

Die vorliegende Arbeit hat die lasergestützte Flüssig- bzw. Festphasenablation zur Molekül- und Partikelanalyse zur Grundlage. Mittels IR-Strahlung wurden die Analyten, vom molekularen bis hin zum mittleren Mikrometergrößenbereich, in die Gasphase überführt, ionisiert oder geladen und anschließend durch spektrometrische beziehungsweise spektroskopische Analysemethoden identifiziert und quantifiziert. Eingangs wurden IR-MALDIs (*infrared laser-assisted matrix dispersion ionization*) Anwendungsbereiche als Kopplungsmethode etabliert sowie fundamentale Aspekte des Ionisationsprozesses innerhalb der IR-MALDI beleuchtet. Die als Kopplungsmethode eingesetzte IR-MALDI ermöglichte die erstmalige Zusammenführung eines Mikrochip-Reaktors mit einem Niederdruck-Ionenmobilitätsspektrometer. Dies geschah über die IR-MALDI eines vom Mikrochip ejektierten Flüssigkeitsmikrostrahls und wurde für die Verlaufsbeoachtung photokatalysierter *E-Z* Olefin-Isomerisierungsreaktionen verwendet. Dieses hybride Konzept aus Mikrochip-Reaktor und Niederdruck-Ionenmobilitätsspektrometer hatte eine erhebliche Reduktion der benötigten Messzeit zur Folge, und konnte, im Vergleich zur halbtägigen Verlaufsbeobachtung von Reaktionen im Kolben, auf nur wenige Minuten verringert werden. Hiermit war es nun also nicht nur möglich Dreifachmessungen innerhalb von nur zehn Minuten auszuführen, sondern es wurde auch nur ein kleinster Bruchteil der sonst üblichen Rohstoffe benötigt, was wiederum zeigt, welches Potential diese systemische Miniaturisierung für nachhaltige Chemie hat. Entlang der Entwicklung dieser Flüssigkeitsstrahlkopplung konnte IR-MALDI auch auf einen Aufbau mit hängendem Tropfen übertragen werden. Hierdurch kam es zu einer der ersten Gasphasenanalysen von Submikron-Partikeln direkt aus einer Suspension heraus. Nachdem diese durch IR-MALDI mit entsprechender Ladung versehen wurden, konnten sie mittels differentieller Mobilitätsanalyse charakterisiert werden. Durch die hohe spektrale Auflösung der Methode war eine eindeutige Zuordnung von bis zu acht Ladungen auf einem Partikel möglich. Folglich lieferte dies die Grundlage zur Evaluierung bestehender IR-MALDI-Ladungsverteilungsmodelle und schlussendlich zur Entwicklung eines neuen Ladungsverteilungsmodels. Anschließend wurde die Ablation auf noch größere Partikel, auf denen die Ablation direkt und damit in der festen Phase stattfinden konnte, übertragen. Hierbei fanden LIBS (*laser-induced breakdown spectroscopy*) und LII (*laser-induced incandescence*) ihre Anwendung in der Aerosolquantifizierung sowie in deren Identifizierung beziehungsweise Klassierung. Die vielschichtige Methodenkonfiguration bestehend aus Stroboskopie, Photoakustik, LII und LIBS eröffnete neue Dimensionen für analytische Synergien. In diesem Zusammenhang wurde ein neuer Ansatz zur photoakustischen Normierung von Einzelsignalen in der LIBS entwickelt. Als weiteres Alleinstellungsmerkmal wurde LIBS mit niedrigen Fluenzen von unter 100 J/cm^2, somit also phasenselektiv, und hohen Wiederholungsraten von bis zu 500 Hz verwendet. Somit konnte innerhalb von Sekunden eine statistisch relevante Menge an Daten erhoben werden, nahezu in Echtzeit, was wiederum Anwendungspotentiale in Industrieprozessen aufzeigt. Auf derselben Zeitskala, jedoch bei deutlich geringeren Fluenzen (<1.5 J/cm^2), wurde auch die LII für Partikelzählung verwendet. Hierbei wurde erstmals das Potential der LII zur Klassierung von Partikeln im Rahmen eines Fluenz-Screenings gezeigt.

Acknowledgments

First and foremost, I would like to thank my supervisor Prof. Dr. Hans-Gerd Löhmannsröben for taking me under his wing, for not only being a continuous source of inspiration and advice but also providing a nurturing academic environment, where professional and constructive scientific exchange flourishes.

Special thanks go to all the *Beitz's* for years of fruitful discussions, passionate debates and formidable personal growth, both inside and outside of the work environment. My gratitude naturally also extends to all the members of the physical chemistry department. In addition, I would like to thank *Simon* for his work on spelling and grammar.

I would also like to thank Prof. Dr. Stefanie Sielemann and Prof. Dr. Michael Linscheid for being reviewers for this doctoral thesis.

Last but not least, I would like to thank all of the funding bodies, the School of Analytical Sciences Adlershof, the German Research Foundation (project FOR 2177 / 275653032), the European Regional Development Fund, the State of Brandenburg, the German Aerospace Center as part of the Federal Ministry of Education and Research (project 01DM19009A), and the DEAL project for the open access funding.

1

Introduction

1.1 Prologue

Sizing is ubiquitous in all fields of natural sciences and engineering. Size is most often perceived as the degree to which an object extends into any of the three spatial dimensions, it comes, however, in different flavors. Depending on the field and application where sizing occurs, the characteristic length, the most fundamental sizing property, can either imply an actual unit of length or be representative of an area or volume. The distinction between those three, as trivial as it seems, is by any means absolute and therefore has a variety of pitfalls and barriers that can be a great source for misinterpretation and fallacies. Size and sizing on its own does not impart any physical meaning if the method with which the size was determined isn't implicitly or explicitly mentioned. This is ever so important for the analysis of aerosols, nanoparticles and single molecules, where the intuitive ruler-size maxim breaks down. Here, size cannot be determined as a static, ruler-like concept but is the result of an equilibrium of forces acting upon the measured object. Because of these forces, size then becomes a convolute of principles which are often multidimensional in their own right. Therefore, size is an inherently multidimensional descriptor rather than just a number multiplied by a length unit. The two realms presented in this thesis will mainly focus on drag forces that involve cross section properties of molecules, nanoparticles and aerosols. Molecular size is mostly presented as a collision cross section, thus a true area unit. Nanoparticle or aerosol size is usually presented in units of lengths, such as diameter, although measured by cross section-based methods and sometimes even represented as a volume/mass ratio, such as PM10. This short list already shows that great care must be taken when talking about sizes and especially so, when relating, correlating or comparing sizes determined by different techniques and therefore, potentially, vastly different physical principles.

1.2 Motivation

Minor, Citius, Vidirius - smaller, faster, greener is the potentially best way to summarize the contemporary trends in science, and most notably in physical chemistry. Keywords like microreactor, nanomaterials and sustainability are omnipresent in research activities in all chemical genres, pushing innovations ever closer to limits of what is possible chemically, but also physically, nearing universal limitations. In the realm of that endeavor, the last decade has spawned great advances in preparative miniaturization, prompt analytics and automation procedures. [1–7] The field of microfluidic chemistry emerged from these trends in the early 1990s, and underwent great progress perennially implementing more techniques and features onto a single microfluidic device. This microfluidic device, a so-called microchip or lab on a chip (LOC), can be made from silicon, quartz, metals, polymers, ceramics or glass. [8–10] Structural elements such as tightly meandering channels, dead volume-free mixing junctions and optically transparent high pressure-resistant materials have been developed onto the LOC. [11] Increments in compactness and fineness come at the exceedingly high cost of labor-intense manufacturing, increased back-pressure effects and elevated risks of clogging. This, of course, also holds for on-chip functionalities, such as separation techniques, electrode bio-sensing or application-tailored surface modifications. [12–15] To do justice to the chemical engineering ingenuity, seamless coupling of LOCs to analytical techniques is key. The coupling of preparative LOC has recently also been advanced because single-cell as well as single-droplet analysis on and from these LOCs has come into focus. [16, 17] Advantages such as swift changes in reaction conditions, precise reaction time and resource rationing and instantaneous analysis, paved the way for using LOCs as high-throughput screening techniques. For this electrical sensors have often been employed given their ability to detect quickly. [18, 19] Implementing gas-phase transfer and ionization onto LOCs, so that they are compatible with techniques such as mass spectrometry (MS) and ion mobility (IM) spectrometry, comes with its own challenges. [20] Here, electrospray (ES) is the most widely used method given its gentle gas-phase transfer and soft ionization, making it the gold standard ionization technique for IM spectrometry and MS. ES often requires a high potential at the microfluidic device and a narrow emitter tip to achieve this gas-phase transfer and ionization. This is where practical limitations arise, however hyphenations with other techniques has been achieved in multiple variations. [16, 21, 22] The second, even softer, ionization technique routinely used for MS or IM spectrometry is the matrix-assisted laser desorption ionization (MALDI). It can be employed with a wide range of laser light sources, and if carried out with infrared (IR) light, it is referred to as IR-MALDI. Because it disperses and ionizes in a fully laser-based manner, thus operates electric field-free and on any type of surface, none of the ES restrictions apply here per se. For a near real-time measurement, however, a free-standing liquid beam being ejected from the LOC has proven most practical. Although IR-MALDI is found in- and outside the microfluidics community, little is actually known about the charge generation and evolution process of it. Studies on that have been scarce at best and therefore, charging models are also seldom presented in literature. [23–26] This lack of knowledge naturally also extends to the sub-micron particle size regime, although IR-MALDI bears great potential being virtually free of any particle size limitations. Exploring this charging process to deepen the understanding of IR-MALDI on a fundamental physicochemical level is therefore needed. At the same time, research work done in the sub-micron size regime would reveal the practical particle size limitations of such a model. It could be then be implemented in charge state correction algorithms for absolute quantification measurements, which are routinely used in commercially available sizing techniques. [27] At this point, although the transition from continuous process

monitoring to automated (industry 3.0) or autonomous (industry 4.0) systems seems self-evident, it remains a great challenge. This is because of the application's high dimensionality, a well-known issue in all genres of artificial intelligence and machine learning. The overarching consensus, however, is the vast amount of data required to achieve such goals. In industry, especially in ones operating in harsh conditions, such as metallurgy, requirements for measurement techniques are high and thus data is scarce. In fact, because of the harsh conditions, only contactless methods are feasible for in-line and real-time measurements, both essential for a real-time optimization. Flame IR-pyrometry and laser-based techniques are one of the few process analytics used in, for example, blast furnaces. [28–30] Here, the most commonly used laser-based technique is laser-induced breakdown spectroscopy (LIBS) because it operates from a distance, does not require any sample preparation, works exceptionally well on metals and has a high automation potential. [31–38] While all these advantages are practical and promising, the one great challenge in LIBS persists, achieving calibration-free LIBS. This is primarily due to LIBS being inevitably sensitive to matrix effects. In metallurgy, these matrix effects include, but are not limited to, the amount and composition of the mineral and gangue and the quality of the plasma. Although machine learning and deep neural networks have been explored in most recent years to enhance the practicality of the data, they do not, in any way, foster the analytical understanding of LIBS or of the plasma. [39–41] This is also why they hardly ever help by identifying or quantifying single component matrix effects nor by diagnosing the plasma itself. Only a comprehensive set of complementing analytical techniques would expand the parameter space to a degree that such conclusions could possibly be drawn. [42] One of them is photoacoustics. In photoacoustics the amplitude of the shock wave produced by a single LIBS event is recorded. This holds information on how much material was involved in the formation of the plasma for this individual event. [43–46] Event though this is valuable information, it is somewhat non-specific in its nature and prone to noise. This is probably also why it hasn't found its way into process analytics, yet advances in acoustic signal deconvolution are on their way. Until then, better, for example photoacoustic normalization methodologies, will be needed to put these acoustic signals to use. Related to LIBS, however, working at lower fluences, there is laser-induced incandescence (LII). It comes with the same practical advantages as LIBS, however, with a lower analytical specificity. This is because the incandescence susceptibility of a particle is more of an ensemble property than the LIBS signals defined by atomic emission lines. This comes with the advantage that LII does contain size information, information principally inaccessible by LIBS. In time-resolved LII (TiRe-LII) the signal decay is, among other parameters, proportional to the size of the particle and can thereby be used not to determine the size either of a single particle or the size distribution of an entire particle population. So, in a nutshell, material identification in LII is based on incandescence susceptibility and sizing on time-resolved LII measurements. [47–52] It therefore provides a viable addition to LIBS.

The doctoral thesis presented addresses and aims to partially solve the issues stated above. This ranges from laser ablation of liquid matrices all the way to solid particulate matter ablation. Likewise, the employed sizing techniques range from ion mobility for single molecules to stroboscopic imaging of 100 µm particles. The laser ablation of liquids was realized by using IR-MALDI for a microbeam demonstrating a novel hyphenation technique between a microfluidic device and a reduced-pressure ion mobility spectrometer for ionizing and size-discriminating enantiomer pairs. Hereafter, the liquid-phase ablation with IR-MALDI was proceeded in a hanging-drop setup, rendering the first application of sub-micron particle ionization with IR-MALDI. In this context charging models of IR-MALDI were critically reviewed, eventually leading to a

newly derived charge distribution model for IR-MALDI for the sub-micron size range. The laser ablation technique was then adapted, so it can be applied to solid, airborne non-soot particles by using low pulse fluences and high repetition rates yielding a phase-selective version of LIBS (PS-LIBS). Additionally PS-LIBS was accompanied by stroboscopic and CCD imaging, as well as light scattering, photodiode and photoacoustic detection methods to form a comprehensive set of airborne particle analyses, complementing each others analytical information. Also, a refined photoacoustic normalization procedure for PS-LIBS emerged from the photoacoustic measurements in this work. Proceeding to even lower fluences, LII was used for standard quantification of the non-soot particles, however, throughout the course of the work, demonstrated an LII specificity of unexpectedly high quality. A discovery finding its way into a all new fluence screening application for the classification of airborne particles.

2

Theory

2.1 Dispersion and charging

For the characterization of the native state of molecules, nanoparticles, and aerosols it is important to reduce the number and the nature of interactions with surrounding matter as much as possible. This process is known as gas-phase transfer and can be achieved by using a variety of dissipation methods. For liquids, these are usually sprays [53, 54] or nebulizers [55], and for powders, dispersers or dust generators. Although the gas phase comprises gas-phase interactions, these are most infrequent compared to their condensed-phase counterparts. For ion-based analytical methods, ubiquitous in analytical chemistry, these species also require non-zero net charges. These can either be obtained during the dispersion process or thereafter. The most common soft ionization techniques for simultaneously dispersing and charging species are electrospray (ES) ionization and matrix-assisted laser dispersion (MALD) ionization. They will be addressed in the first two sections. The third section covers a gas- or aerosol-charging technique, the bipolar charger or neutralizer, that requires prior dispersion.

Soft ionization Soft ionization is an umbrella term for charging samples that retain the original, or native, conformational information and avoid fragmentation as much as possible. This is achieved by ionizing the surrounding matrix or gases, rather than the analyte itself. After that ionization, the charge is transferred to the species of interest, either via a charge-transfer reaction or by adduct formation. By doing so, soft ionization directs the conformationally disruptive ionization process away from the analyte. Electrospray (ES) ionization and infrared matrix-assisted dispersion ionization (IR-MALDI) are both preluded by extreme conditions that exceed the coherent forces within the liquid, eventually dispersing it. Therefore, ionization and dispersion occur almost simultaneously with the former enabling the latter. These two soft ionization techniques are especially relevant for biochemical and bimolecular structural investigations because it is

vital that they maintain their structural integrity over a vast parameter space, as found, for example, in proteomics, glycomics or proteoglycomics.

2.2 Electrospray

The electrospray (ES) is an ionization and dispersion technique that has been subject to electrochemical, fluid dynamics, and analytical studies as can be been seen in numerous papers, reviews, and books over the last decades. [56] Although pioneered in 1989 by Fenn et al. [57, 58] and brought to the masses by Kebarle et al. [59] in the early 1990s, research on the mechanistic details of ES continues to this day, where recent focus is put on cluster chemistry [60, 61] well as on using ES droplets as micro-reaction vessels. [62]

Briefly, ES is based on oxidation and reduction reactions [63, 64] that take place at the tip of an emitter or counter electrode under high-voltage. The voltage shapes the emitted liquid, balanced by the adhesive effects within it and by the repulsive effects due to the charges contained in the liquid along the surrounding electric field, as illustrated in Fig. 2.1.

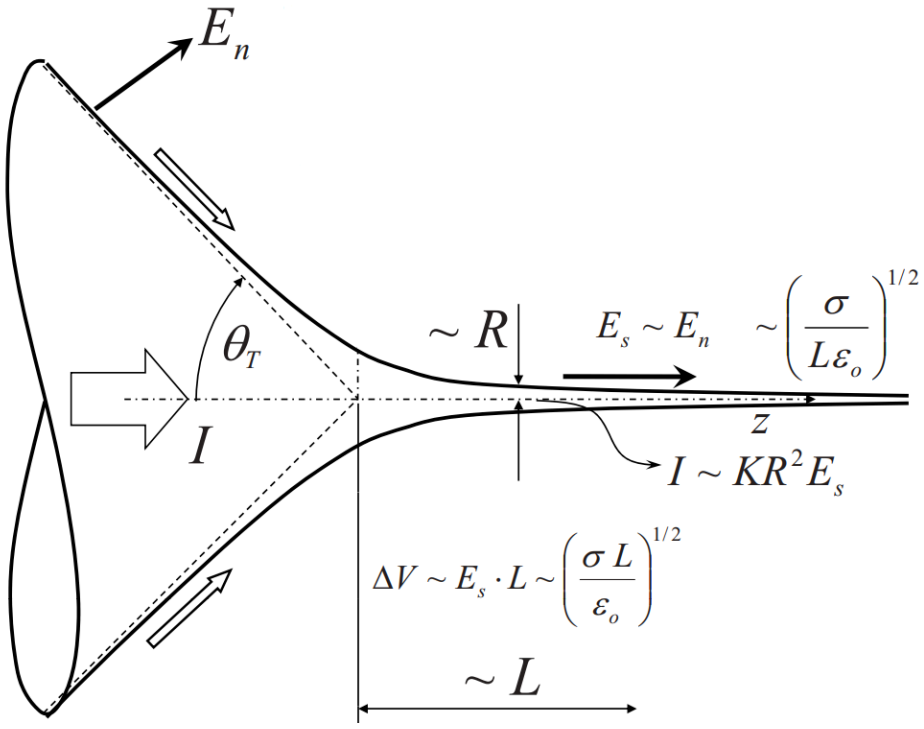

Figure 2.1: Summary scheme illustrating the electric forces E_s, E_n, ΔV (potential), liquid properties σ, K for the filament dimensions R, L with a total ion current (I), all within the Taylor cone, adapted from [65].

This balance defines the characteristic solid angle θ of the cone, most notably the Taylor cone $\theta_T = 49.3°$. [66] As the electric field becomes more tangential, the tangential electric field E_S breaks even with the normal electric field E_n at the Taylor solution for the equilibrium between these two. This equilibrium also depends

on the surface tension σ and the characteristic axial length L, see Eqn. (2.1).

$$E_S \propto \sqrt{\frac{\sigma}{\varepsilon_0 L}} \tag{2.1}$$

The electric current I in this region depends on the cross-sectional area R^2, the electric conductivity K, and the tangential electric field E_s that is pulling the charges out of the cone, forming the liquid filament. This is accompanied by a potential drop ΔV along this filament. The free-standing liquid filament eventually disintegrates to form primary droplets. [59] These droplets eject ever smaller offspring droplets, daughter droplets, a process called Coulomb fission cascade. Here, the offspring droplets are smaller than 100 nm and contain hundreds of charges[1], which are thought to be originating the charges for the gas-phase ions of interest. [59, 67, 68] Combining ES with bipolar chargers or neutralizers, the so-called soft X-ray ES (xES) drastically reduces that charge density and prevents the Coulomb fission cascade, opening the doors to investigate large suspended particles or to use the primary ES droplets themselves.

2.3 Infrared matrix-assisted laser desorption ionization

Infrared matrix-assisted laser dispersion ionization (IR-MALDI) of liquids uses the high fluence of focused laser light to create a thermal- and stress-confined region to create a supercritical state. The thermal and stress confinement in that region, a regime wherein energy is absorbed faster than it dissipates through the surrounding phase, abruptly promotes the liquid phase to that supercritical state, the spinodal, from where it relaxes into two phases – liquid and vapor – by phase explosion. During that phase explosion, the solvent, analytes and accompanying charges are ejected and redistributed in much smaller sub-volumes or droplets, a stroboscopically visible process. [69, 70]

The following section aims to introduce and justify the concept of spinodals along the lines of the Gibbs free energy, setting it apart from nucleation modes, showing how a spinodal decomposition is realized by using IR-MALDI, its resulting dispersion and charging of the species of interest.

2.3.1 Spinodal decomposition

A phase explosion is a distinct case of the spinodal decomposition where the decomposition occurs from the liquid to the vapor phase and is accompanied by a drastic increase in volume. All spinodal decompositions have the same underlying thermodynamic principles and, in contrast to nucleation-mode processes, occur uniformly across the entire systems. This is illustrated below, where the spatial distribution of three different compositions χ_0, χ_1, and χ_2 are shown over four points in time.
In the nucleation mode, as time progresses, a uniform composition χ_0 separates at distinct points of nucleation into χ_2, directly surrounded by a χ_1 phase, creating an extreme concentration gradient, whereas the remaining material farther away only gradually approaches χ_1 as the areas of χ_2 expand over time. The composition changes along the concentration gradient (A in Fig. 2.2), until coalescence takes over, leading to a sudden change in composition and the expansion of the areas with composition χ_2. Here, coalescence causes the retention of the concentration gradient until the entire system is in composition χ_1 or χ_2, as shown in Fig. 2.2. [71]

[1] The Rayleigh limit for a water droplet of 100 nm diameter is about 1400 elementary charges.

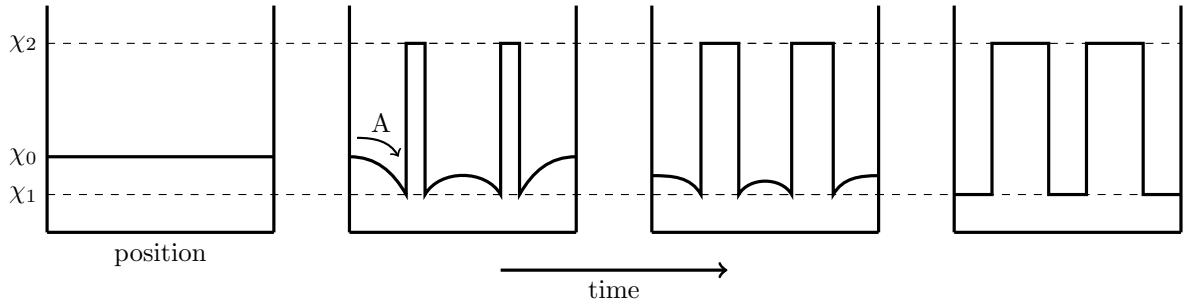

Figure 2.2: Four points in time for the progression of a nucleation-driven phase separation starting at nucleation sides that grow outwards from the inside, retaining the concentration gradient and sharp concentration edge, reconstructed from [71].

For the case of spinodal decomposition, illustrated in Fig. 2.3, the Gibbs free energy G is also reduced, however, contrary to nucleation, the composition changes gradually and against the concentration gradient (B in Fig. 2.3). [72] Because the entire system change follows that process simultaneously, no localized jumps occur in the composition. Only in the end, when the entire system is fully divided among these sections of composition χ_1 and χ_2, does a sharp border appear.

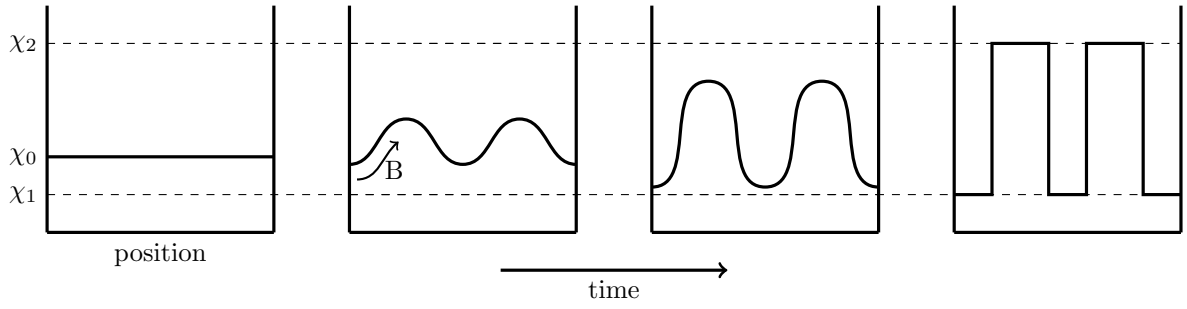

Figure 2.3: Four points in time for the progression of a spinodal-driven phase separation occurring simultaneously over the entire system and against the concentration gradients without sharp concentration edges, reconstructed from [71].

The spinodal decomposition was first described by Kauzmann in 1948 [71, 73] for glass mixtures and alloys and later refined by Hillert [74]. It thus has its origin in metallurgy. Spinodal decomposition manifests itself experimentally as part of the miscibility gaps, or along the locus of temperature extrema ($T < T_C$) on the pressure-volume-temperature (p-V-T) surface, in-between these extrema, in which improper change of state would arise because $\partial p/\partial V > 0$, see Fig. 2.4. In all three plots, the spinodals mark the border between the (meta-)stable and unstable states of the system.

A spinodal decomposition occurs under a constant decrease of the system's free energy and is thus entirely spontaneous. Although counter-intuitive at first, this includes processes against the concentration gradient. All mixtures that exhibit a negative curvature in the G-χ_B plane for an isobar isotherm, [71, p. 304] and can therefore exhibit a miscibility gap, are eligible for a spinodal decomposition. One way of formalizing that

negative curvature is via Eqn. 2.2.

$$\left.\frac{\partial^2 G}{\partial \chi_B^2}\right|_{p,T} < 0 \tag{2.2}$$

They contain at least two free energy minima, $\partial G/\partial\chi_B = 0$, $\partial^2 G/\partial^2\chi_B > 0$, one maximum with $\partial G/\partial\chi_B = 0$, $\partial^2 G/\partial^2\chi_B < 0$, and two points of inflection, $\partial G/\partial\chi_B = 0$, $\partial^2 G/\partial^2\chi_B = 0$) as illustrated in Fig. 2.4. [75]

If a closed system is located within a negative curvature at a point $\mathrm{P}_1(\chi)$ in that G-χ_B plane, all compositional perturbations to $\mathrm{P}_1(\chi + d\chi)$ along the same chemical potential (on G_1 with μ_1=const.), or constant partial molar free energy, are accessible under the decrease of the Gibbs free energy and only limited by diffusion.

$$\mu_j = \left(\frac{\partial G}{\partial n_j}\right)_{p,T,n_{j\neq i}} \tag{2.3}$$

When this process starts outside the negative curvature, geometrically speaking, outside the two points of inflection, there are states with the same chemical potential (on G_2, with μ_2=const.) that are only accessible via a transient increase of free energy, thus are not necessarily spontaneously accessible. This can only be achieved by a sudden jump in composition due to a nucleation or due to coalescence. For a given temperature and pressure, the locus of the free energy minima and points of inflection onto the temperature or pressure domain constructs the boundaries between stable and metastable (binodal, black) and between metastable and unstable (spinodal, blue). The binodal and spinodal tangent at the upper critical solution temperature T_C [76, p. 183] is thus were the miscibility gap starts to occur. As already mentioned, the phase decomposition is independent of any nucleation, meaning it is solely limited by diffusion. It can then be approached by the second law of diffusion for multiple dimensions by Eqn (2.4), with a change in concentration c over time t and all dimensions ∇ proportional to the diffusion coefficient D. [76, pp. 261, 770]

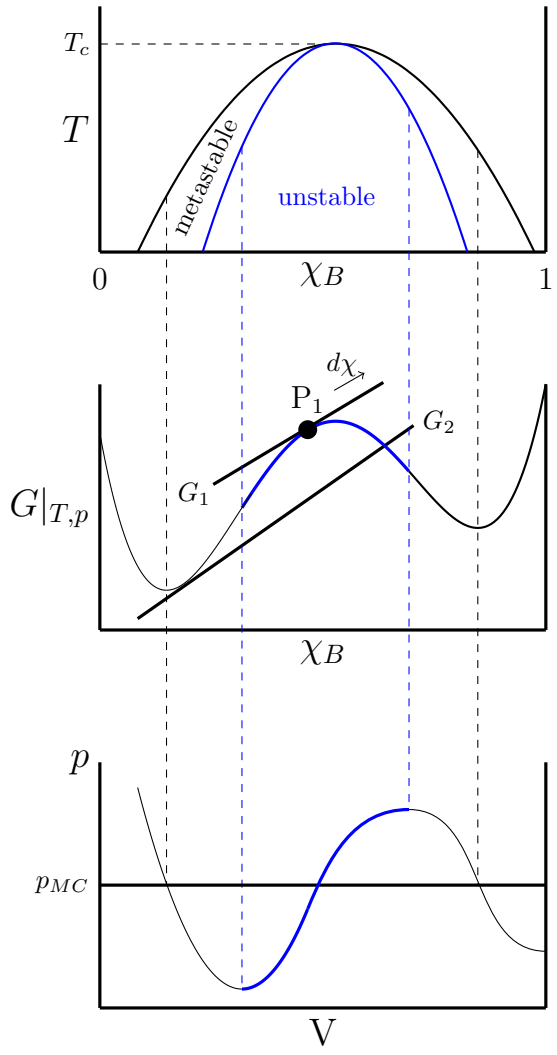

Figure 2.4: Illustrates how the miscibility gap in the temperature domain (top) can be derived from the Gibbs free energy plot (middle) where the metastable (black) and unstable (blue) region is located. The phase diagram in the p-V plane (bottom) shows the same unstable (blue) and Maxwell constructed metastable (black) region.

$$\frac{\partial c}{\partial t} = D\nabla^2 c \tag{2.4}$$

It was shown that the sign of the change in Gibbs free energy in an $\mathcal{O}(n^3)$ approximation, see Eqn. (2.5),

only depends on its second derivative [71, p. 305], which explains why the second derivative of the Gibbs free energy with respect to the molar composition has to be negative and ends at zero, which determines the limit of the unstable region.

$$\Delta G = \frac{1}{2}(\delta c)^2 \frac{\partial^2 G}{dc^2}\bigg|_{c_0} + \mathcal{O}(n^3) \tag{2.5}$$

As mentioned before, the Gibbs free energy can also be represented as a p-V-T surface. Here, the spinodal occurs at locus at the pressure maximum and minimum in the p-V plane. In-between these extrema, the curve shows a positive slope $\frac{dp}{dV}\big|_T > 0$ marking improper physical behavior. These two locus lines thus act as the boundary between metastable and unstable states of that system, rendering all states within them as unstable. The solution to locate the spinodal of water on its p-V-T surface, for example, was only estimated by Poole et al. in 1993, however, is still subject to investigations and debate [77, 78] as it is thought to elucidate the anomalies of water. Outside of that area, the metastable region extends to the intercepts of the isobar Maxwell construction [76, p. 35], bisecting the isotherm $\int_{V_1}^{V_2} pdV = \int_{V_2}^{V_3} pdV$.

2.3.2 Entering the water spinodal using IR-MALDI

IR-MALDI achieves thermal and stress confinement due to the absorption properties of water as shown in Fig. 2.5.

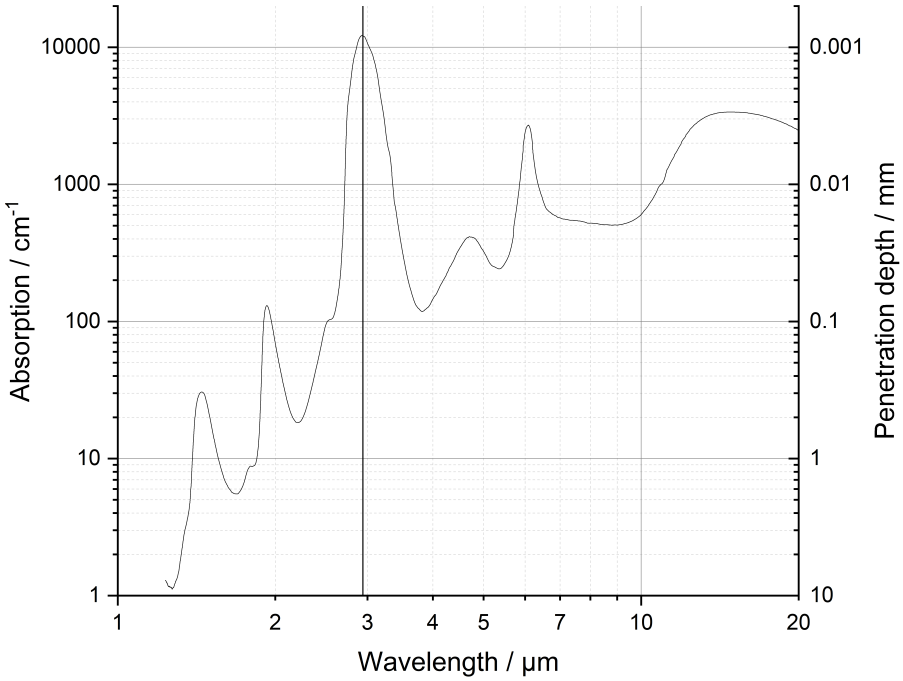

Figure 2.5: Absorption and penetration depth of water in the IR range with the 2940 nm wavelength marked, created from [79].

Here, the absorption peak at 2940 nm is used to create a supercritical state below the surface, which was confirmed by theoretical calculations. [80, 81] The thermodynamics and kinetics of that process proceed

along three steps. At first, the liquid in the focal volume, which is arbitrarily located in the liquid region of the phase diagram but below the critical temperature T_C, is heated and therefore elevated in pressure and temperature. This leads to the generation of a compressive stress wave that turns into a tensile wave at the free surface. When this tensile wave passes that point again, a drastic increase in tensile pressure (negative pressure) under isothermal conditions, due to the thermal confinement, causes the drop below the liquid spinodal from where the spinodal decomposition occurs. Because this can occur under various degrees of freedom, it may be accompanied by less extreme processes such as cavitation or boiling. [82] All these processes eventually generate conditions that can expel the liquid from its bulk.

2.3.3 Dispersion processes in IR-MALDI

With spinodal decomposition, the rupture of the liquid phase is a phenomenon that has already been investigated in numerous studies, ranging from tissue studies [83, 84], via shadowgraphic imaging [23, 85, 86], to theoretic chemical calculations [69, 87]. From an experimental point of view, this can be grouped into two regimes. In the first regime, the expansion takes place isotropically from the origin of the spinodal decomposition. This occurs when the spinodal decomposition is close to the entire volume of the provided liquid phase, which is the case for measurements in single droplets and micron-sized free-standing microbeams. [88, 89] The second regime is reached when the spinodal decomposition happens in bulk or on large surfaces. This enables mechanical recoiling, a more directed ejection of matter, which manifests itself by plume formation that can be stroboscopically imaged. The actual ionization process and origin of charges during the IR-MALDI process is still debatable but is recently thought to be a statistical phenomenon caused by the redistribution of charges. Because the spinodal decomposition and consecutive expansion disperses charges abruptly among nanometer-sized sub-volumes, the sub-volumes have a chance of having non-zero net charges. Given the experimental observation of IR-MALDI only producing low charge states, this process of redistribution is thought to be of Poissonian nature. It is based on the constant autoprotolysis of water, where the ions are abruptly redistributed as a consequence of the spinodal decomposition. Given most of the generated droplets do have net charges of zero, charging is supposed to be a seldom event, thus meeting the essential criterion for a Poisson statistic. [24, 69]

2.4 Bipolar charger and neutralizer

The third technique for charging analytes is direct gas-phase charging, which is applied for already dispersed particulate matter or aerosols. This charging regime is beyond that of the size regime of molecular and macromolecular ionization encountered in xES and IR-MALDI. The charging is based on the creation of a bipolar gas using an x-ray, soft x-ray, or radioactive material source that emits gas-ionizing radiation and generates an equilibrium of positive and negative charges in the gas phase. As the aerosol particles pass that bipolar region, a defined charge distribution is imposed on them. Here, the diffusion properties of ionized gas as well as the sizes of particles are the steering parameters for the outcome of the charge distribution. For a steady state with $\partial n/\partial t = 0$, thus a constant ion flux, the diffusion of the ions towards a spherically symmetric aerosol is given by Eqn. (2.6) with the ions' number density n, the diffusion coefficient of the gas D_g, the radial distance from the center of aerosol r_a, the mobility B, and the electrostatic force F_{es} acting

on it. [90] [76, pp. 261, 841]

$$4\pi r_a^2 \left[D_g \frac{\partial n}{\partial r_a} - BF_{es} n \right] \propto I = \text{const.} \tag{2.6}$$

The amount of net charge of each aerosol particle is cross section-dependent. Empirical studies done by Fuchs [90] and Gunn [91, 92] in the 1950s and unified by Wiedensohler in 1988 [93] delivered a comprehensive charge distribution model, see Eqn. (2.7), where N is the charge state, a_i is the empirically determined polynnomal for the nth order of charge stand N, D_P depicts the particle size in nanometers, and (Z_+/Z_-) is the empirically determined ratio between the two polarities.

$$f(N) = \begin{cases} N \leq 2 & 10 \exp\left[\sum_0^5 a_i(N) \log\left(\frac{D_p}{nm} \right)^i \right] \\ N > 2 & \frac{ea}{\sqrt{4\pi^2 a}} \exp \frac{\left[N - \frac{2\pi a}{e^2} \ln\left(\frac{Z_+}{Z_-} \right) \right]^2}{\frac{4\pi a}{e^2}}, \qquad a = \epsilon_0 D_P \kappa_B T \end{cases} \tag{2.7}$$

Here, the Fuchs charge distribution is used for charge numbers of two and below and the Gunn distribution for charge numbers above two. Empirical data for $a_i(N)$ is well documented for each type of ionization source, usually up to a charge number of six, in some cases even above that. Executing these equations both at a temperature of $T = 300$ K delivers the distributions shown in Fig. 2.6. For the size range of $1 < D_P < 1000nm$ for both polarities, see Fig. 2.6 left. For the first six positive charge states, see Fig. 2.6 right.

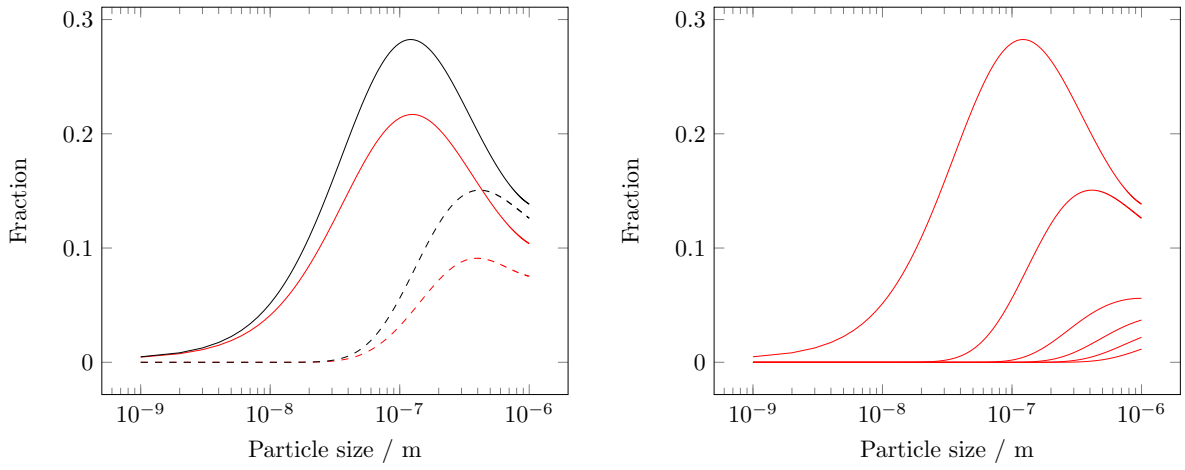

Figure 2.6: Left: Charge distribution of the singly (solid) and doubly (dashed) charge states in the positive (red) and negative (black) polarity over a range of particle sizes, reproduced from [27]. Right: Distribution of the first six positive charge states over a a range of particle sizes.

These steady state charge distributions center the charge population around low charge states, typically one or two in each polarity. This can be interpreted as a charge neutralization coming from the ES point of view, or a charge increase coming from an ambient gas point of view. The main advantage of using this

technique is absolute quantification of aerosols in the size range of ten to one thousand nanometers. This may be a number, surface, or volume, and therefore a mass concentration of particles.

2.5 Electric mobility

In general, electric mobility describes the movement of charged particles or molecules along an electric field gradient hindered by an ensemble of frictional forces. Electric mobility comes in different flavors depending on the particles and on the scientific community, both of which will be discussed in the upcoming two sections. For single molecules and macromolecular structures, this is given as ion mobility. For large molecular structures and particles, it is given as differential mobility. Although both represent electric mobility properties, the measurement principles and therefore physical interpretation of these sizes are very different. As a rule of thumb, the ratio between the expected characteristic length of the ion and the mean free path of the surrounding gas can be used to decide when to use what mobility regime. This, however, is also a matter of pressure, given that the mean free path is pressure dependent.

2.5.1 Ion mobility

Definitions and justifications Typical for ion mobility is a characteristic length of the ion that is much smaller than the mean free path of the gas. This causes collisions between the ion and the gas to occur as discrete events. In that molecular realm, a small characteristic length correlates with a smaller mass. [94] Thus, momentum of inertia transfer and dipole and quadrupole interactions between the ions and the gas have a significant impact on the measured size as well as on the diffusive forces. After its inception, an ion cloud will start diffusive broadening along the concentration gradient from the cloud to the surroundings. This process is dictated by the first law of diffusion [95, p. 215], as shown in Eqn. (2.8) for one direction, where the ion flux can be expressed in terms of a diffusion coefficient of the ion D_{ion} along a concentration gradient ∇, or as a diffusive velocity v_{ion} of an ion number density n_{ion}.

$$J_{ion} = -D_{ion}\nabla_{n,ion} = v_{ion}n_{ion} \tag{2.8}$$

Although the diffusion coefficient and diffusive velocity comprise the electrostatic interaction information, they do not explicitly provide a value for them, but rather make use of empirical values. When this diffusion is now set in an electric field, this can be expanded to the generally balanced Eqn. (2.9). [96]

$$m_{ion}\frac{d^2}{dt^2}\vec{r} + \mu_{ion,red}\nu\frac{d}{dt}\vec{r} = q_{ion}\vec{E} \tag{2.9}$$

Here, the mass of the ion m_{ion}, its reduced mass $\mu_{ion,red}$, the collision frequency ν between the ion and the neutral molecules, the electric charge q_{ion} of the ion, and the strength of the electric field $\vec{E}$ are incorporated. It is this number density in Eqn. (2.9), expressed as collision frequency ν, that results in the pressure and temperature dependence of the mobility of an ion. For $q \neq 0$ and a high number density of the gas, thus at ambient pressures, the collision term dominates, leading to the so-called drift tube velocity equation with $\vec{v}_{dt}$ being the drift tube velocity and K the mobility of the ion. [95, p. 165]

$$\vec{v}_{dt} = K\vec{E} \tag{2.10}$$

The ion mobility K, on the other hand, is dependent on the diffusion coefficient D_{ion} of the ion that is ion gas pair-specific as well as temperature-dependent.

$$K = \frac{eD_{ion}}{\kappa_B T} \tag{2.11}$$

It is at this stage, where the electrostatic interactions between the ions and the gas are taken into account, although remaining unspecified. Since these intertwined effects are difficult to disentangle and to put in absolute terms, a mobility value is always given alongside the buffer gas with which it was determined. This collection of electrostatic forces include, but are not limited to, dipole-induced or quadrupole-induced effects the ions have on the gas. Different approaches, including the hard-sphere and the 12, 4 hard-core models eventually led to the central equation of ion mobility, which defines the mobility K. [95, p. 222] [97]

$$K = \frac{3q}{16n_{gas}} \frac{1}{\Omega(T_{eff})} \sqrt{\frac{2\pi}{\mu_{red}\kappa_B T_{eff}}} \tag{2.12}$$

Here, μ_{red} is the reduced mass of the ion-gas system $m_g m_{ion}/(m_g + m_{ion})$, κ_B is the Boltzmann constant, T_{eff} is the sum of the thermal energy of gas and the kinetic energy of the ion along the drift direction, q the electric charge, n_{gas} the number density of the gas, and Ω the collision integral. The collision integral is usually in the sub-nanometers and thus given in $\mathring{A}^2$. [95, 97–99] A more empirical form of that equation includes the experimental correction factor α.

$$K = \frac{3q}{n_{gas}} \frac{1-\alpha}{\Omega(T_{eff})} \sqrt{\frac{2\pi}{\mu_{red}\kappa_B T_{eff}}} \tag{2.13}$$

However, for m_{ion} being significantly larger than m_g, α is usually small and thus sometimes omitted assuming $1 - \alpha \approx 1$. This approach forms the basis for the determination of the collision integral and thus the size of the ion in the realm of ion mobility.

Computational collision cross sections With advances in the theoretical understanding of ion mobility as well as in molecular modeling, it was possible to build models to estimate the collision integral in silico. Their evolution was driven by the increasingly accurate and precise results of experimental collision integral determinations. In their infancy, ion mobility spectrometers only had a resolving power, defined as the peak position over its full width at half maximum, of about 10. [100] Nowadays, they reach 250 or more than 400 with peak deconvolution techniques for drift tube ion mobility spectrometers. [101, 102] This created a need for more and more sophisticated models, so that the calculated results match the experimental ones, however, remaining computationally inexpensive. These approximations are usually based on a projection, a hard sphere, or electron density calculations, all of which will be presented in this section and are exemplified in Fig. 2.7. [103, 104]

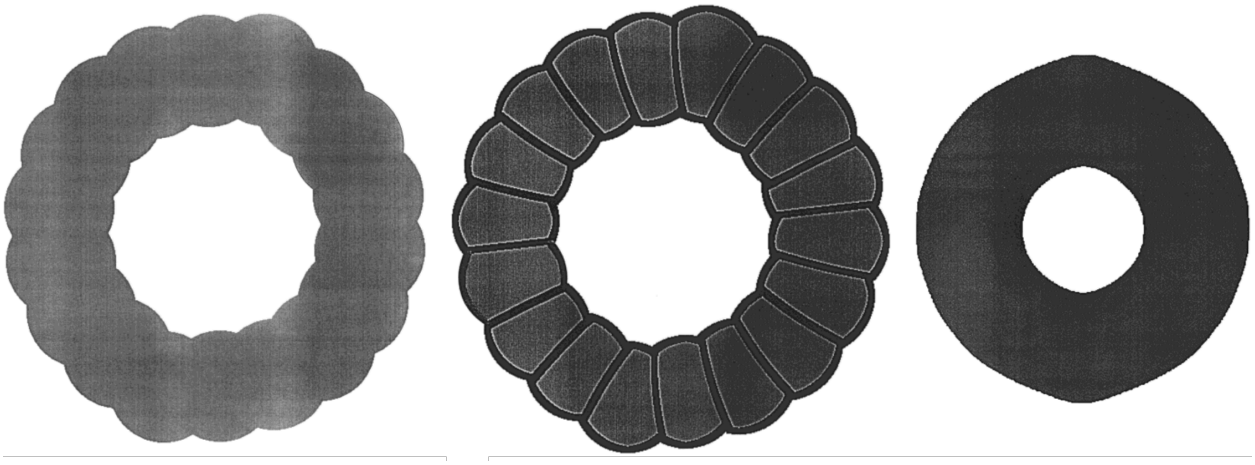

Figure 2.7: The same C_{18} ring cation rendered using projection approximation (left), exact hard-sphere scattering (middle), or scattering on electron density isosurfaces (right), reprinted from [104].

Within the following section, the term *ion* refers to the charged analyte and the term *gas* to the neutral atom or molecule of the surrounding gas.

Projection approximation The projection approximation (PA) was one of the first approaches using a hard-sphere approximation in an (n, 6, 4) potential well. Its inception dates back to 1925 [105], its further developments to the 1960s [106], until its refinement in the 1990s [107] eventually lead to the hard-sphere potential $\varphi(R_a)$ defined by Eqn. (2.14), where r_a and ϵ_φ describe the position and depth of the potential well and n_φ is a fitting parameter that turned to deliver best results when set to $n = 8$, 12, or 16. [107]

$$\varphi(R_a) = \frac{n_\varphi \epsilon_\varphi}{n_\varphi(3-1) - 12(1+\gamma_\varphi)} \left[\frac{12}{n_\varphi}(1+\gamma_\varphi) \left(\frac{r_a}{R_a}\right)^n - 4\gamma_\varphi \left(\frac{r_a}{R_a}\right)^6 - 3(1-\gamma_\varphi) \left(\frac{r_a}{R_a}\right)^4 \right] \tag{2.14}$$

The attractive force between the ion and the ion-induced dipole of the neutral gas is captured by the R_a^{-4}-term, which describes the gas's polarizability. The terms R_a^{-6} and $R_a^{-n_\varphi}$, on the other hand, form a Lennard-Jones-like potential, changing from repulsive to attractive forces over the course of the inter-atomic distance. Finally, γ_φ is a weighing factor for the R_a^{-6} and R_a^{-4} part of the potential.

To determine the collision integral, a square-inscribed circle is generated on an arbitrarily oriented plane and the molecule is cast onto that plane. A number of randomly chosen points within the square are classified as hit or no hit, effectively determining the cross section of that ion in that particular plane. Manyfold averaging over such planes thus gives the collision integral. This approximation is useful for smaller ions of up to 200 atoms, which is in part because they are unlikely to have cavities or indents.

Hard-sphere approximations When the ion gets larger, more expansive structures have to be accounted for to correctly estimate the collision integral. PA does increasingly diverge from experimental results with larger ions because it fails to incorporate real scattering interactions, such as deflection scattering and multi-scattering trajectories. To account for this, the hard-sphere approximation is used on each atom of the ion,

effectively creating a calotte model of the ion. Then, gas is cast onto that calotte model and its trajectory is calculated, either by omitting intra-molecular scattering processes (trajectory approximation [108])

$$\Omega_{avg}^{(1,1)} = \frac{1}{4\pi^2} \int_0^{2\pi} d\Theta_s \int_0^{\pi} d\varphi_s \sin\varphi_s \int_0^{2\pi} d\gamma_s \ \pi b_{min}^2 \tag{2.15}$$

or by taking them into account (exact hard-sphere scattering [109]).

$$\Omega_{avg}^{(1,1)} = \frac{1}{4\pi^2} \int_0^{2\pi} d\Theta_s \int_0^{\pi} d\varphi_s \sin\varphi_s \int_0^{2\pi} d\gamma_s \int_0^{\infty} db \ 2b(1-\cos\chi) \tag{2.16}$$

Both comprise the geometric angles Θ_s, φ_s, and γ_s and the impact parameter b or b_{min} that are the defining features for the hard sphere. Using the calculated trajectories, the collision integral is determined. It is numerically averaged over a large number of casts and over all three spatial directions and yields the first order approximation collision integral $\Omega_{avg}^{(1,1)}$. The latter equation does extend this to multiple intra-ion scattering events and the final scattering angle χ is computed by tracking these four geometric parameters for each and every cast, until the gas atom leaves the ion for good, thus $\chi(\Theta_s, \varphi_s, \gamma_s, b)$. This way, locally convex and concave surfaces of the ion can be accounted for.

Scattering on electron density isosurfaces A third approach to calculate the collision integral is based on electron density calculations. These quantum chemical electron densities are used to build an isosurface that is the basis for the ion-gas interactions. The model is thereby able to account for dynamic electron behavior such as chemical bonding on electron orbitals and electron spill-out, which is especially important for anions. [103] By using this surface, this model effectively takes attractive forces into account. [100] This is solved by using Eqn. (2.17), which is similar to Eqn. (2.15) but the scattering angle χ is replaced by $M(\Theta_s, \varphi_s, \gamma_s, b)$ that is unity for integers and null for non-integers. [100]

$$\Omega_{avg}^{(1,1)} = \frac{1}{4\pi^2} \int_0^{2\pi} d\Theta_s \int_0^{\pi} d\varphi_s \sin\varphi_s \int_0^{2\pi} d\gamma_s \int_0^{\infty} db \ b \ M \tag{2.17}$$

2.5.2 Differential mobility

Differential mobility (DM) is an electrical mobility that applies to much larger objects than ion mobility does. Within this section, the term *particle* refers to the investigated (charge-carrying) species and the term *gas* to the single atom or molecule of the surrounding gas. Since DM is usually applied in air at ambient pressures and temperatures, thus with a typical mean free path around 70 nm, particles between 100 and 1000 nm are in permanent contact with the gas. Therefore, theoretical justifications stem from the realm of fluid dynamics, the gas being the fluid, and the particle being the solid. In the following section, a brief introduction to kinetic gas theory and the motion of particles is given. After that, their behavior when charged and put in an electric field is described, before heading to the particle distributions specific to the DM community.

Kinetic theory of gases The advent of kinetic gas theory made it possible to describe gaseous processes based on the gas's kinetic energy, its impacts on its container, on momentum and mass transfer, microscopic properties that manifest themselves in their macroscopic counterparts of temperature, pressure, viscosity,

and diffusion respectively. [110, p. 17] A first important parameter is the kinetic energy the gas has. It is given by the mean square molecular velocity c_{rms}, where M_g is the molar mass of the gas, R_g the universal gas constant, T the temperature, and $\bar{c}^2 = c_x^2 + c_y^2 + c_z^2 = 3c_x^2$, given its isotropic nature. [110, p. 19]

$$c_{rms} = \sqrt{\bar{c}^2} = \sqrt{\frac{8RT}{\pi M_g}} \tag{2.18}$$

The c_{rms} depicts the velocity distribution, which can be described in terms of the magnitude of the molecular velocities in any direction. [110, p. 21]

$$\bar{c} = 4\pi \int_0^\infty c^2 \left[\frac{m}{2\pi\kappa_B T}\right]^{\frac{3}{2}} \exp\left[\frac{-mc^2}{2\kappa_B T}\right] dc = \sqrt{\frac{8RT}{\pi M_g}} \tag{2.19}$$

A second important parameter is the number density of the gas, as it directly relates the velocity to the mean free path λ via Eqn. (2.20) with n_g is the number density of the gas and d_{coll} the collision diameter.

$$\lambda = \frac{1}{n_g \pi d_{coll}^2 \sqrt{2}} \tag{2.20}$$

The collision diameter is a property that can be determined using ion mobility spectrometry and $\Omega_D(T_{eff}) \propto d_{coll}$. [95] The third important parameter is the viscosity, more precisely the coefficient of dynamic viscosity, of the gas. Viscosity describes the internal frictional forces a gas (or liquid) imposes on itself due to a linear momentum flux along the velocity gradient of different regions within the gas. It is purely mechanically defined via [76, p. 756]

$$J_x = -\eta \frac{dv_x}{dz} \tag{2.21}$$

where J_x is the momentum transfer via a velocity change in the x-direction dv_xover a distance z, orthogonal to direction x. The proportionality factor η, which in this case represents the dynamic viscosity, can also be expressed in terms of the mean free path λ, the number density n and $\bar{c}$ as done in the following equation. [110, p. 24]

$$\eta = \frac{1}{3}\lambda \bar{c} m n = \frac{2\sqrt{m\kappa_B}}{3\pi^{3/2} d_{coll}^2} \cdot T^{\,0.74} \tag{2.22}$$

Here, temperature exponent is an empirical fit parameter found to hold for the range of 223 K to 773 K. In order to analytically solve the various momentum transfers, it is important to take the dimensions of the gas into account. The two forces that come into play are, on the one hand, the time-independent frictional force between the gas and its container or any other object within the gas and, on the other hand, the time-dependent inertial forces of the gas itself. The ratio between the frictional forces and inertial forces that act on a fluid is the Reynolds number.

$$Re = \frac{F_{in}}{F_{fr}} = \frac{\rho v d_{coll}}{\eta} \tag{2.23}$$

Motion of particles With the gas now fully parametrized, particles can be added. To describe the motion of particles in a fluid, it is important to denote the realm of the interactions, which is based on the particle dimension with respect to the mean free path of the gas. This is the free molecular (D_P = 1-20 nm),

transition (D_P=20-1000 nm), or continuum regime (D_P > 1000 nm), all in reference to the mean free path of the gas at atmospheric pressure as shown in Fig 2.8. [111]

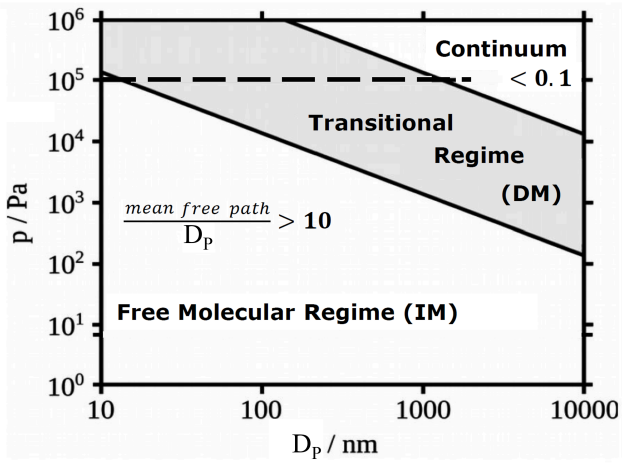

Figure 2.8: Depiction of the drag and collision regime based on the mean free path λ over a range of pressure, recreated from [111].

In the context of electrical mobility, the particles are usually accelerated by the electric field, for which they must have non-zero net charges. The force opposing the particles' motion is the drag force, which is rooted in the momentum transfer from a particle traveling through a gas phase to the gas, at a different velocity as the gas itself. The drag force is the result of the combination of two major principles, summarized in the Navier-Stokes equations for the conservation of mass

$$\nabla \cdot \mathbf{v} = 0 \tag{2.24}$$

and Newton's second law

$$\rho \left(\frac{\partial v}{\partial t} + v \nabla v \right) = -\nabla p + \eta \nabla^2 v \tag{2.25}$$

with ρ as the mass component and the time-derived velocity v as the acceleration term. By assuming a constant flow of gas $\partial v / \partial t = 0$ and keeping the particle at a standstill, this rearranges to Eqn. (2.26), which can be solved analytically by taking spherical symmetry and the boundary condition that the velocity is zero at the surface of the particle into account.

$$\nabla p = \eta \nabla^2 v \tag{2.26}$$

When doing so, this delivers the normal force component

$$F_n = 2\pi \eta v_\infty R_a \tag{2.27}$$

and the tangentially-acting frictional component.

$$F_\tau = 4\pi \eta v_\infty R_a \tag{2.28}$$

Here, v_∞ is the gas velocity at a large distance from the particles and R_a is the distance from the center of mass of the particle, rendering $R_a = r$ the surface of a spherical particle. At this surface, the sum of both components delivers the final term for Stokes's drag force, with D_P the particle diameter.

$$F_D = 3\pi\eta v_\infty D_P \tag{2.29}$$

On the other hand, there is the solely Newtonian approach, where drag is only dependent on the particle size, thus on the mass of gas that is replaced when the particle takes the gas's place.

$$\dot{m}v \propto \rho\frac{\pi}{4}D_P^2 v^2 \tag{2.30}$$

The proportionality factor C_D, the drag coefficient, does however depend on the dimension ratio of the particle and the mean free path of the gas, thus giving a more complex picture of the drag force as a whole, as summarized below. [110, p. 43]

$$C_D(Re) = \begin{cases} Re < 1 & \dfrac{24}{Re} & Stokes's\ Law \\ 1 < Re < 10^3 & \dfrac{24}{Re}\left(1 + 0.15Re^{\,0.687}\right) & Transition \\ Re > 10^3 & \cong 0.44 & Newton's\ Law \end{cases} \tag{2.31}$$

With this in place, the central paradigm in differential mobility is the electrical terminal settling velocity v_{TE}, analogous to the mechanical mobility, and given for the equilibrium F_D=F_E for a particle with charge q. How to approach the electrical terminal settling velocity v_{TE} depends on the Reynolds number of the system.

$$v_{TE}(Re) = \begin{cases} Re < 1 & \dfrac{q\vec{E}C_C}{3\pi\eta D_P} \\ Re > 1 & \sqrt{\dfrac{8q\vec{E}}{\pi\rho_g D_P^2 C_D}} \end{cases} \tag{2.32}$$

Here, C_C is the slip correction factor, correcting for the fact that the velocity difference between the particle and the gas is not zero at the surface of the particle. This slip factor is an empirically derived factor that depends on the mean free path λ and the particle dimension D_P.

Aerodynamic equivalent sphere For particles that are not perfectly spherical, a so-called dynamic shape factor is incorporated to match the experimental velocities with the theoretical results. The maxim for the shape factor is that all perturbations in shape and size must preserve the terminal electrical settling velocity. This means that inertial forces, which are mass dependent, and frictional forces, which are shape dependent, must remain constant. First, an irregularly shaped particle of arbitrary dimensions is approximated by a sphere of equivalent terminal velocity (Stokes equivalent sphere) as the initial particle. Second, this sphere diameter is adjusted to a density of 1000 kg m^{-3}, maintaining its terminal velocity (aerodynamic equivalent sphere). By default, this is the property shown as *diameter* in a DM spectrum. This is then the

electric mobility of an aerodynamic equivalent sphere to the measured particle, meaning it has been shape- and density- (and thus size-) corrected. The physical interpretation of these diameters may thus lead to confusion.

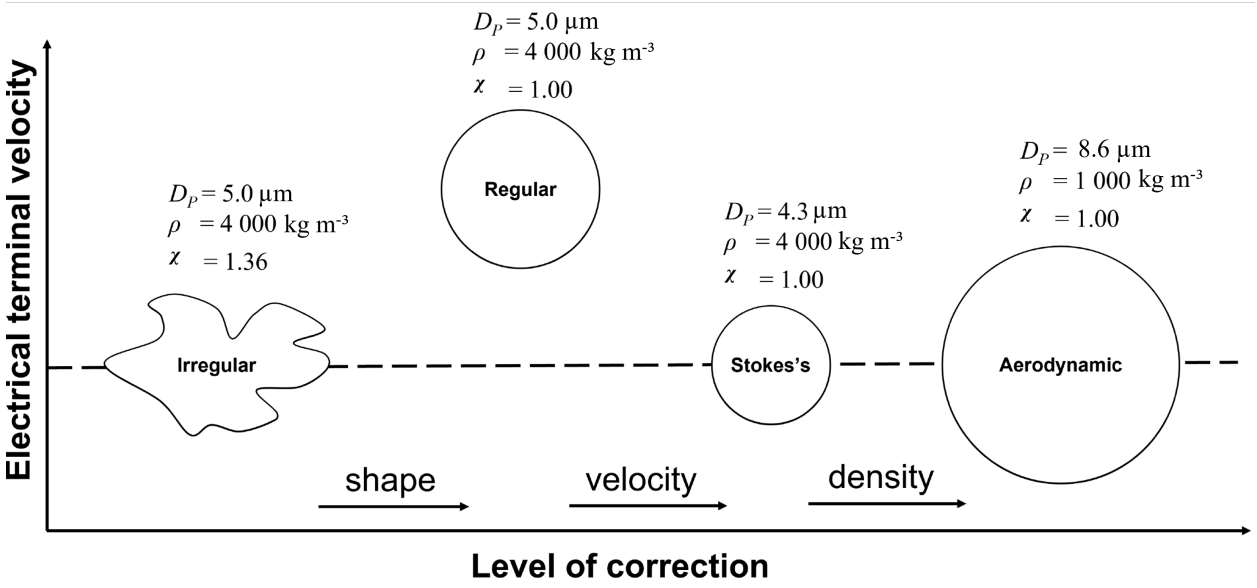

Figure 2.9: Scheme of the particle transformation model used to correct for shape and density, while retaining the electrical terminal velocity, derived from [110].

DM geometries At the heart of differential mobility analyzers is the separation chamber. A polydisperse, charged aerosol stream Q_a enters this region upon laminarization by a sheath gas stream Q_S. The sheath gas stream determines the time of flight and is thus a major parameter in the time-dependent peak separation and broadening process, above all due to Brownian motion. The electric field of a few kilovolts is applied orthogonally to that gas stream and usually spans about 1 cm.

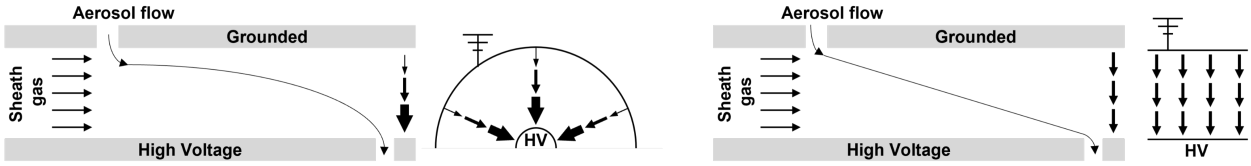

Figure 2.10: The cross section view of DM analyzers in flow direction of the sheath gas and orthogonal to it. Left: Annular design with inwardly increasing electric field strength causing a ballistic particle trajectory. Right: Planar design with a constant electric field strength causing a fairly linear particle trajectory.

Generally speaking, DM analyzers come in two geometries, the annular, with a radial electric field between two coaxial rods, or with parallel-plate geometry, with a linear electric field gradient, see Fig. 2.10. [112–114] The parallel-plate design usually provides a better resolution, which increases with the laminar-limited flow $\sqrt{Re}$ and breakdown-limited electric field $\sqrt{\vec{E}_{DM}}$ because it can handle much larger sheath gas flows and the electric field gradient is constant between the two plates. Recently, a resolution of over 100 [114] was

achieved by realizing Re as high as $9 \cdot 10^5$ while still retaining a laminar flow. The annular design, on the other hand, has a larger dynamic range of up to three orders of magnitude, however at the cost of resolution. Here, major advances were made in the early 1990s, when the Vienna-type design of the DM analyzer was developed. It uses a tangential geometry to merge the aerosol and sheath gas stream, which drastically increased laminarity of the total gas flow. [115] Given its radial electric field, the electric field gradient is increased the closer the aerosol moves from the outer (ground) to the inner (high-voltage) rod and causes a ballistic trajectory of the aerosol.

2.6 Mobility detectors

The two modes of detection for electrical mobility are electric counting of charges via Faraday detectors and direct particle counting, most notably the condensation particle counters.

2.6.1 Faraday detector

The Faraday plates are used in ion mobility spectrometry as well as in differential mobility analysis to quantify the amount of electrical charge over time. The measured currents are usually in the nanoampere range and require intense amplifications of GV/A to achieve a measurable potential of volts or millivolts. Faraday plates are usually used for molecules or nanoparticles, thus below 10 nm. Recent DM analyzers that have a Faraday plate as a detector have a response time of 25 ms. [116]

2.6.2 Condensation particle counters

For the detection of larger and therefore much less frequent species, with nominal currents in the femtoampere range, single-particle detection methods are preferred, such as condensation particle counters. They operate as a nucleation-mode optical counter. [117] Here, the incoming particle enters a particle-cooling conditioning chamber followed by a hot chamber with a solvent-supersatured atmosphere, often water, where the cooled particles act as nucleation seeds so that the solvent continuously condenses onto that particle, making it grow past the optical detection limit. By doing so, the optical detection limit is replaced by the vapour pressure-driven limit for condensation. This is limited by the Kelvin diameter [76, p. 652] with the surface tension σ, the vapor pressure at the curved surface of the droplet of radius r p_r, and the vapor pressure at a plane surface with $r = \infty$, p_∞.

$$r = \frac{2\sigma V_m}{RT \ln \frac{p_r}{p_\infty}} \tag{2.33}$$

For water and butanol, this computes to a 50% detection cut-off of 2.5 nm and 0.8 nm, respectively. A condensation particle counter in a DM setup does have a rise time of about 250 ms [118], making it slower than a Faraday plate. However, unlike Faraday plates, it is capable of detecting a single particle.

Particle distributions The electrical mobility spectra obtained in DM measurements are frequency density functions of the differential mobility. Because there is little consensus about how to present these distributions in the aerosol community, and not all representations are intuitive, this section gives a brief overview on relative peak positions, different normalization methods and single population descriptors.

Modality and mobility It is important to differentiate between the mobility seen in a DM spectrum and its extrapolation to the modality of the measured population. Within a DM spectrum, peaks at the same electric mobility are monomobile. However, many comprise a multimodal population. The same goes the other way around, if there are multiple peaks in a DM spectrum, they can be the different charge states of a single monomodal population. Simple linearized diameter-charge plots help to distinguish or confirm such populations, see Fig. 2.11.

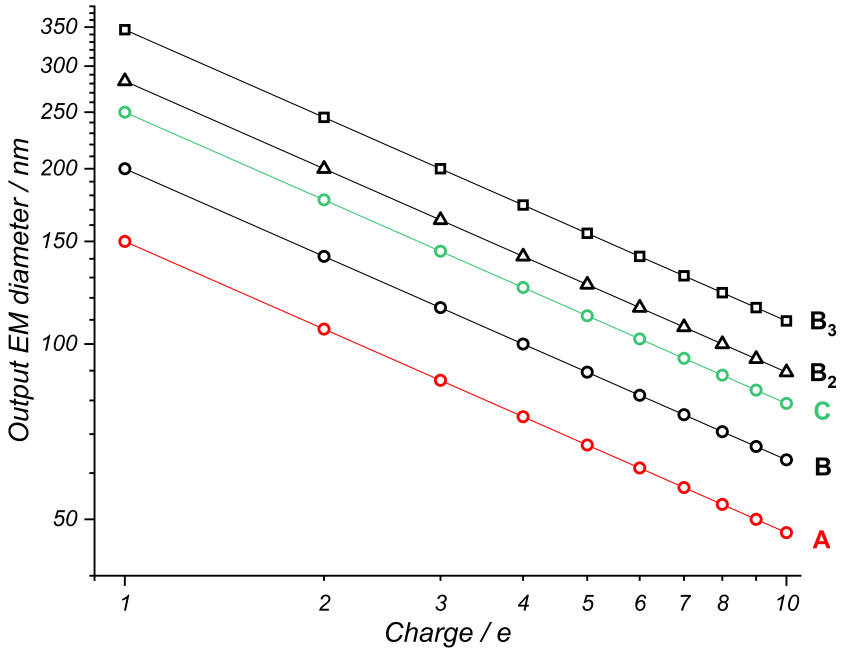

Figure 2.11: Linarized EM diameter-charge plot of the three monomodal particle populations of 150 (A), 200 (B, B_2, and B_3), and 250 nm (C) nominal diameter. Particles with the same modality are located on the same line, each consisting of individual monomobile points.

Scales and normalizations Although the DM probes the differential electrical mobility of a particle population, its results are often represented in units of length, surface, or volume and mass concentration, depending on the scientific community. Because aerosols show a log-normal size distribution upon formation, they are often represented on such a plot. To retain comparability between different devices, the number of counts is often normalized to each size (length) decade.

$$\frac{d}{dlogD_P}W = dW \cdot Res_{Ch} \tag{2.34}$$

Here, channel resolution Res_{Ch} refers to the number of channels in each size (length) decade. The weighting factor W assigns each channel a weight depending on whether the spectrum is on a scale of length, surface or volume, thus mass.

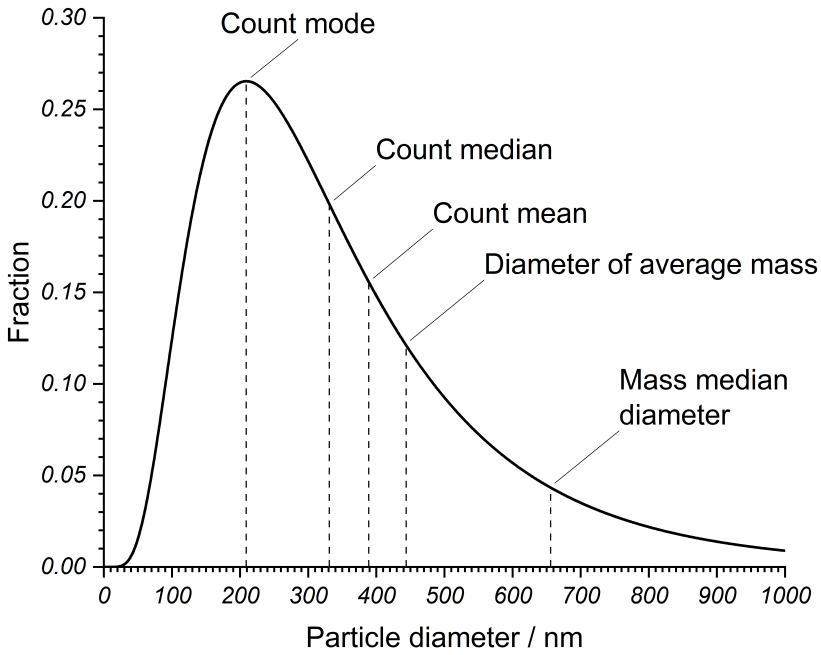

Figure 2.12: An example curve for a particle size distribution with different descriptor of that distribution annotated, reconstructed from [110].

2.7 Laser light and solid interactions

The final application of infrared (IR) laser light in this work shifted the wavelength domain from the short wavelength infrared (SWIR) laser light to the near infrared (NIR). Here, two different IR applications were explored, the low-fluence realm of laser-induced incandescence (LII) and the high-fluence realm of laser-induced breakdown spectroscopy (LIBS), both of which will be introduced in the following section and are illustrated in Fig. 2.13. [47]

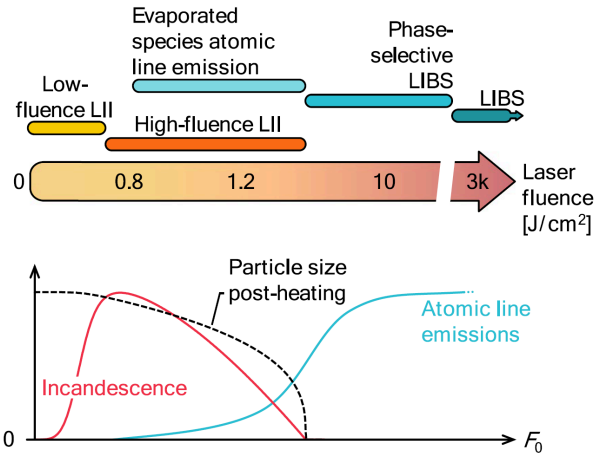

Figure 2.13: Top: An illustration of LII and LIBS categories across a fluence range. Bottom: The intensity evolution of the emitted signals along this fluence range with the shrinkage of the particle annotated with dashed line, reprinted from [47].

As the graph suggests, the information content emitted by LII and LIBS are fundamentally different. LII emission is the direct consequence of the light absorption, heat transfer and heat radiation of the whole particle, thus revealing ensemble properties of multiple elements. For LIBS on the other hand, the emission, notwithstanding ensemble effects during the ablation process, is an atomic and thus specific property of each element involved.

2.7.1 Laser-induced breakdown spectroscopy

LIBS is a plasma-based form of atomic emission spectroscopy that is widely used for the compositional analysis of materials. Since it is based on elemental emission lines, virtually any element in the periodic table can be accessed by LIBS. It requires very little sample, no preparation thereof, and can be applied contactless at a distance. These practical properties have driven LIBS applications, especially in extreme environments such as metallurgy [119], deep sea water [120] and on Mars [121, 122]. The laser-induced breakdown occurs in successive steps, as shown in Fig. 2.14.

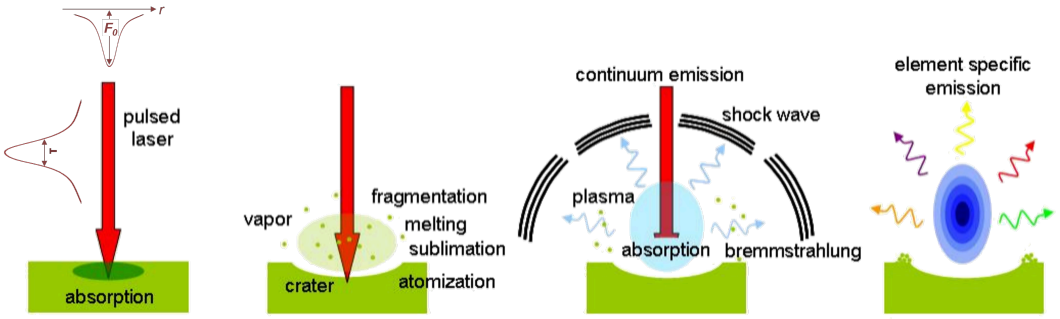

Figure 2.14: An illustration, reconstructed from [123, 124], of four major steps during the LIBS process, from left to right: absorption, ablation, continuum and shock wave emission, and atomic emission.

The first step is the absorption of energy by the material from a pulsed laser with a profile in space $F_0(r)$ and time τ. [124, 125] While the spatial dimension is more or less always in the micrometer size range, the temporal profile differs greatly between different LIBS communities, ranging from routinely used nanoseconds down to highly-specified femtosecond laser pulses. [126] After absorption, the energy dissipates by heating the particle, causing ablation and vapor formation above the surface. This amount of ablated mass is a direct consequence of the laser properties, absorptance A and pulse energy E_{puls}, and the particle properties, specific evaporation enthalpy $\Delta_{vap}H$ and specific heat capacity c_{heat}. [125]

$$\rho V = \frac{AE_{puls}}{(\Delta_{vap}H + c_{heat}\Delta T)} \tag{2.35}$$

Upon condensation of that vapor and further energy uptake, heating escalates, ionizing the vapor, thus creating a plasma. This plasma, usually accompanied by an electron number density of 10^{16} to 10^{18} cm^{-3}, evolves highly dynamically under quick expansion and cooling, while emitting two principle sorts of information, light and pressure waves. The shock wave amplitude, as the acoustic response, is assumed from Eqn. (2.35) to be directly related to the amount of ablated material, which forms the basis for the plasma formation. [127–129] The light emission, on the other hand, is sub-divided into electron-ion-recombinant continuum emission, bremsstrahlung, and element-specific atomic emission. The former is emitted first, while the latter peaks in intensity microseconds after the plasma ignition. [125] Formally, the absolute line intensities can be approached by Eqn. (2.36) under the assumption of local thermodynamic equilibrium, where the intensity of the transition from the upper state i to the lower state j of the atomic state I experimentally depends, upon normalization, only on the number densities n^I and n^{II} of the atomic and ionic state, respectively. A_{ij}, g_i, and $U^I(T)$ account for the transition probability, statistical weight, and temperature-dependent partition function, respectively. [130]

$$I^I_{ij} \propto n_s \frac{n^I}{n^{II} + n^I} \frac{g_i \exp(-E_i/\kappa_B T)}{U^I(T)} A_{ij} \tag{2.36}$$

From Eqn. (2.36), it becomes apparent that the plasma temperature is essential, nevertheless, it remains experimentally inaccessible for an individual plasma. Not knowing that, exact plasma temperature poses an ongoing challenge in LIBS measurements when it comes to absolute quantification. To ease that restriction, a Saha-Boltzman-based calibration is used to estimate this plasma temperature, again for a population of events, thus not a single event. The aforementioned photoacoustic detection applied to LIBS can also be

used, as it relates to the amount of ablated mass, which in turn relates to the plasma temperature. This acoustic response can then be assigned to a single event. Attempts to reduce plasma temperature variations by reducing matrix effects in general have been alternative ways to counter that problem. These techniques range from double- or triple-pulse measurements all the way to phase-selective LIBS (PS-LIBS) setups all aiming to isolate the ionized matter from the rest of the matrix. [131, 132]

2.7.2 Laser-induced incandescence

As LII does not lead to plasma formation, different laser-induced processes play a role here. These processes are based on an energy balance, Eqn. (2.37), and characterized by a constant loss of mass, Eqn. (2.38). [47] As the particles in LII start to exhibit incandescence at some point, their internal energy inevitably must have been raised to a temperature that enables such light emission, thus having been promoted to an electronically excited state. This requires the energy dissipation to be slower than the energy absorption, eventually leading to a heating of the particle and consequently raising the internal energy, as expressed by the term on the left side of Eqn. (2.37). This increase of internal energy is the result of the absorption of laser energy and its consecutive dissipation, with the dissipative processes being heat conduction, heat radiation, and matter evaporation. [133]

$$\frac{dU_P}{dt} \propto \underbrace{F_0 f(t) C_{abs,\lambda}}_{\text{absorption}} - r^2 [\underbrace{\alpha_{th} n_g c_g \langle E_{g,o} - E_{g,i} \rangle_{max}}_{\text{conduction}} - \underbrace{n_{vap} c_{vap} \Delta_{vap} h}_{\text{evaporation}} - \underbrace{\sigma_{SB} \varepsilon_\lambda (T_P^4 - T_0^4)}_{\text{radiation}}] \tag{2.37}$$

The amount of absorbed energy depends on the laser beam's fluence F_0 and temporal profile $f(t)$, as well as on the particle's absorption cross section $C_{abs,\lambda}$, which is wavelength-specific. The heat conduction comprises heat dissipation within the particles and outwards to the surrounding gas molecules upon collision. The number density n_g and velocity c_g make up the number flux of the gas, transferring $\langle E_{g,o} - E_{g,i} \rangle_{max}$ amount of energy per collision with respect to the thermal accommodation coefficient α_{th}, effectively cooling the particle. Another particle-cooling process is evaporation. Again, the number flux is made up of the number density n_{vap} and the velocity c_{vap}, but this time, of all the atoms and molecules leaving the particle, thus being vaporized. In sum, this evaporation manifests itself in a continuous mass loss of the particle that can be described by Eqn. (2.38).

$$\frac{dm_P}{dt} = -\frac{q_{evap}[T_P(t)] m_{vap}}{N_A \Delta H_{vap}} \tag{2.38}$$

This adds yet another layer of dynamic behavior to the laser particle system in the form of a dynamic differential equation that includes a temperature-dependent, thus time-dependent, evaporation heat. In addition to that, when the particle mass is reduced, so is the absorption cross section, and the energy balance attunes anew. This dynamic proceeds until the particle evaporates out of existence or the particle exits the laser beam. The last process in Eqn. (2.37) describes the radiation, which includes the wavelength-dependent emissivity factor ε_λ of the particle and the Stefan-Boltzmann constant σ_{SB}, which formulates the emitted radiation out of the fourth power of the temperature of the particle T_P, corrected for the surrounding temperature T_0. Since all these processes, and ultimately also the internal energy, relate to the particle dimension, LII embodies a great deal of size information. All parts of the Eqn. (2.37) also contain

composition-specific properties, so does the emitted light. This emission $J(t, q, \lambda_{em})$

$$J(t, q, \lambda_{em}) \propto \int_0^\infty R_{th}(r, t, q, T, \lambda_{em}) P(r) dr \tag{2.39}$$

consists of two contributions, first, the highly convoluted process of thermal response R_{th}, which not only depends on particle size, temperature, and heat, but also evolves over time, and, second, the particle size distribution $P(r)$. Because $P(r)$ is firmly embedded into $J(t, q, \lambda_{em})$, LII is able to determine a population's full size distribution including its mean characteristic length r_m and the width σ_r of the distribution.

$$P(r) = \frac{1}{\sqrt{2\pi}\sigma_r r} \exp\left[-\frac{(\ln r - \ln r_m)^2}{2\sigma_r^2}\right] \tag{2.40}$$

Combining all these principles in LII makes it a comprehensive particle quantification technique that delivers a particle number density, a full set of particle size distribution descriptors, as well as composition information, derived from the LII susceptibility.

3

Publications

The following sections include the publications contributing to this thesis in chronological order. For each publication there will be a brief introduction and an explicit statement of my contributions to the respective paper. The original publication will be attached thereafter.

3.1 In situ monitoring of photocatalyzed isomerization reactions on a microchip flow reactor by IR-MALDI ion mobility spectrometry

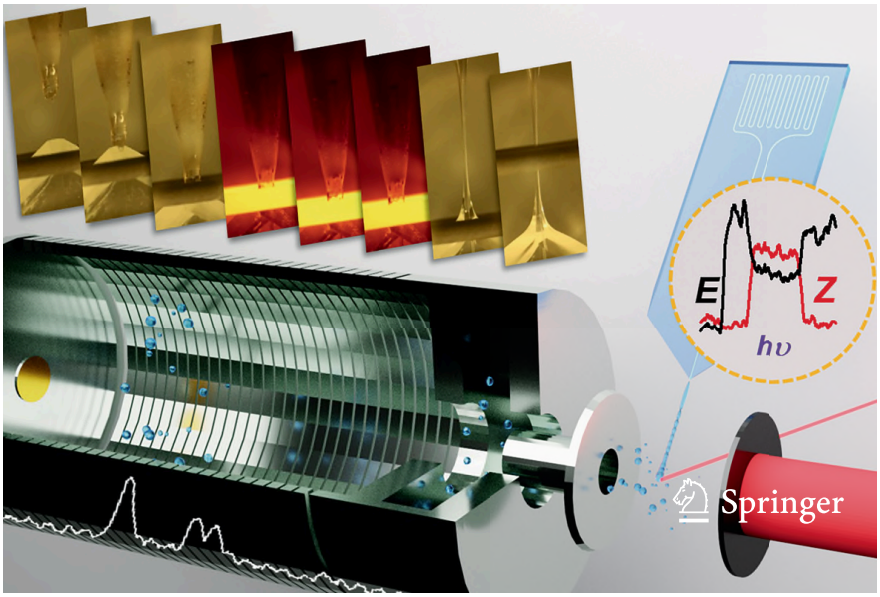

Figure 3.1: Cropped front cover of the 412th volume of the Journal of Analytical and Bioanalytical Chemistry featuring this study.

Scope of the publication The aim of this study was the seamless integration of a microchip flow reactor into a reduced-pressure ion mobility spectrometer using IR-MALDI source as the hyphenation and ionization technique. Using the highly controllable and adjustable microchip environment, it was possible to tightly monitor the fast *E*-*Z* conversion in a matter of a minute or two. Given the small dimensions of the reactor, this approach presents a fast, reliable and quantitative insight into photocatalytic activities. Its practicability as a high-throughput screening method was well-proven and shown to the full extent.

Author's contribution My contribution to this study was the design and realization of the free-standing liquid beam IR-MALDI interface as well as the development of the capillary flow reactor. All measurements shown were conducted by me and evaluated using an independently created code in Matlab to time-efficiently evaluate gigabytes' worth of ion mobility spectra within minutes. Being one of the manuscript editors, my responsibilities included, but were not limited to, its writing, editing as well as all data visualization. Eventually, my work also included the design of the front cover of volume 412 of the Journal of Analytical and Bioanalytical Chemistry, as shown above.

Analytical and Bioanalytical Chemistry (2020) 412:7899–7911
https://doi.org/10.1007/s00216-020-02923-y

RESEARCH PAPER

In situ monitoring of photocatalyzed isomerization reactions on a microchip flow reactor by IR-MALDI ion mobility spectrometry

Chris Prüfert[1] · Raphael David Urban[2] · Tillmann Georg Fischer[3] · José Villatoro[1] · Daniel Riebe[1] · Toralf Beitz[1] · Detlev Belder[2] · Kirsten Zeitler[3] · Hans-Gerd Löhmannsröben[1]

Received: 18 June 2020 / Revised: 17 August 2020 / Accepted: 27 August 2020 / Published online: 12 September 2020

Abstract

The visible-light photocatalytic *E*/*Z* isomerization of olefins can be mediated by a wide spectrum of triplet sensitizers (photocatalysts). However, the search for the most efficient photocatalysts through screenings in photo batch reactors is material and time consuming. Capillary and microchip flow reactors can accelerate this screening process. Combined with a fast analytical technique for isomer differentiation, these reactors can enable high-throughput analyses. Ion mobility (IM) spectrometry is a cost-effective technique that allows simple isomer separation and detection on the millisecond timescale. This work introduces a hyphenation method consisting of a microchip reactor and an infrared matrix-assisted laser desorption ionization (IR-MALDI) ion mobility spectrometer that has the potential for high-throughput analysis. The photocatalyzed *E*/*Z* isomerization of ethyl-3-(pyridine-3-yl)but-2-enoate (***E*-1**) as a model substrate was chosen to demonstrate the capability of this device. Classic organic triplet sensitizers as well as Ru-, Ir-, and Cu-based complexes were tested as catalysts. The ionization efficiency of the *Z*-isomer is much higher at atmospheric pressure which is due to a higher proton affinity. In order to suppress proton transfer reactions by limiting the number of collisions, an IM spectrometer working at reduced pressure (max. 100 mbar) was employed. This design reduced charge transfer reactions and allowed the quantitative determination of the reaction yield in real time. Among 14 catalysts tested, four catalysts could be determined as efficient sensitizers for the *E*/*Z* isomerization of ethyl cinnamate derivative ***E*-1**. Conversion rates of up to 80% were achieved in irradiation time sequences of 10 up to 180 s. With respect to current studies found in the literature, this reduces the acquisition times from several hours to only a few minutes per scan.

Keywords Microchip · Reaction monitoring · IR-MALDI · Ion mobility spectrometry · Photochemistry · Photocatalysis · Olefin isomerization

Introduction

Preparative photoreactions carried out in stirred batch reactors are regularly characterized by reaction times on the scale of hours. This is due to the usually high optical density of the reaction solutions and the resulting low penetration depth of light. In order to achieve low and well-defined liquid layer thicknesses, a number of photoreactor designs, such as flat-bed, falling film, capillary flow, and microchip reactors, were developed. Especially microchip reactors have become popular in recent years.

The narrow width of the tubing in capillary flow reactors enables uniform irradiation of the reaction volume. This also offers a series of advantages over photochemistry in batch photoreactors, such as an accurate control over reaction parameters, or the improved heat transfer due to the larger surface-to-volume ratio. Moreover, there is a controlled

Chris Prüfert, Raphael David Urban and Tillmann Georg Fischer contributed equally to this work.

Electronic supplementary material The online version of this article (https://doi.org/10.1007/s00216-020-02923-y) contains supplementary material, which is available to authorized users.

✉ Chris Prüfert
cpruefert@uni-potsdam.de

✉ Hans-Gerd Löhmannsröben
loeh@chem.uni-potsdam.de

[1] University of Potsdam, Physical Chemistry, Karl-Liebknecht-Str. 24-25, 14476 Potsdam, Germany

[2] Institute of Analytical Chemistry, Leipzig University, Linnéstraße 3, 04103 Leipzig, Germany

[3] Institute of Organic Chemistry, Leipzig University, Johannisallee 29, 04103 Leipzig, Germany

mixing of fluids, an enhanced reactivity due to the increased photon flux in photochemical reactions, and continuous multistep syntheses are possible [1]. Additionally, the product is constantly spatially separated from the irradiated reaction zone, which reduces the degree of photodegradation of products and increases the productivity of photochemical processes [2, 3]. An overview of the photoreactions in capillary flow reactors can be found in [1, 2, 4, 5].

While chip-based reactors benefit from similar advantages as capillary flow reactors, they are much more compact and therefore allow enhanced integration of various functionalities on a single device. In addition, chip-based devices can mix solutions dead-volume-free and different reaction zones on the chip containing different solvents can be introduced. The latter enables decoupling of different flow rates in different channels for reaction progression and subsequent analysis [6]. Furthermore, the combination of chemical reactions and online analysis enables time resolved studies of chemical processes. The latter can be realized by applying spectroscopic techniques, such as fluorescence or Raman microscopy, or by coupling microfluidic chips to mass spectrometry. For isomer discrimination, we previously reported the integration of microflow reactions and chip HPLC [7–9] that allowed for the analysis of enantioselective transformations.

Visible light is an inexhaustible source of energy to drive "green" chemical processes. Photocatalysts can be useful as photosensitizers that can absorb visible light and drive reactions of organic molecules via electron or energy transfer, which could otherwise only be carried out using UV light. The absorption of visible light allows new modes of molecule activation and enables challenging or previously unattainable transformations. Iridium or ruthenium polypyridyl complexes are among the most applied photocatalysts. By now, a broad range of novel synthetic methods became accessible through visible-light photocatalysis [10, 11]. In recent years, the direct application of solar radiation for performing photocatalyzed syntheses has also been explored [12–14].

Gilmour et al. investigated that the photocatalytic, bio-inspired *E*/*Z* isomerization of olefins yields almost pure *Z*-isomer (up to 99:1 *Z*/*E*) by using different photocatalysts, in batch processes over 24 h [15]. This isomerization is initiated by a triplet energy transfer from the photocatalyst to an α,β-unsaturated ester and was studied for a series of α,β-unsaturated esters and various photocatalysts, which possess triplet energies in the range of 140 to 250 kJ/mol [15].

A variety of spectroscopic methods have been implemented in order to monitor reactions performed on microfluidic chips. A waveguide interferometer–based UV-Vis spectrometer was used for the detection of an antibody-antigen reaction [16, 17]. However, UV-Vis absorption spectroscopy has a rather poor sensitivity due to the short optical path lengths found in microfluidic chips. An alternative method is fluorescence spectroscopy, which was utilized for the analysis of reaction progress [18] after chromatographic or electrophoretic separation [19–21]. A third method is surface-enhanced Raman spectroscopy, the suitability of which was demonstrated through several studies: by monitoring the progress of a Hantzsch synthesis in droplets [22], in a kinetic study of a platinum-catalyzed reduction of 4-nitrothiophenol to 4-aminothiophenol [23], monitoring the Fenton degradation of rhodamine 6G [24] and the products of a multistep cascade reaction of glycerol to mesoxalic acid [25].

In addition to optical methods, mass spectrometry (MS) allows tracing chemical reactions on the microchip in real time. An example is the monitoring of stereoselective transformations on a microchip by chip-integrated HPLC separation and subsequent electrospray ionization mass spectrometry detection (ESI-MS) [7]. Alternative to ESI, infrared microbeam matrix-assisted laser desorption and ionization (IR-MALDI in high vacuum) MS can be employed. This methodology was used to investigate the kinetics of the synthesis of pyrrolo[2,1-b]benzoxazoles [3]. IR-MALDI is a very soft ionization method that allows detection of short-lived and sensitive intermediates. In the MS configuration applied in [3], the microbeam was situated in the high vacuum region of the MS, enabling the direct transfer of the intermediates into that region after IR-MALDI and thus their immediate detection. IR-MALDI-MS, at atmospheric pressure (AP), has been used to investigate a vinylogous Mannich reaction performed in continuous flow on a microchip [6]. Special features of the microchip were the on-chip dilution step with an IR-MALDI compatible solvent and the chip-integrated nozzle to generate the microbeam.

Ion mobility (IM) spectrometry is a fascinating alternative to MS. In contrast to the time-, cost-, and labor-intensive high-performance liquid chromatography-MS, IM spectrometry is an alternative method with the potential to separate and detect isomeric compounds. This has already been demonstrated for the separation of isomers produced by photoreactions in the gas phase [26, 27] and the photoisomerization of azobenzenes [28]. Analogous to MS, the composition of the reaction mixture in flow reactors can be determined in real time but at reduced costs. The combination of these properties makes IM spectrometry attractive for reaction monitoring. IM spectrometry in combination with ESI was previously used for reaction monitoring of a three-step synthesis [29]. The coupling of a microchip-based HPLC separation and IM spectrometry was also shown [30], demonstrating the potential of chip-HPLC/IM spectrometry as a miniaturized two-dimensional separation method for separating three isomeric antidepressants.

In this work, the photocatalyzed *E*/*Z* isomerization of the ethyl-3-(pyridine-3-yl)but-2-enoate (***E*-1)** in photo flow reactors was investigated by IR-MALDI-IM spectrometry. This technique allows the real-time separation and detection of the *E*- and *Z*-isomer. Two different photo flow reactors, a capillary and a microchip reactor, were studied. Capillary

reactors have the advantage of easier handling due to their modular design but were usually only partially illuminated by the intense irradiation of a single LED. Microchip reactors allow for integrated reaction zones and hence to effectively realize complex mixing processes. Since charge transfer processes at atmospheric pressure can influence the detection of the reaction products, a low-pressure IM spectrometer was used. Herein, we demonstrated the capability of this hyphenated method of microchip and IM spectrometer for high-throughput analysis of a photochemical reaction. Moreover, the effects on the reaction yields of the *E*/*Z* isomerization of a number of photocatalysts were investigated.

Experimental part

General instrumentation and method The experimental setup consisted of the IR laser, the liquid flow supply, the flow reactor, the radiation source, and the IM spectrometer and is schematically shown in Fig. 1. Two different flow reactors were used: a microchip reactor and a capillary flow reactor as reference.

In brief, the *E*-isomer ***E*-1** (2.5 mM) and the respective catalyst (2 mol%) were dissolved in MeCN:MeOH 1:1 (v/v) and irradiated with a single LED ($\lambda = 404 \pm 15$ nm or 365 ± 15 nm) for 10 s in the capillary or 180 s on the microchip. The reaction mixture was diluted (1:99) on-chip and then analyzed by an IR-MALDI-IM spectrometer built in-house. Measurements were performed as follows: a sample of the starting material solution was injected at $t = 0$ s. After the fluid passed through the microchip or the capillary reactor and a stable signal for the starting material was observed, the LED was turned on. Depending on the photocatalyst, the *Z*-isomer was formed as a product and was detected by the IM spectrometer. After a full residence time cycle, the LED was switched off and the measurement was stopped. Then, only starting material signal was observed.

Liquid flow supply Two HPLC pumps (Infinity 1260, Agilent and Azura P 6.1 L, Knauer, GER), an injection valve, and a UV-transparent fused-silica capillary (0.91 m, ID 75 μm, FS UV untreated, CS-Chromatographie, GER) made up the microfluidic system for the first setup. In a second setup, the UV-transparent capillary was replaced by a microchip, providing a tightly meandering reaction channel that further enhances the irradiation efficiency. At the end of the photo flow reactors, a make-up flow was added that dilutes the reaction mixture (1:99) and establishes conditions compatible with IR-MALDI. The make-up flow rates were varied between 79 and 396 μL/min depending on the used reaction channel flow rate. The dilution factor was kept constant.

The solvent, provided by the two HPLC pumps, was delivered through polyether ether ketone (PEEK) capillaries (OD 1/16″, ID 50 μm, JR-T-5802-M5, VICI AG International, CH) into the injection valve. In the capillary reactor setup, a 6-port valve (Azura V 2.1, Knauer, GER) with a 20-μL sample loop was used, and in the microchip reactor setup, a 10-port valve (C72MPKH-4670ED, VICI AG International, CH) with a 50-μL sample loop was used. The reaction mixture was introduced into the sample loop via microinjection ports (M-432-03, IDEX Health & Science, USA) and through in-line filters (JR-0611-SS05-3, VICI AG International, CH) protecting the reaction channels from clogging. For fluid introduction into the microchip, the tubing was connected to polyacrylamide-coated fused-silica capillaries (FS, OD 360 μm, ID 50 μm, Chromatographie Service GmbH, GER) by reducing adapter assemblies (V-447, Upchurch Scientific, IDEX Health & Science, USA). To ensure a pressure-tight interface between the microchip and the fused-silica capillaries, in-house-built stainless-steel connection clamps consisting of perfluoro-elastomeric (FFKM) ferrules and headless 6–32 PEEK screws (N-123-04 and N-123H, IDEX Health & Science, USA), were used [31].

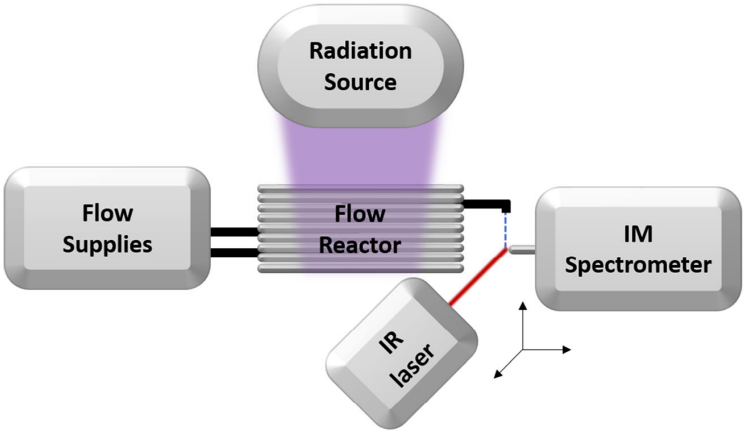

Fig. 1 Scheme of the general setup consisting of the liquid flow supply unit, the flow reactor unit, a radiation source, the ion mobility (IM) spectrometer unit, and an OPO IR laser

Microchip flow reactor The microfluidic glass chips were designed and fabricated in-house by common photolithography, wet-etching, and bonding methods [32]. A description is found in the Electronic Supplementary Material (ESM). Briefly, the microchip consisted of two layers, both of which were manufactured from microscope slides of a soda-lime glass with a size of 76 mm × 26 mm (Carl Roth GmbH + Co. KG, GER). The bottom glass-layer contained etched channels with a depth of 20 μm and a width of 100 μm. To close the channels, the slide was bonded to a top layer with powder-blasted holes that served as inlets for pressure-tight fluid delivery. The glass microchip contained the following functional units: The channel (50 nL) led to a reactor region with an internal volume of 560 nL. After the reactor region, the channel (70 nL) crossed a make-up flow channel where additional fluid (MeCN:H_2O 1:1 (v/v), 1:79 up to 1:299 dilution of the reaction mixture) was delivered to form a liquid jet at the end of the microchip. A pulled glass emitter tip was manufactured at the microchip exit to reduce the flow rate necessary to generate a free-standing liquid jet [33, 34]. The channel had a total internal volume of approximately 680 nL. This channel then tapered into a 20-μm opening which generated the free-standing liquid jet of about 20 μm diameter.

Capillary flow reactor The in-house synthesized *E*-isomer ***E*-1** was dissolved in MeCN (5.0 mM) and mixed with a 100 μM (2 mol%) solution of the respective catalyst in MeCN right before analysis in a 1:1 volumetric ratio. The sample was injected into a 20-μL sample loop of the 6-port valve. From here, the reaction mixture was picked up by a stream of MeCN of usually (0.3–3.0) μL/min and was transferred into a reaction capillary loop ($l = 0.90$ m, $V = 1.8$ μL) with three windings. When the thrice-turned UV-capillary was supplied with 1 μL/min flow rate of analyte solution, a linear velocity of 3.8 mm/s and thus a Reynolds number of about 2 were achieved, indicating laminar flow conditions. Each tube winding has a length of approximately 30 cm. Since the LED had an irradiating surface area of about 1 cm^2, only a part of the total capillary volume was intensely irradiated. This means that the reaction mixture was irradiated three times for a total time of about 10 s, depending on the exact sample flow rate. After that, the reaction mixture was diluted into a make-up flow of MeCN:H_2O 1:1 (v/v) giving a total flow rate of 300 μL/min. This terminated the reaction progress at a defined point in time and generated sufficient throughput to create a free-standing liquid beam of 20 μm in diameter by means of a glass nozzle (OD 1.0 mm, ID 0.235 mm, tapered to ID = 20 ± 2 μm at the nozzle tip, Biomedical Instruments, GER).

Radiation sources For conducting the photoreactions on microchip, a light-emitting diode (LED, 404 nm, operated at 9 A, 3.55 V; CUN0MF9A, Seoul Viosys, KR) was installed in front of the reactor region at a distance of 3 mm and was cooled at the backside by an axial fan (HXB25B12, SEPA EUROPE, GER). Alternatively, a 365-nm LED was used, which had about 2% of the intensity of the 404-nm LED.

IR-MALDI-IM spectrometer The detection of the isomers is based on an in-house-built IM spectrometer as described in a previous publication [35]. A liquid filament, called microbeam, at an atmospheric pressure was used for coupling the photo microchip or the photo capillary reactor to the reduced pressure IM spectrometer [36]. The microchip is mounted between a counter electrode and the inlet electrode of the IM spectrometer (Fig. 2a). To support the liquid beam and to guide charged analytes into the orifice by an electric field (next to the pressure gradient), a counter electrode at a voltage of 7 kV was positioned at the opposite side of the inlet electrode and the liquid beam. This geometry ensured the most uniform electric field around the ionization region. Under nominal operating conditions, the counter electrode was set at a distance of 4 mm from the inlet electrode with the microchip outlet placed midway between them. The laser focal point and the microchip outlet were positioned at a distance of 2 mm in front and 2 mm above of the IM spectrometer orifice with the help of an *X-Y-Z* linear translation stage (Metric XYZ Three-Axis Miniature Translation Stage, Thorlabs GmbH, GER). Throughout all experiments, the capillary and the optical systems were fixed in the laboratory frame to keep the laser beam path's focal point unaltered.

A nanosecond IR laser pulse ($\lambda = 2940$ nm, rep. rate = 20 Hz, $t = 6$ ns, $E = 2.1 \pm 0.1$ mJ, IR Opolette 2940, OPOTEK, USA) was guided through a 99 ± 0.5-cm-long optical pathway achieved with two gold mirrors (PF10-03-M01, Thorlabs GmbH, GER) and a CaF_2 plano-convex lens (f = 75 mm, Edmund Optics GmbH, GER) that focused the laser beam onto the microbeam.

In order to monitor the ionization region by stroboscopic imaging, a CCD camera (DBK 41 AU02, The Imaging Source, GER) was used. On the opposite side of the ionization region, a red stroboscopic diode (LED and electronics by Autodrop AD-K-901, microdrop Technologies GmbH, GER) was mounted within the optical axis of the CCD camera. The diode power supply unit was triggered by the OPO laser Q-switch output signal via a delay generator (PDG 204, S.M.V. München, GER) to correct for any optical and electrical delays and to observe different points in time before and after the laser impact on the free-standing liquid beam.

The IR laser dispersed a volume of the liquid beam, generating analyte ions. The ionized analytes entered the heated transfer tube, where desolvation took place. The ions were then pulsed into the IM spectrometer for 140–340 μs (pulse width), where they were separated according to their size and shape and detected by a Faraday plate (20 mm diameter), coupled to an amplifier (1 GV/A, custom-built by ISAS, GER) and then fed to an oscilloscope (TDS 5052 PDO, Tektronix Inc., USA) for data acquisition.

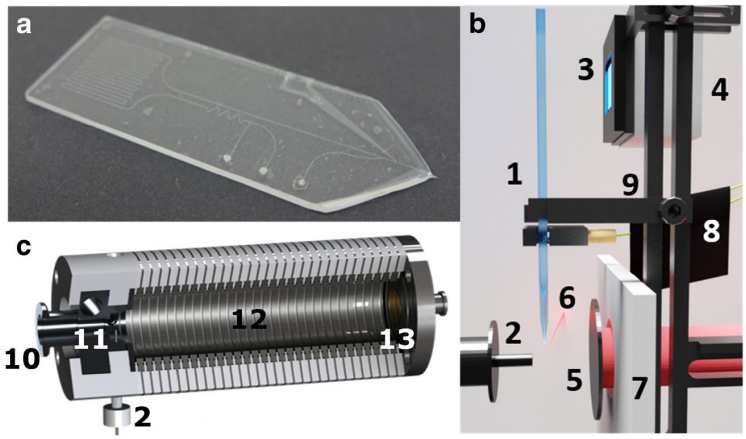

Fig. 2 **a** Microchip used in this study. **b** Layout of chip setup in front of IM spectrometer inlet with a side view of the microfluidic chip (1), the IM spectrometer inlet (2), the LED positioned in front of the chip reactor region (3), the LED cooler (4), the counter electrode (5), the laser beam (6), a PTFE insulation plate (7), the capillary system and microchip mount including clamps (8), and a fine positioning stage (9). **c** In-house-built IR-MALDI IM spectrometer with heated inlet in top view, inlet (2) at the bottom-left is equivalent to (2) of panel **b**, the pump inlet (10), the pulsed ion inlet (11), the drift tube (12), and the faraday plate (13) as the detection element

The heated transfer tube (200 °C) bridges the different pressure regimes: the ambient pressure ionization region and the reduced pressure IM spectrometer (100 mbar N_2, 0.3 L/min N_2, 60 °C, 212 mm drift tube, 140–340 μs pulse width, and 300–540 μs pulse delay). After the laser pulse was released, the laser triggered the electric potential switch of the ion pulsing via a delay generator and a fast high-voltage switch (GHTS 30, Behlke Power Electronics GmbH, GER). The system was usually operated with a pulse delay of 310 μs, a pulse width of 140 μs, and a repetition rate of 20 Hz. This resulted in a resolving power (defined as drift time over full width at half maximum) of 20–40 for the system, which is sufficient to separate the two isomers well enough without compromising the sensitivity. It also allows the calculation of the yield for each species by a simple cumulative Gaussian fit.

Results

Photoreaction An example of a visible light–catalyzed photoreaction is the isomerization of the *E*-isomer, ***E*-1**, to the corresponding *Z*-isomer ***Z*-1** by photocatalysts (see reaction scheme 1). After excitation of the photocatalyst by visible light, the reaction, based on triplet energy transfer, can occur yielding the *Z*-isomer ***Z*-1**. After breaking the π bond, the energy transfer leads to the formation of a delocalized biradical electron system [15] as an intermediate that allows the C-C bond to rotate. The discrimination of both isomers is based on the deconjugation of the π system of the *Z*-isomer, in which the side chain is sterically rotated out of the plane of the aromatic system. This increases the triplet energy of the *Z*-isomer and renders triplet energy transfer from the catalyst to the *Z*-isomer. This makes re-isomerization of the *E*-isomer infeasible.

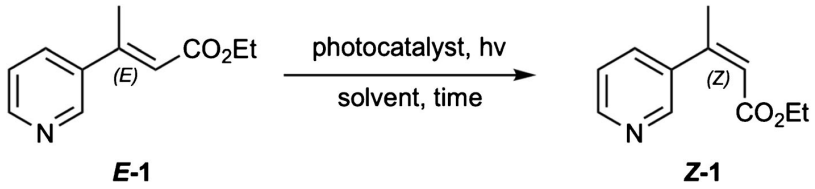

***E*-1** ***Z*-1** (1)

In addition to photocatalysts such as riboflavin (**L**), a number of other photocatalysts for which this isomerization has already been observed, were also investigated in this work [15]. A summary is given in Table 1.

ESI/IR-MALDI IM detection of *E*/*Z* isomers The advantage of drift tube IM spectrometry, compared with MS, is the facile differentiation of isomeric compounds, and the reduced measuring time compared with chromatographic methods. Similar

Table 1 Overview of photocatalysts investigated

Name	Label	$E_{TRIPLET}$ (kJ/mol)
$[Ru(bpy)_3](PF_6)_2$	A	195 [10]
$[Ru(phen)_3]$ Cl_2	B	196 [10]
Rose Bengal	C	198 [15]
$[Ru(bpz)_3](PF_6)_2$	D	201*
Mes-Arc$^+ClO_4^-$	E	205 [37]
9-Fluorenone	F	209 [38]
Eosin Y	G	210 [39]
$[Ir(dtbbpy)(ppy)_2]PF_6$	H	212 [40]
Rhodamine 6G	I	218 [41]
4CzIPN	J	220*
fac-Ir(ppy)$_3$	K	232 [10]
Riboflavin	L	234*
$[Ir[dF(CF_3)ppy]_2(dtbbpy)]PF_6$	M	252*
$[Cu(dap)_2]Cl$	N	160 [42]

*Experimental data can be found in the ESM

to MS, the composition of the reaction mixture in flow reactors can be determined in real time. The combination of both properties, the differentiation of isomeric compounds and the real-time analysis, makes drift tube IM spectrometry attractive for reaction monitoring. The ionization of the components of the reaction mixture should be carried out gently. If polar or aqueous solvents are used, IR-MALDI can be applied alternatively to ESI. As demonstrated in Fig. 3, the *E*- and *Z*-isomers of ethyl cinnamate derivative ***E*-1** and ***Z*-1** were successfully ionized by both methods. The IM spectra also show that both isomers were well separated in the IM spectrometer. An IM spectrometer working at AP was used to obtain the ESI-IM spectra. In the remainder of this work, IR-MALDI was used as the ionization method. IR-MALDI has distinct advantages over ESI. These include the formation of ions that are usually only singly or doubly charged, the softer ionization of the analytes, for example, for electrochemically reactive substances, and the higher sensitivity in combination with pulsed analysis methods (time-of-flight). Another important contribution to this work is the ability of IR-MALDI to tolerate high water contents and wide ranges of flow rates. The flow rate within the reaction channel on the microchip was typically 0.3–1 μL/min and within the flow reactor 1–3 μL/min, so that a high reaction rate was realized. At the microchip and capillary reactor outlet, the liquid stream of the reaction mixture was mixed with a liquid stream of a MeCN/H_2O mixture (100 μL/min and 300 μL/min). This stopped the reaction, diluted the reaction mixture, and achieved an optimal solvent composition for subsequent analysis. While the resulting flow rate was optimal for IR-MALDI because it created a microbeam which was sampled by the IR-laser, this flow rate would have been too high for the combination of ESI and the IM spectrometer.

Monitoring of the photocatalyzed *E*/*Z* isomerization In the beginning of the reaction, ethyl cinnamate derivative ***E*-1** was exclusively detected at the outlet of the photoreactor with the light source switched off. After switching on the light source, a peak just in front the *E*-isomer appeared, which can be assigned to the corresponding *Z*-isomer ***Z*-1**. This can be seen in the IM spectrum (Fig. 4), in which both isomer peaks appear. The peak at a drift time of 4.74 ms can be assigned to the *Z*-isomer and the peak at 5.01 ms to the *E*-isomer. From the fraction ratio of the peak areas of both

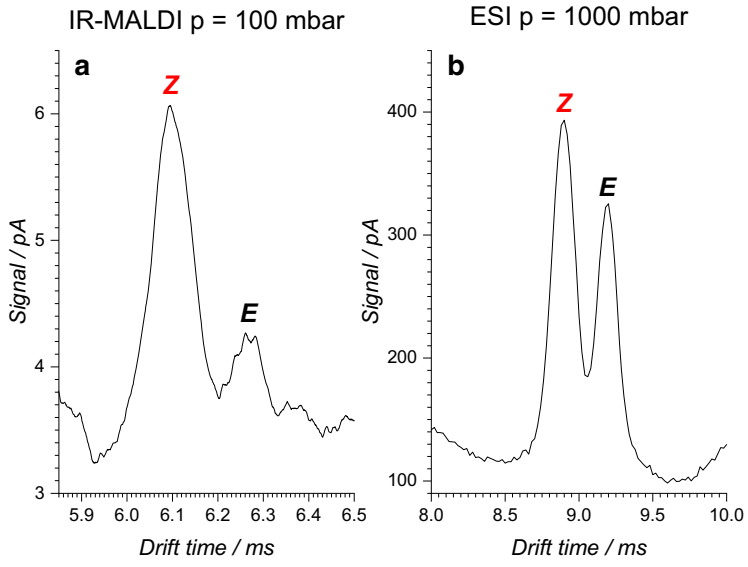

Fig. 3 Comparison of IM spectra of 50:50 mol% *E*/*Z* mixtures of an ethyl cinnamate derivative ***E*-1**: **a** IR-MALDI-IM spectrum at 100 mbar and **b** ESI-IM spectrum at an ambient pressure. Differences in relative and absolute intensity of the isomers arise from the different charge transfer equilibria for the different techniques and pressures. In both cases, a good separation between the *E*- and the *Z*-isomer was achieved

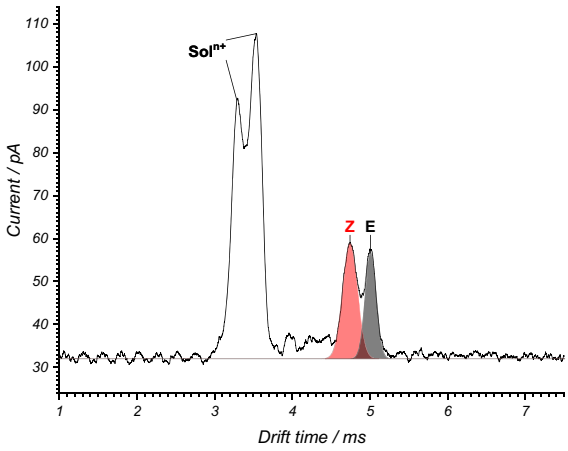

Fig. 4 IM spectrum of the *E*- and *Z*-isomer of ethyl cinnamate derivatives ***E*-1** and ***Z*-1** with their drift time maxima at 5.01 ms and 4.74 ms, respectively

isomeric peaks, the reaction yield can be derived after consideration of the calibration function.

Calibration While the ionization, and thus the detection efficiency, of different substances varies greatly for ESI or IR-MALDI, and more so for API-MS, no major change is generally expected for isomeric compounds such as the two *E*/*Z* isomers. However, we found that the yields of the photoreactions in the flow reactor obtained by simple peak integration did not follow such a linear trend, and calibration function was recorded in order to correct for this (Fig. 5).

The calibration function (inset in Fig. 5 with linear scaled axes) shows a strong non-linear behavior. It can be concluded that the ionization efficiencies of the *E*-isomer and the *Z*-isomer differ significantly. A significantly larger peak area is observed for the *Z*-isomer than should be expected for the corresponding concentration. Logarithmization resulted in a linearized calibration function (Fig. 5). This correlation allows a sensitive detection of small amounts of the reaction product (*Z*-isomer) and thus the typically rather low reaction yields that are observed in the flow reactor setup according to the short reaction time. In contrast, the calibration function (inset in Fig. 5) for larger yields shows a flatter curve. Consequently, the determination of higher yields is therefore less precise.

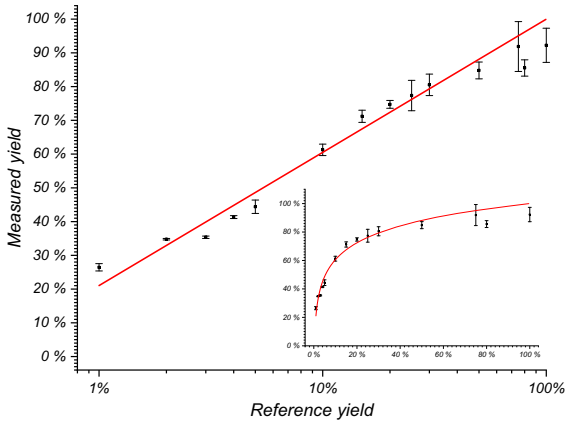

Fig. 5 Calibration function for *E*/*Z* isomer mixtures for the IR-MALDI-IMS setup in a semi-logarithmic plot, with $R^2 = 0.994$, $n = 14$. The inset shows the calibration function for linearly scaled axes. The measured yield is the signal integral $\boldsymbol{Z}/(\boldsymbol{Z} + \boldsymbol{E})$ in the measured spectrum. The reference yield refers to the actual molar fraction of the *Z*-isomer

The preferred detection of the *Z*-isomer is a result of a proton transfer reaction from the *E*-isomer to the *Z*-isomer. This protonation can happen either within the nanodroplets (protonation equilibrium) or in the gas phase. The latter, as they occur later, probably determine the protonation ratio. To evaluate the charge transfer equilibrium in the gas phase, the proton affinity of the two isomers was obtained by DFT calculations at the B3LYP/6-311+G(d,p) level. The corresponding energy-optimized structures (side and top views) are shown in Fig. 6. The important structural parameter here is the dihedral angle between the aromatic ring plane and the conjugated double bond. With increasing dihedral angle, the conjugation between aromatic ring and double bond weakens until the conjugation is lost and the π system is restricted to the aromatic ring. This change will affect the proton affinity of the nitrogen atom in the pyridine ring and therefore the proton affinity of the entire molecule. From the *E*- and *Z*-isomers, the dihedral angle increases from 36.6 to 55.8° because it is more energetically favorable, as the steric hindrance in the *Z*-isomer is reduced. This change is associated with an increase in proton affinity from 936.4 to 964.5 kJ/mol for the *E*- and the *Z*-isomers, respectively. This difference in the proton affinity of both isomers may explain the shape of the calibration curve.

Pressure dependence of charge transfer reactions One possibility of suppressing charge transfer reactions was the reduction of pressure, which is associated with a reduction of the collision frequency of the ions in the ionization region and thus the number of reactive collisions. To determine the influence of pressure on the ratio of protonated ions of *Z*- and *E*-isomers, a mixture consisting of 95 mol% *E*-isomer and 5 mol% *Z*-isomer was investigated by IR-MALDI-IM spectrometry in the pressure range between 5 and 200 mbar (Fig. 7). Since the drift voltage was kept constant as the pressure was varied, the ions were detected at lower drift times with decreasing pressure. This reduces the residence time of the ions in the IM spectrometer and thus the number of possible reactive collisions in the surrounding of the transfer capillary.

An essential result of these investigations was the change in the ratio of the peak intensities of the two isomers with varying pressure. Thus, the peak intensity of the *Z*-isomer becomes significantly smaller in relation to the peak intensity of the

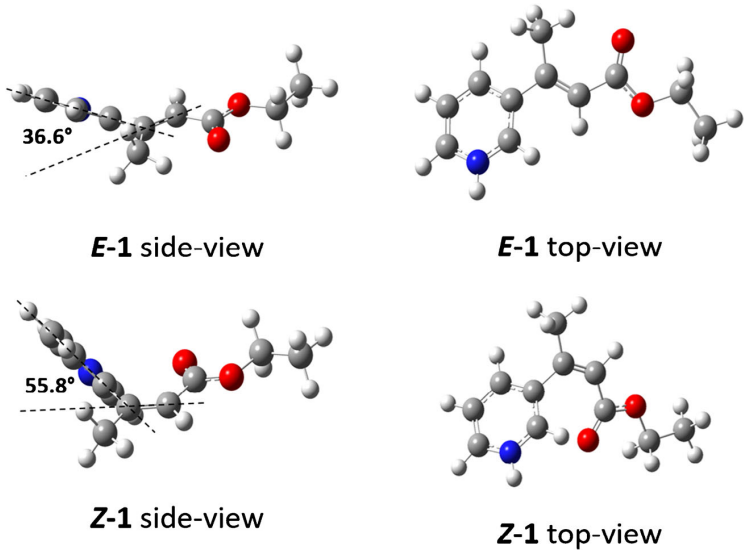

Fig. 6 Side and top views of the structures of the *Z*/*E*-isomers, ethyl cinnamate derivatives ***E*-1** and ***Z*-1** (DFT: B3LYP/6-311+G(d,p))

E-isomer with decreasing pressure. The reason is charge (proton) transfer reactions from protonated *E*-isomer to neutral *Z*-isomer due to its higher proton affinity. At atmospheric pressure, a thermodynamic equilibrium between *E*- and *Z*-isomer ions is established due to the high collision frequency. Decreasing the pressure reduces the collision frequency and increases the probability that *E*-isomer ions survive and arrive at the detector.

Although the IM spectrometer should be optimally operated at 5–10 mbar to suppress charge transfer reactions as much as possible, a pressure of 100 mbar was applied in this work. Pressures of 5–10 mbar result in drift times of only a few hundred microseconds. Currently, no amplifiers are commercially available that allow sufficiently fast detection of ions with such drift times, low noise, and amplification factors larger than 1 GV/A. The reduction of charge transfer effects, good sensitivity, and overall performance at 100 mbar were the reason to choose this pressure in the IM spectrometer for the remainder of this work.

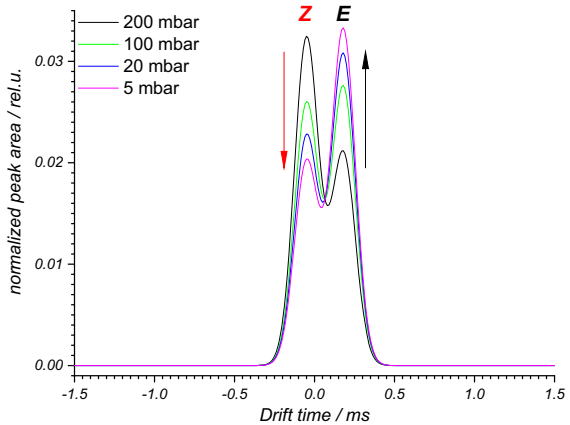

Fig. 7 IM peaks for an ***E*-1** and ***Z*-1** 95:5 mol% mixture in dependence of the pressure; for the sake of clarity, only area-normalized and time-scaled (drift-time shifted and peak-width normalized) fit functions are shown

The influence of the pressure seemed somewhat surprising, since the dispersion of the liquid occurs at an atmospheric pressure. However, this event took place directly at the inlet of the transfer capillary. The nanodroplets initially formed thus evaporate to a large extent within the heated capillary and in the drift tube of the IM spectrometer, in which the pressure was reduced. This was also where charge transfer reactions took place. With complete suppression of the charge transfer reactions, the ratio of the peak areas should be 5:95, which is not the case. This indicated that a part of the isomer ions was already released at AP or that some transfer reactions still took place in the drift tube at 100 mbar.

Photoreaction on the microchip The time sequence of the experiment is shown in Fig. 8. At time $t = 0$ s, the reaction mixture was injected into the flow reactor. No *E*-isomer is yet detected at the reactor outlet output. At a flow rate of 1 µL/min, an initial *E*-isomer signal was observed after circa 70 s. The LED was switched on at $t = 150$ s to trigger the conversion of the starting material by excitation of the photocatalyst. After a short delay, a continuous decrease of the *E*-isomer signal and an increase of the *Z*-isomer signal were observed. About 30 s after switching on the light source, a stationary state characterized by the maximum conversion of the reaction from *E*- to *Z*-isomers was reached. When the light source was switched off, the concentration of the *Z*-isomer drops and the initial concentration of the *E*-isomer was approximately restored.

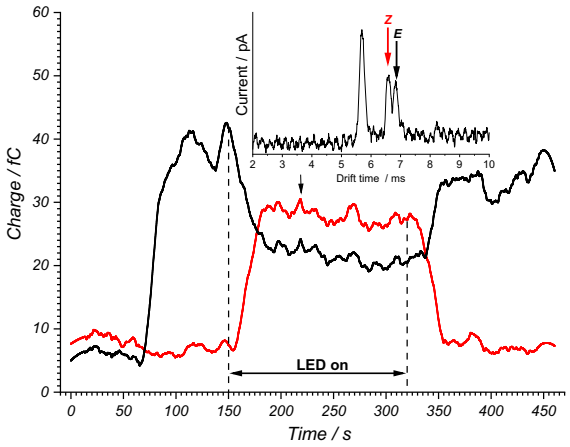

Fig. 8 IR-MALDI-IM signals of the *E* isomer ***E*-1** (black) and *Z*-isomer ***Z*-1** (red) recorded over reaction time of the microchip reactor

The residence time, and thus the irradiation time, of the reaction mixture in the flow reactor was about 70 s, given a sample flow rate of 1 μL/min. Comparable reactions in a batch reactor, as described in the literature, run up 48 h [15]. However, a complete conversion is likely achieved earlier, possibly after several hours. In our exemplary batch reaction from [15], the GC-FID determined yield for the *Z*-isomer was 10% and 96% for riboflavin and 76% and 94% for *fac*-Ir(ppy)$_3$ after 2 h and 24 h irradiation time, respectively.

The influence of the catalyst concentration on the conversion of the *E*- to the *Z*-isomers is shown in Fig. 9. With increasing catalyst concentration (here **L**), an increase of the *Z*-isomer signal was observed in the stationary range. The inset in Fig. 9 shows that the stationary range was reached sooner with increasing catalyst concentration, given the response rate of the system rose from 0.1 to 0.9 fC/s. At a higher catalyst concentration, it seemed that a plateau in the product concentration was reached. The maximum concentration of 2 mol% for the catalysts that was used in this work, resulted from the maximum solubility of the catalysts in the final reaction mixture with MeCN/H_2O 1:1 (v/v) solvent required for IR-MALDI. This was less of concern for the batch preparations (5 mol%).

Multiple radiation sources The spectral overlap integral of the emission of the LED source ($\lambda = 404$ nm) and the absorption bands of the catalysts may vary greatly. In order to efficiently excite catalysts with varying absorption bands, multiple LEDs may be needed. We implemented an additional UV LED ($\lambda =$ 365 nm) with a 50 times lower intensity (see Fig. S1 in ESM). Still, Fig. 10 shows the product formation for catalyst **M** after sequential switching on and off of the LED light sources with a continuous flow of starting material through the capillary flow reactor. With this setup, that could be extended to even more light sources, we were able to screen the reaction mix with two radiation sources in less than 10 min. With wavelength-tunable light sources in mind, this concept could be extended to a large range of wavelengths. All of which could be continuously screened within one measurement. The shown yields of *Z*-isomer correspond the ratio of ***Z***/(***Z*** + ***E***) after calibration. Due to the lower photon density delivered by the 365-nm LED, a significant conversion could only be obtained for catalyst **M**, Ir(dF(CF$_3$)ppy)$_2$(dtbbpy)PF$_6$ (Fig. 11b). Catalyst **M** was also the most effective catalysts if the 404-nm LED was used (Fig. 11a).

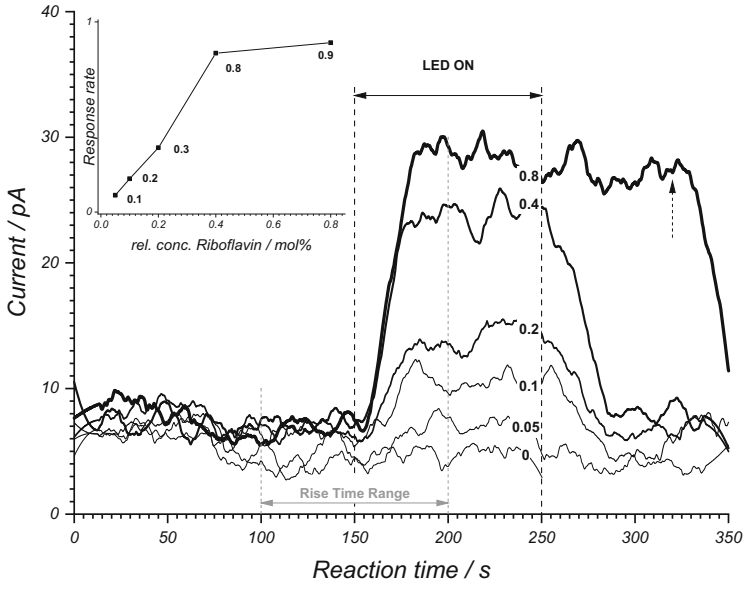

Fig. 9 IR-MALDI-IM signal of the *Z*-isomer (product) in dependence of the concentration of the photocatalyst used (0 to 0.8 mol%, from bottom to top with in increasing line width), in this case riboflavin **L**. Inset shows the maximum slope (between 150 and 200 s) and marks the minimum response time of the entire setup at 10 s with a maximum response rate of 0.9 fC/s. For a riboflavin concentration of 0.8 mol%, the irradiation was stopped at 320 s

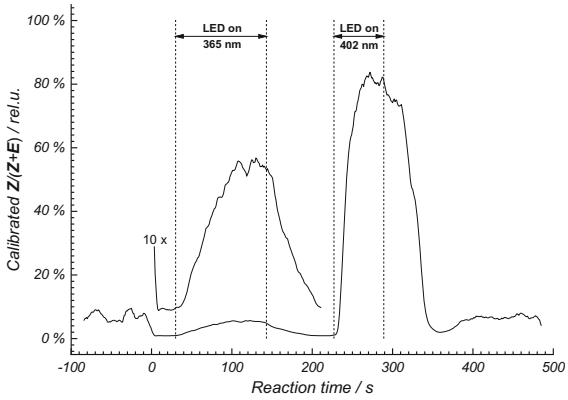

Fig. 10 Calibration-corrected yield of the *E*/*Z* isomerization for two different radiation sources, 404 nm and 365 nm sequentially applied to the photoinduced isomerization reaction carried out in the capillary flow reactor (catalyst **M**, $[Ir[dF(CF_3)ppy]_2(dtbbpy)]PF_6$, 2 mol% in MeCN)

Product yields The significantly shorter screening time compared with the several hours in a photo batch reactor makes reaction screening in a capillary or microchip photoreactor superior. In combination with flow injection analysis (FIA), this technique has potential for high-throughput analysis.

In this work, the reaction yield of photoisomerization was determined for a number of different photocatalysts (Table 1). These catalysts were characterized by their corresponding absorption in the UV/Vis range and a wide range of triplet energies. The results of the catalyst screening are shown in Fig. 11 as a representation of the reaction yield vs. the triplet energy of the catalyst. A more precise treatment would consider the kinetics of the energy transfer and *E*/*Z* isomerization.

Herkstroeter and Farid [43] were able to show that the logarithmic rate constants of the energy transfer of different acceptors display a characteristic behavior with respect to the triplet energies of the photocatalysts: from a strong increase in the endothermic regime, a plateau is reached in the exothermic

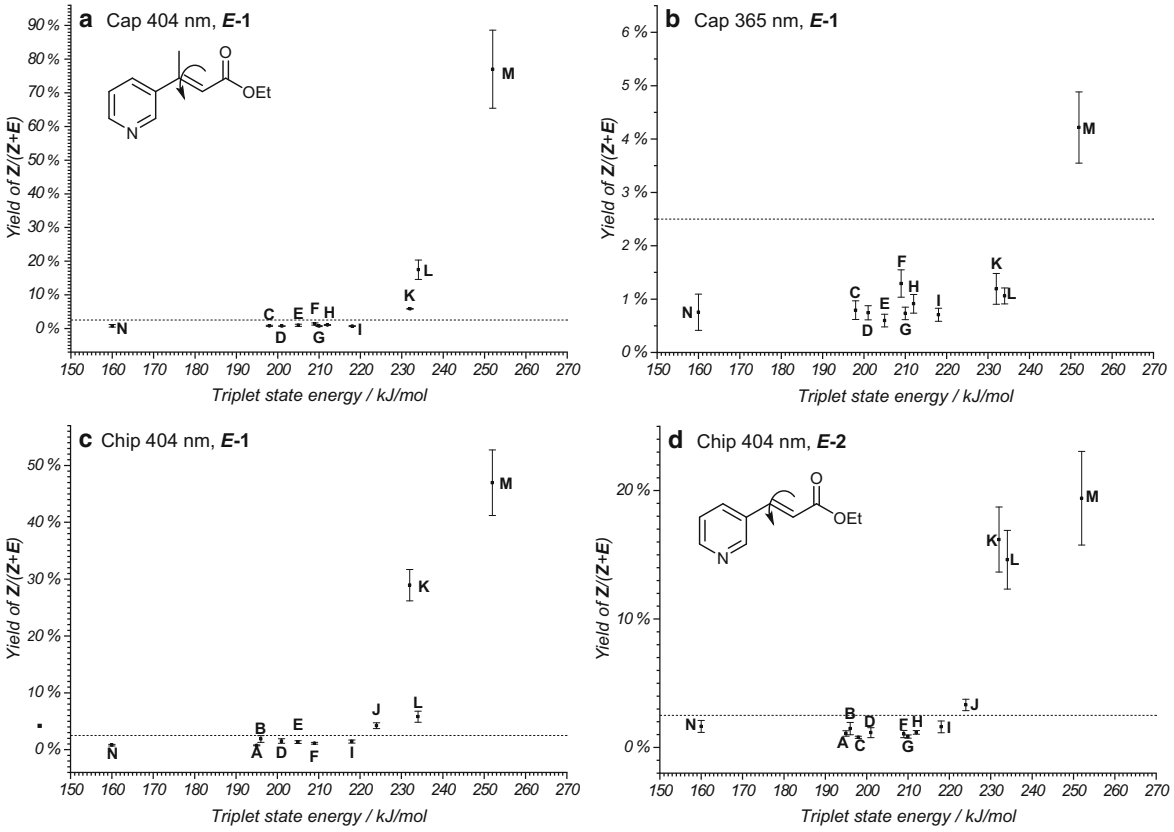

Fig. 11 Reaction yields of the *Z*-isomers from its *E*-isomer as starting material: **a** ethyl cinnamate derivative ***E*-1** in the capillary flow reactor at 404 nm excitation (Cap 404 nm, ***E*-1**), **b** ethyl cinnamate derivative ***E*-1** in the capillary flow reactor at 365 nm excitation (Cap 365 nm, ***E*-1**), **c** ethyl cinnamate derivative ***E*-1** in the microchip flow reactor at 404 nm excitation (Chip 404 nm, ***E*-1**), **d** ethyl cinnamate derivative ***E*-2** in the microchip flow reactor at 404 nm excitation (Chip 404 nm, ***E*-2**). Photosensitizing catalysts: **A**, $[Ru(bpy)_3](PF_6)_2$; **B**, $[Ru(phen)_3]Cl_2$; **C**, Rose Bengal; **D**, $[Ru(bpz)_3](PF_6)_2$; **E**, Mes-Arc$^+$$ClO_4^-$; **F**, 9-fluorenone; **G**, Eosin Y; **H**, $[Ir(dtbbpy)(ppy)_2]PF_6$; **I**, Rhodamine 6G; **J**, 4CzIPN; **K**, *fac*-$Ir(ppy)_3$; **L**, Riboflavin; **M**, $[Ir[dF(CF_3)ppy]_2(dtbbpy)]PF_6$; **N**, $[Cu(dap)_2]Cl$. The dashed line at 2.5% represents the threshold of the reaction onset and results from reference measurements, and their standard errors, containing no *Z*-isomer

limit [39]. Since analogous measurements were not possible in the experiment described here and, in addition, the kinetics of the overall reaction is more complex, the presentation of the results seen in Fig. 11 was chosen. This representation also allowed direct comparison to results published by Metternich and Gilmour [15].

Metternich and Gilmour have shown a similar correlation for the related substrate ethyl-3-phenylpent-2-enoate in photo batch reactor experiments. This correlation was characterized by a sharp increase in the yield of the *Z*-isomer from a triplet energy of 179 kJ/mol (anthracene as photosensitizer), the formation of a plateau with yields of over 95% (with 2 sensitizers at 60% and 72%), and a drop in yield at a triplet energy of 255 kJ/mol (Fig. 4 in supplementary information of [14]). In that work, a long reaction time of 24 h forced a complete conversion from the *E*-isomer to the *Z*-isomer, thereby effectively masking nuances in the sensitizing efficiency.

In contrast, these small differences in reactivity were more clearly visible in the flow reactors due to the significantly shorter reaction times. Within the scope of a screening, only reaction conversions for the most reactive catalysts were observed. This most reactive catalyst was **M**; however, **K**, **L**, and **J** were above the reaction threshold. Their triplet state energies are in the range of 220–250 kJ/mol. This detection of the most reactive catalysts is of particular importance for synthetic chemists and provides a fast and cost-efficient method for catalyst screening. For these catalysts, a complete conversion after 24 h reaction time was observed by Metternich and Gilmour [15].

The significant decrease of the reaction time in both flow reactors was certainly due to the more homogeneous irradiation of the reaction mixture with an optical layer thickness in the range of less than 75 μm (capillary reactor 75 μm diameter, microchip reactor 20–30 μm channel depth, 100 μm channel width). In contrast, in batch reactors at a high optical density, only a very small volume of the reaction mixture is continuously irradiated. On the other hand, by varying the flow of the starting materials, or even going to stop flow, an extension of the reaction time can be achieved. By doing so, the photoreactions of other catalysts can also be detected.

Figure 11 a and c compare the yields of both photo flow reactors for irradiation at $\lambda = 404$ nm. In both flow reactors, only the conversions of the reaction under participation of the above-mentioned catalysts were observed, meaning a good qualitative agreement was obtained. While an absolute agreement of the yields cannot be expected due to the different irradiation conditions in both reactors, strong deviations in the relative yields of the catalysts **M** and **L** were observed. Besides the ethyl cinnamate derivate ***E*-1**, a second structurally related *E*-isomer of ethyl-3-(pyridine-3-yl)prop-2-enoate ***E*-2** that is without the methyl group of ethyl cinnamate derivative ***E*-1**, was investigated (Fig. 11d). Comparison of the yields in Fig. 11 c and d reveals a qualitatively similar reaction behavior. The most reactive catalyst was again **M**, with **K**, **L**, and **J** above the threshold. However, yields for *Z*-isomer were lower for this ethyl cinnamate derivative as the missing methyl group leads to a decreased steric constrains in the *Z*-isomer and inferior deconjugation of the π system. Thus, the triplet energy of the formed *Z*-isomer ***Z*-2** is lower than for *Z*-isomer ***Z*-1**, which also allows for back-isomerization of ***Z*-2** to the *E*-isomer ***E*-2** by triplet energy transfer.

Conclusions and outlook

Using a novel combination of photo flow reactors with an IR-MALDI-IM spectrometer, we found catalyst **M** and also **K**, **L**, and **J** to be effective and efficient sensitizers for the *E*/*Z* isomerization of ethyl cinnamate ***E*-1**. Irradiation time sequences from 10 to 180 s yielded conversion rates of up to 80% and allowed us to identify these four best performing catalysts out of a set of 14 different photocatalysts within only minutes of measurement time for each. When compared with current studies found in the literature, this approach helps to drastically reduce the measurement times to only a few minutes per scan. In addition, given the much smaller volume of the reaction vessel, only 2 nmol (20 μL of a 100 μM solution) of catalyst was used for a single scan compared with 5 μmol of catalyst used in a single reaction with a batch reactor setup. Especially in the context of valuable iridium- and ruthenium-based catalysts, this certainly constitutes an improvement in cost and resource efficiency.

In the future, wavelength-tunable light sources could be used for directly subsequent irradiation periods due to the fast scanning time of the setup. This approach could make wide ranges of wavelengths accessible to reaction performance tests in short timescales. Such an approach would be infeasible in batch reaction–based screening systems.

Funding Open Access funding provided by Projekt DEAL. This work was funded by the Deutsche Forschungsgemeinschaft (DFG, German Research Foundation)—project number 275653032 (FOR 2177).

Compliance with ethical standards

Conflict of interest The authors declare that they have no conflict of interest.

References

1. McQuade DT, Seeberger PH. Applying flow chemistry: methods, materials, and multistep synthesis. J Organomet Chem. 2013;78(13):6384–9.
2. Gilmore K, Seeberger PH. Continuous flow photochemistry. Chem Rec. 2014;14(3):410–8.
3. Stolz F, Appun J, Naumov S, Schneider C, Abel B. A complex catalytic reaction caught in the act: intermediates and products sampling online by liquid μ-beam mass spectrometry and theoretical modeling. Chempluschem. 2017;82(2):233–40.
4. Tucker JW, Zhang Y, Jamison TF, Stephenson CRJ. Visible-light photoredox catalysis in flow. Angew Chem Int Ed. 2012;51(17):4144–7.
5. Plutschack MB, Pieber B, Gilmore K, Seeberger PH. The Hitchhiker's guide to flow chemistry. Chem Rev. 2017;117(18):11796–893.
6. Schulze S, Pahl M, Stolz F, Appun J, Abel B, Schneider C, et al. Liquid beam desorption mass spectrometry for the investigation of continuous flow reactions in microfluidic chips. Anal Chem. 2017;89(11):6175–81.
7. Heiland JJ, Warias R, Lotter C, Mauritz L, Fuchs PJW, Ohla S, et al. On-chip integration of organic synthesis and HPLC/MS analysis for monitoring stereoselective transformations at the microscale. Lab Chip. 2017;17(1):76–81.
8. Warias R, Zaghi A, Heiland JJ, Piendl SK, Gilmore K, Seeberger PH, et al. An integrated lab-on-a-chip approach to study heterogeneous enantioselective catalysts at the microscale. ChemCatChem [Internet]. 2018 7 [cited 2020 Feb 20];10(23):5382–5. Available from: https://onlinelibrary.wiley.com/doi/abs/10.1002/cctc.201801637
9. Lotter C, Poehler E, Heiland JJ, Mauritz L, Belder D. Enantioselective reaction monitoring utilizing two-dimensional heart-cut liquid chromatography on an integrated microfluidic chip. Lab Chip [Internet]. 2016 29 [cited 2020 Feb 20];16(24):4648–52. Available from: http://xlink.rsc.org/?DOI=C6LC01138A
10. Prier CK, Rankic DA, MacMillan DWC. Visible light photoredox catalysis with transition metal complexes: applications in organic synthesis. Chem Rev [Internet]. 2013;113(7):5322–63 Available from: https://pubs.acs.org/doi/10.1021/cr300503r.
11. Narayanam JMR, Stephenson CRJ. Visible light photoredox catalysis: applications in organic synthesis. Chem Soc Rev. 2011 Jan;40(1):102–13.
12. Cambié D, Dobbelaar J, Riente P, Vanderspikken J, Shen C, Seeberger PH, et al. Energy-efficient solar photochemistry with luminescent solar concentrator based photomicroreactors. Angew Chem Int Ed. 2019;58(40):14374–8.
13. Cambié D, Noël T. Solar photochemistry in flow. Top Curr Chem. 2018;376(6):45.
14. Schultz DM, Yoon TP. Solar synthesis: prospects in visible light photocatalysis. Science (80-) [Internet]. 2014;343(6174):1239176 Available from: https://www.sciencemag.org/lookup/doi/10.1126/science.1239176.
15. Metternich JB, Gilmour R. A bio-inspired, catalytic E → Z isomerization of activated olefins. J Am Chem Soc. 2015 Sep;137(35):11254–7.
16. Mogensen KB, Kutter JP. Optical detection in microfluidic systems. Electrophoresis [Internet]. 2009 [cited 2020 Feb 20];30(S1):S92–100. Available from: http://www.ncbi.nlm.nih.gov/pubmed/19517511.
17. Ymeti A, Greve J, Lambeck P V., Wink T, van Hövell, Beumer, et al. Fast, ultrasensitive virus detection using a young interferometer sensor. Nano Lett [Internet]. 2007 Feb [cited 2020 Feb 20];7(2):394–7. Available from: https://pubs.acs.org/doi/10.1021/nl062595n
18. Ohla S, Beyreiss R, Scriba GKE, Fan Y, Belder D. An integrated on-chip sirtuin assay. Electrophoresis [Internet]. 2010 [cited 2020 Feb 20];31(19):3263–7. Available from: http://doi.wiley.com/10.1002/elps.201000220
19. Pfeiffer SA, Rudisch BM, Glaeser P, Spanka M, Nitschke F, Robitzki AA, et al. Continuous purification of reaction products by micro free-flow electrophoresis enabled by large area deep-UV fluorescence imaging. Anal Bioanal Chem. 2018;410(3):853–62.
20. Rudisch BM, Pfeiffer SA, Geissler D, Speckmeier E, Robitzki AA, Zeitler K, et al. Nonaqueous micro free-flow electrophoresis for continuous separation of reaction mixtures in organic media. Anal Chem. 2019;91(10):6689–94.
21. Zitzmann FD, Jahnke HG, Pfeiffer SA, Frank R, Nitschke F, Mauritz L, et al. Microfluidic free-flow electrophoresis based solvent exchanger for continuously operating lab-on-chip applications. Anal Chem [Internet]. 2017 [cited 2020 Feb 20];89(24):13550–8. Available from: http://www.ncbi.nlm.nih.gov/pubmed/29164853.
22. Meier TA, Beulig RJ, Klinge E, Fuss M, Ohla S, Belder D. On-chip monitoring of chemical syntheses in microdroplets via surface-enhanced Raman spectroscopy. Chem Commun. 2015;51(41):8588–91.
23. Xie W, Grzeschik R, Schlücker S. Metal nanoparticle-catalyzed reduction using borohydride in aqueous media: a kinetic analysis of the surface reaction by microfluidic SERS. Angew Chemie - Int Ed [Internet]. 2016 [cited 2020 Feb 20];55(44):13729–33. Available from: http://doi.wiley.com/10.1002/anie.201605776
24. Yue S, Ye W, Xu Z. SERS monitoring of the Fenton degradation reaction based on microfluidic droplets and alginate microparticles. Analyst. 2019;144(19):5882–9.
25. Andersen NI, Artyushkova K, Matanović I, Hickey DP, Minteer SD, Atanassov P. Spectro-electrochemical microfluidic platform for monitoring multi-step cascade reactions. ChemElectroChem [Internet]. 2019 2 [cited 2020 Feb 20];6(1):246–51. Available from: http://doi.wiley.com/10.1002/celc.201800578
26. Carrascosa E, Bull JN, Scholz MS, Coughlan NJA, Olsen S, Wille U, et al. Reversible photoisomerization of the isolated green fluorescent protein chromophore. J Phys Chem Lett [Internet]. 2018;9(10):2647–51 Available from: https://pubs.acs.org/doi/10.1021/acs.jpclett.8b01201.
27. Coughlan NJA, Adamson BD, Gamon L, Catani K, Bieske EJ. Retinal shows its true colours: photoisomerization action spectra of mobility-selected isomers of the retinal protonated Schiff base. Phys Chem Chem Phys [Internet]. 2015;17(35):22623–31 Available from: http://xlink.rsc.org/?DOI=C5CP03611A.
28. Urner LH, Thota BNS, Nachtigall O, Warnke S, von Helden G, Haag R, et al. Online monitoring the isomerization of an azobenzene-based dendritic bolaamphiphile using ion mobility-mass spectrometry. Chem Commun [Internet]. 2015;51(42):8801–4 Available from: http://xlink.rsc.org/?DOI=C5CC01488C.
29. Zühlke M, Sass S, Riebe D, Beitz T, Löhmannsröben H-G. Real-time reaction monitoring of an organic multistep reaction by electrospray ionization-ion mobility spectrometry. Chempluschem. 2017;82(10):1266–73.
30. Piendl SK, Raddatz C-R, Hartner NT, Thoben C, Warias R, Zimmermann S, et al. 2D in seconds: coupling of chip-HPLC with ion mobility spectrometry. Anal Chem. 2019;91(12):7613–20.
31. Lotter C, Heiland JJ, Stein V, Klimkait M, Queisser M, Belder D. Evaluation of pressure stable chip-to-tube fittings enabling high-

speed chip-HPLC with mass spectrometric detection. Anal Chem. 2016;88(15):7481–6.
32. Gerhardt RF, Peretzki AJ, Piendl SK, Belder D. Seamless combination of high-pressure chip-HPLC and droplet microfluidics on an integrated microfluidic glass chip. Anal Chem. 2017;89(23): 13030–7.
33. Hoffmann P, Häusig U, Schulze P, Belder D. Microfluidic glass chips with an integrated nanospray emitter for coupling to a mass spectrometer. Angew Chemie Int Ed [Internet]. 2007;46(26):4913–6 Available from: http://doi.wiley.com/10.1002/anie.200605152.
34. Lotter C, Heiland JJ, Thurmann S, Mauritz L, Belder D. HPLC-MS with glass chips featuring monolithically integrated electrospray emitters of different geometries. Anal Chem. 2016;88(5):2856–63.
35. Villatoro J, Zühlke M, Riebe D, Riedel J, Beitz T, Löhmannsröben HG. IR-MALDI ion mobility spectrometry. Anal Bioanal Chem. 2016;408(23):6259–68.
36. Charvat A, Abel B. How to make big molecules fly out of liquid water: applications, features and physics of laser assisted liquid phase dispersion mass spectrometry. Phys Chem Chem Phys [Internet]. 2007;9(26):3335 Available from: http://xlink.rsc.org/?DOI=b615114k.
37. Benniston AC, Harriman A, Li P, Rostron JP, Van Ramesdonk HJ, Groeneveld MM, et al. Charge shift and triplet state formation in the 9-mesityl-10- methylacridinium cation. J Am Chem Soc. 2005;127(46):16054–64.
38. Chang CW, Sølling TI, Diau EWG. Revisiting the photophysics of 9-fluorenone: ultrafast time-resolved fluorescence and theoretical studies. Chem Phys Lett. 2017;686:218–22.
39. Meyer AU. Organic photoredox catalysis: oxidation of sulfur containing compounds and reduction of aryl halides. Univ Regensburg; 2017.
40. Lowry MS, Goldsmith JI, Slinker JD, Rohl R, Robert A, Pascal J, George G. Malliaras A, et al. Single-layer electroluminescent devices and photoinduced hydrogen production from an ionic iridium(III) complex. 2005;
41. Mayr T. Rhodamine 6G [Internet]. Fluorophoes data base. [cited 2020 Feb 18]. Available from: http://www.fluorophores.tugraz.at/substance/58. Accessed 18 Feb 2020.
42. Knorn M, Rawner T, Czerwieniec R, Reiser O. [Copper(phenanthroline)(bisisonitrile)] + -complexes for the visible-light-mediated atom transfer radical addition and allylation reactions. ACS Catal [Internet]. 2015;5(9):5186–93 Available from: https://pubs.acs.org/doi/10.1021/acscatal.5b01071.
43. Herkstroeter WG, Farid S. Photodimerization — relevant triplet state parameters of methyl cinnamate, diethyl 1,4-phenylenediacrylate and methyl 1-naphthylacrylate. J Photochem. 1986;35(1):71–85.

3.2 Liquid phase IR-MALDI and differential mobility analysis of nano- and sub-micron particles

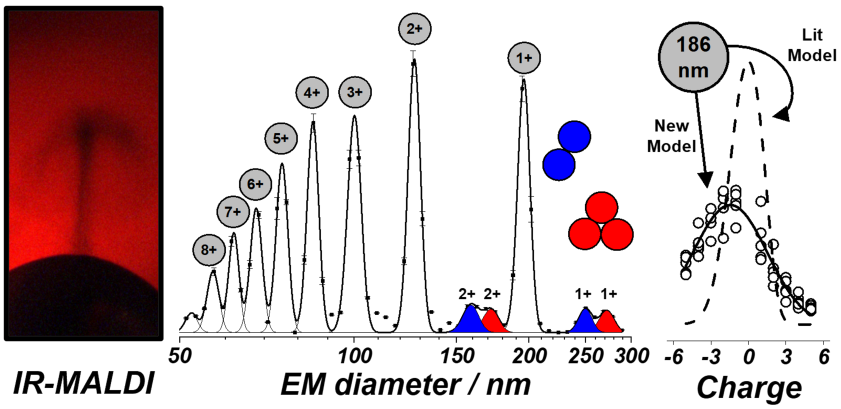

Figure 3.2: Graphical abstract of the publication as featured in the Journal of Physical Chemistry and Chemical Physics.

Scope of the publication This study succeeds the previous work with IR-MALDI in two ways. First, IR-MALDI was implemented as an ionization for differential mobility analysis, thus for particles greatly exceeding the realm of molecular dimensions. The outcome in terms of charging efficiency were compared to established charging methods such as electrospray and bipolar chargers (neutralizers). Second, the charge distribution of IR-MALDI was characterized since literature suggested different dependencies on the outcome of IR-MALDI charging. However, the charging models found in literature were exclusively based on molecular-sized compounds, such as salt clusters. The work presented shows a charging model newly derived from progressive iterations of the existing models.

Author's contribution My contribution to this study was the design and realization of the hanging-drop IR-MALDI interface with the DM analyzer. All measurement shown were conducted by me and evaluated using an independently developed background correction method. Various charge distribution models reported for IR-MALDI in literature were tested and evaluated on their performance on the obtained data. This resulted in the independent development of a new charge distribution model. Being the main editor of this manuscript, my responsibilities included, but were not limited to, its writing, editing as well as all data visualization steps.

PCCP

OF CHEMISTRY

PAPER

View Article Online
View Journal | View Issue

Cite this: *Phys. Chem. Chem. Phys.*, 2022, **24**, 2275

Liquid phase IR-MALDI and differential mobility analysis of nano- and sub-micron particles†

C. Prüfert, * J. Villatoro, M. Zühlke, T. Beitz * and H.-G. Löhmannsröben

Received 14th September 2021,
Accepted 1st January 2022

DOI: 10.1039/d1cp04196g

rsc.li/pccp

Infrared matrix-assisted desorption and ionization (IR-MALDI) enables the transfer of sub-micron particles (sMP) directly from suspensions into the gas phase and their characterization with differential mobility (DM) analysis. A nanosecond laser pulse at 2940 nm induces a phase explosion of the aqueous phase, dispersing the sample into nano- and microdroplets. The particles are ejected from the aqueous phase and become charged. Using IR-MALDI on sMP of up to 500 nm in diameter made it possible to surpass the 100 nm size barrier often encountered when using nano-electrospray for ionizing supramolecular structures. Thus, the charge distribution produced by IR-MALDI could be characterized systematically in the 50–500 nm size range. Well-resolved signals for up to octuply charged particles were obtained in both polarities for different particle sizes, materials, and surface modifications spanning over four orders of magnitude in concentrations. The physicochemical characterization of the IR-MALDI process was done *via* a detailed analysis of the charge distribution of the emerging particles, qualitatively as well as quantitatively. The Wiedensohler charge distribution, which describes the evolution of particle charging events in the gas phase, and a Poisson-derived charge distribution, which describes the evolution of charging events in the liquid phase, were compared with one another with respect to how well they describe the experimental data. Although deviations were found in both models, the IR-MALDI charging process seems to resemble a Poisson-like charge distribution mechanism, rather than a bipolar gas phase charging one.

1. Introduction

Infrared matrix assisted laser desorption and ionization (IR-MALDI) is a soft ionization technique that allows for the gentle transfer of large molecular structures into the gas phase. MALDI was developed in the late 1980s, and soon became the most widespread ion source for transferring biological samples into the gas phase.[1] MALDI is usually performed by embedding the species of interest into a solid matrix. The matrix absorbs the energy of the incident laser, undergoes ionization, and finally transfers its charge to the species of interest. This indirect ionization makes MALDI one of the most gentle forms of ionization. The combination of MALDI and mass spectrometry (MS) became one of the leading techniques for the visualization of biochemicals in cells and tissue. Soon after its inception, MALDI was performed with IR lasers.[2,3] The most recent advances in the field are the use of dual laser systems containing a IR-MALDI laser and a post-ionization laser yielding an increased signal-to-noise ratio in the MS spectra.[4,5]

University of Potsdam, Physical Chemistry, Karl-Liebknecht-Str. 24-25, Potsdam, Germany. E-mail: cpruefert@uni-potsdam.de, beitz@uni-potsdam.de

† Electronic supplementary information (ESI) available. See DOI: 10.1039/d1cp04196g

The usage and further development of IR-MALDI was primarily motivated by the strong absorption band of water in that wavelength region. Water, aside from being abundant and environmentally benign, is the native environment of biomolecules.[6] MALDI paved the way for a wide range of unprecedented investigations of large biomolecular structures directly from the liquid phase. In aqueous phase IR-MALDI, the liquid water absorbs the IR laser energy mainly below its surface.[7] This triggers a sub-surface phase explosion, which is a thermodynamic transition due to superheating beyond the liquid spinodal of water.[8–10] The transition occurs at such speeds that the randomly distributed charges contained in the liquid phase get dispersed into the separated sub-volumes, namely the droplets. These emerging micro- and nano-droplets contain a statistically distributed amount of charges and a net charge.[11] An alternative to other IR-MALDI liquid interfaces was developed,[12–14] which supplied the sample to the system *via* a hanging drop, greatly reducing clogging. This system has already been combined with ion mobility spectrometry.[15,16] Although phase explosions can occur in all liquid IR-MALDI systems, the geometry of the dispersion cloud may be very different. A hanging drop contains enough water to enable a recoil-induced material expulsion and therefore the

ions are ejected in a directed plume.[17,18] IR-MALDI inherently only creates ions or charged particles of low charge states. This is vital for the analysis of large particles, and for very charge-affine structures in general, because a very large number of charges would easily lead to undetectably low drag-to-charge ratios or to spectral congestion. Combined with the directed particle ejection from the plume, this makes IR-MALDI a viable technique for the directed transfer of the species into a differential mobility (DM) analyzer.

DM analysis is an analytical technique that characterizes the drag-to-charge ratio of nano to sub-micron particles (sMP). DM analysis determines the characteristic length of a particle as the aerodynamically normalized electrophoretic mobility (EM) diameter. A single peak in a DM spectrum is referred to as a monomobile fraction, since all particles in that fraction have the same electrophoretic mobility, and thus the same drag-to-charge ratio, in the gas phase. The monomobile fraction must be distinguished from a monomodal population, which represents particles that have the same diameter, and which is independent of the particle charge. Commercially available electrospray (ES) or nano-electrospray (nES) ionization is used to transfer solvated or suspended molecules or particles to the gas phase. The amount of charge that a particle or droplet can sustain strongly depends on its size, which is especially important for the analysis sMP since they are much larger than molecular structures normally investigated in ES. The EM diameter describes the drag-to-charge ratio of a particle thus a very large charge state may push the particle's EM diameter below the lower limit of detection of 2.5 nm for a standard water-based condensation particle counter. Because of that, nES must be accompanied by a soft X-ray or a radioactive source in order to be compatible with DM analysis. Soft X-ray or radioactive ionization reduces the amount of charge per particle. The soft X-ray or radioactive source generates a bipolar gas phase. This generates a defined charge distribution regardless of charge state of the incoming particles that is centered around very low charge states. Therefore, even large particles or molecules accumulate only a few charges, even if, for example, their proton affinity is high. This is especially advantageous, or even essential, for the analysis of charge-affine macromolecular structures, such as they often occur in nature. Current advances in the analysis of biological systems, such as liposomes and virus-like particles (VLCs), were achieved with a soft X-ray coupled nES source.[19,20] So far, the characteristic lengths of the particles or macromolecular structures investigated in the literature did not exceed 100 nm in diameter. This may in part be because nES is limited to small particle dimensions, so that a steadily balanced Taylor cone and liquid filament can be formed. It was described in the literature that even with the help of strong electric fields, particle dimensions that approach the dimension of the Taylor cone filament can distort or disrupt it completely.[21–24] This makes nES unsuitable for the analysis of sMP. This is where liquid-phase IR-MALDI can provide a solution: it can charge species of up to a few micrometers in EM diameter, as already shown in the literature.[25,26] In principle, its only size constraints arise from inherent mass limitations since heavier particle are harder to eject and transfer. On top of that, IR-MALDI is also an electric-field-free ionization method that therefore is also less prone to electrochemical side reactions.

Combing all the advantages mentioned above, the motivation for the presented work is grounded in two interests. Firstly, to offer a more feasible, complete, and practical setup for the size characterization of particles, particle populations and structures between 10 nm and 1000 nm in EM diameter. Secondly, to gain more detailed physicochemical insights into IR-MALDI from the aqueous phase. Here, the resulting particle charge distribution helps to pinpoint the nature of the charging process that happens in IR-MALDI. Both objectives are tackled using particle size standards. The data obtained was used to assess the analytical capabilities and dynamic range in terms of particle size, polydispersity, and concentration. Also, the data quality was sufficient to derive charge distributions and to compare different charging models to one another.

2. Experimental

2.1. IR-MALDI ionization chamber

The ionization chamber is a grounded aluminum cylinder (I.D. = 25.5 mm), sealed gas-tight at the top and bottom by IR-transparent CaF_2 windows (d = 25.4 mm).[27] The laser beam path runs through these windows coaxially. The transfer sheath gas stream was aligned midway between the two windows, perpendicular to the laser beam path, and across the cylinder's axis. The sample is introduced at this intersection *via* an SST capillary (32ga, TUB SS 304, Hamilton Company, US) supplied by a syringe pump (ALADDIN-1000, WPI Germany GmbH, GER). The sample capillary was aligned at a 45 degree angle with respect to the transfer sheath gas axis. An additional SST capillary (I.D. = 1 mm) was coaxially mounted the sample capillary to form a gas stream around the tip of the sample capillary. During a measurement, a particle-containing hanging drop forms at the tip of the sample capillary. Here, the laser hits the hanging drop and generates the aerosol. This aerosol is then picked up by the transfer sheath gas stream and guided to the DM analyzer *via* a 5 cm conductive rubber transfer tube. This transfer tube also contains a T-piece that provides pressure equalization to ambient conditions through a HEPA filter.

2.2. Electrospray generator

A commercially available setup (EAG 3482, TSI Inc, USA) is an X-ray coupled electrospray device which is operated in liquid-junction mode. The liquid-junction cross was replaced by an in-house built adapter made from PEEK that connects the glass emitter directly to an SST union. This greatly facilitated the capillary replacement and maintenance. As a solvent a 5–20 mM ammonium acetate aqueous solution was used. The EAG is usually operated with a 9 : 1 mixture of synthetic air and CO_2 and at total volume flow of 0.6 L min^{-1}. A voltage of (1.4 ± 0.005) kV was used to generate a current of (150–200) nA.

2.3. Laser and optics

For the setup we used a nanosecond IR laser pulse (λ = 2940 nm, f = 20 Hz, t = 6 ns, E = 0.9–3.5 mJ $\pm$ 0.1 mJ, IR Opolette 2940, OPOTEK, Carlsbad, CA, USA) that was guided through a (151 $\pm$ 1) cm long optical pathway along two gold mirrors (PF10-03-M01, THORLABS Inc., GER) and a CaF_2 plano-convex lens (f = 75 mm, Edmund Optics GmbH, GER) that focused the laser beam onto the hanging drop. To monitor the ionization region by stroboscopic imaging a CCD camera (DFK 41 AU02, The Imaging Source Europe GmbH, GER) was used. Along the CCD camera's optical axis, a red stroboscopic diode (LED and electronics from the Autodrop AD-K-901, Microdrop Technologies GmbH, GER) was mounted. The diode power supply unit was triggered by the OPO laser Q-switch output signal *via* a delay generator (PDG 204, S.M.V., GER) to correct for any optical and electrical delays and to observe different points in time before and after the laser impacts the hanging drop.

2.4. DM analyzer system

The differential mobility (DM) analyzer system is a commercially available screening mobility particle sizer (DMA 3081/3085/3085A, Classifier 3082, CPC 3788, AAN 3088) operated with the Aerosol Instrument Manager Software 10.2.0.11, all by TSI GmbH Co & KG, Germany.

2.5. Data treatment

The data was background corrected using an exponential decay function to correct for the long tailing that the solvent peak had up to the region of interest, which was only significant for small EM diameters. The spectra were fitted with multiple Gaussian peaks. When the width of a single peak is much smaller than a decade, the lognormally distributed peak can be approximated by a Gauss fit function. This was to reduce the fit function parameter space significantly, compared to using a lognormal fit function. This was omitted as soon as the FWHM of peaks exceeded half of a decade and lognormal fit function was used instead.

2.6. Chemicals

All silicate and polystyrene (PS) particles were purchased from micromod (micromod Partikeltechnolgie GmbH, Germany). All other chemicals and solvents were purchased from Millipore-Sigma (Merck KGaA, Germany). Both were used as received without further purification unless specifically indicated.

3. Results and discussion

3.1. Electrospray source

Electrospray ionization combined with subsequent charge neutralization by soft X-radiation was used for dispersing into the gas phase and charging sMP, as a reference method for the particle investigation with IR-MALDI. In the literature, most of the nES studies focus on particles smaller than 100 nm. This seems to be a size barrier for the nES ionization source. In this work, particles of 41, 95, 155 and 307 nm were measured, while only particles up to 155 nm in EM diameter could be measured under stable conditions. Since this is already at the uppermost limit (155 nm) of what is possible to spray with the nES setup, it was not possible to systematically investigate larger particles. A selection of the results from the soft X-ray coupled nES in that size regime are shown in Fig. 1.

The left panel in Fig. 1 shows the monomodal distributions of spherical plain silicate particles suspended in water at a mass concentration of 0.5 mg mL^{-1} before charge state correction. The spectrum for the 41 nm particles (dotted line) shows one monomobile fraction of the population containing only singly charged monomers. The 95 nm particles (dashed line) show two monomobile classes in the population with the singly-to-doubly charged species being about 6 : 1 in terms of population fraction. The largest sMP that we were able to spray with nES under stable operating conditions were the 155 nm particles. Here, the singly-to-doubly-to-triply charged species relation was 14 : 4 : 1 in terms of population fraction. Thus, the 155 nm particles contained about twice as many doubly charged species than the 95 nm particles did using nES as the charging method. The size-to-charge relation of aerosols is described by the Wiedensohler charge distribution. This is a model used to describe the distribution of the first two charge states of aerosols in both polarities. For charge states of three and higher, the Gunn charge distribution model is used.[28,29] By using both charge distributions, it is possible to deconvolute all monomobile fractions into their respective modal distributions.[30] Spectra thus deconvoluted are referred to as charge distribution corrected below. By doing so for the samples shown here, an almost monomodal size distribution of the particles can be ascertained (Fig. 1 panel b). Thus, it was possible to expand the analytical scope of the commercially available X-ray coupled nES to sMP of 155 nm in EM diameter.

3.2. Comparing IR-MALDI with nES

Spectra. As an alternative to charging by ES, IR-MALDI was used, which has some advantages compared to ES. In IR-MALDI, the sMP are ejected from a hanging drop. This drop is formed at the tip of a stainless-steel capillary which has a much larger inner diameter than fused silica capillaries conventionally used in nES or nES. This avoids clogging and leads to fewer adhesion effects, which are known to occur on glass surfaces for all sorts of particle species.[31,32] IR-MALDI uses five to ten times higher flow rates than nES, namely 1 and 0.1 µL min^{-1}, respectively. Its overall analytical performance compared with nES is shown in Fig. 2.

A suspension of plain 155 nm silicate particles was dispersed by nES from a 20 mM ammonium acetate solution. For IR-MALDI, the same particles were dispersed from an aqueous solution without any additives. Fig. 2 shows the background corrected spectra produced by IR-MALDI (red) which separates the different charge states of the particles according to their drag-to-charge ratio (mobility). The monomodal particle population of plain 155 nm silicate particles is separated into at least five clearly distinguishable monomobile fractions. The fraction

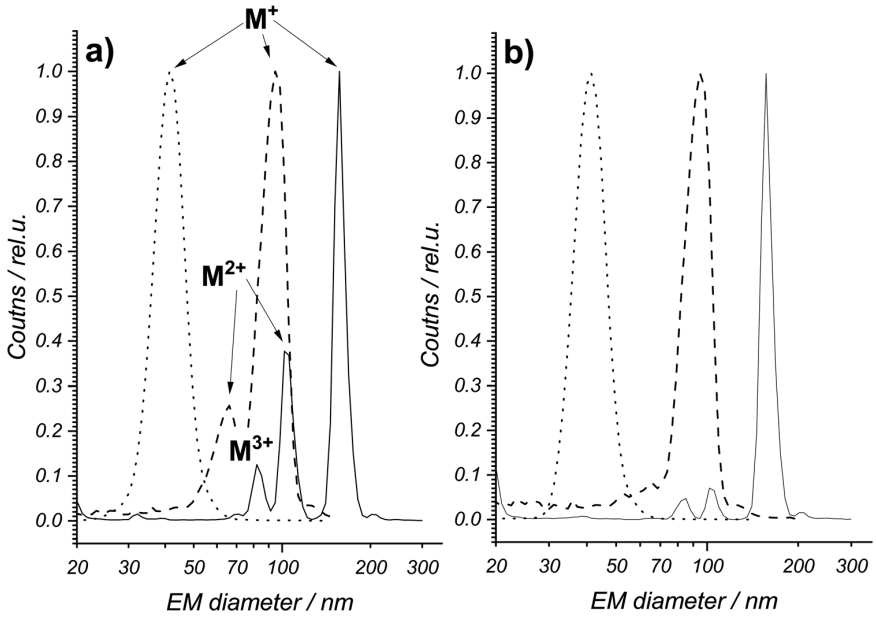

Fig. 1 Spectra of plain spherical silicate particles using nES for charging. The three particle populations are monomodal and centered around 41 nm (dotted line), 95 nm (dashed line), and 155 nm (continuous line) as their respective EM diameter for the singly charged monomer, (a) before charge state correction, (b) after charge distribution correction.

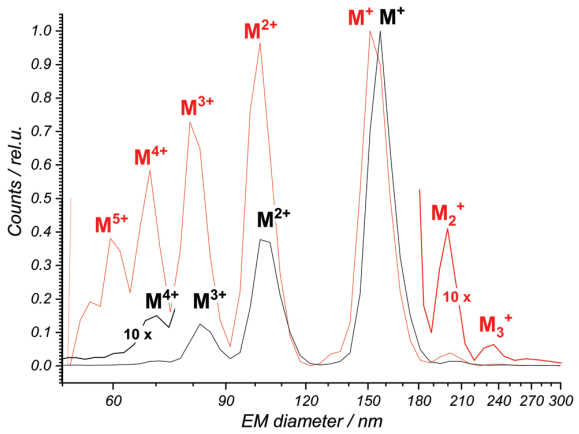

Fig. 2 Direct comparison of count-normalized EM spectra of monomodal plain silicate particles with a measured EM diameter of 155 nm charged with nES (black, from Fig. 1 uncorrected) and IR-MALDI (red), with the left end of the nES (black) and right end of the IR-MALDI spectrum (red) vertically zoomed-in by a 10-fold.

a charge state occupies within the total population of all charged particles decreases with increasing charge number. By comparing the signal from the IR-MALDI source (red) with the signal from the nES source (black), both charging methods show a similar analytical performance. nES shows the first three charge states (M^{+}–M^{3+}) clearly visible, and traces of the quadruply charged monomer (M^{4+}) as well as traces of singly charged dimer (not annotated in the spectrum). IR-MALDI on the other hand covers a wider range of species by including more charge states as well as more small clusters of particles. For the monomers, the first five charge states can be easily distinguished. The singly and doubly charged dimers are also visible. The singly charged trimer is also present in the spectrum. Due to this level of detail, the polydispersity index of the main particle fraction, defined as the ratio of the standard deviation squared over the peak center, was reduced from 0.014 (DLS) to 0.002 (DM) respectively. This was possible because DM analysis has a higher resolving power than DLS, which is especially interesting when it comes to multimodal distributions. It also becomes apparent that the resulting resolving power in the spectra shown is not limited by the DM analyzer itself, but by the inherent particle size distribution.

Fig. 3 shows the spectrum of the highest measured concentration of the particle suspension discussed in the concentration series later. The features in the spectrum are defined and numerous enough to not only discuss their intensity, but also the exact peak positions and peak widths. As shown in Fig. 3, next to the singly charged monomer signal in the spectrum at the highest concentration there is a singly charged dimer and trimer signal with an EM diameter of (253 ± 1) nm and (273.4 ± 0.4) nm, respectively. Each feature represents a single monomobile particle population, namely the singly charged dimer and trimer as well as their doubly charged counterparts. The larger the sheath gas flow rate is, the shorter is the particle's residence time in the DM analyzer and the less diffusive signal broadening can occur (for more details see Fig. S1 of the ESI†).

Dispersion efficiency. The fraction of particles that is effectively reaching the detector for both charging techniques it is

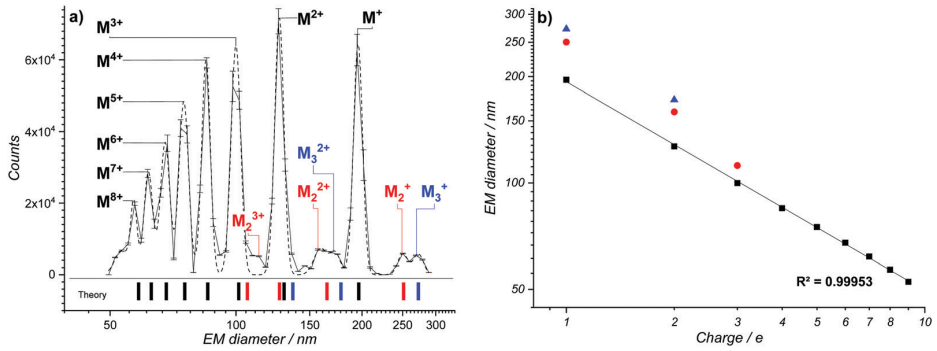

Fig. 3 Panel (a) highest concentration measured in the negative HV mode (cations) with the calculated EM diameters of differently charged particles, based on the singly charged monomer at an EM of 194 nm, monomers (black), dimers (red) and trimers (blue). Mulitply charged species of the monomers which are uniformly spaced on the logscale. The dashed line represent the cumulative lognormal fit curve. Panel (b) measured correlation between EM diameter and charge number of the monomers (black squares), dimers (red circles) and trimers (blue triangles). It shows a strong relation between the different monomeric charge states. This indicates that all these peaks result from the same species. The few dimer and trimer data points are only shown for comparison.

important to determine the absolute number of particles in the gas phase. By using a fully calibrated X-ray source, this number was found to be 20–30% for both techniques. For this X-ray source, it is known how many particles acquire how many charges, and what fraction remains neutrally charged. With this information, the absolute number of particles can be calculated. The X-ray source was coupled to the nES or IR-MALDI source for this experiment and the absolute number of charged particles was derived. This number, however, must not be confused with the charging efficiency of nES or IR-MALDI. Both charging sources impose their individual charge distributions on the generated droplet populations, including charged droplets and neutrally charged droplets. These are transported by a gas stream into the neutralizer that overrides the charge distribution with its own charge distribution. This, on average, means that higher charged particles get partially neutralized to lower charge states and neutral particles get charged to be mostly singly charged, both effects resulting in the characteristic charge distribution of the X-ray source. After that, the particles get measured by the DM analyzer. The number of detected particles thus mainly depends on the amount of sample that was dispersed at the source, and on the path of the gas stream. Since the latter is well characterized, the absolute number of particles in the gas phase can be determined. Hence, this efficiency is a dispersion and transfer efficiency and not solely an ionization efficiency, because losses in signal may not only be caused by insufficient charging but also by aerodynamic losses. Within our measurements, this dispersion efficiency did not change significantly with either of the ion sources.

Primary droplet size distribution. The primary droplet size distribution (PDSD) refers to the instance at which the sub-volume has completely separated from the bulk liquid for the first time. The droplets created by the IR-MALDI process do not contain enough charges to accumulate on the surface and to undergo the Coulomb fission cascade found in ES. Consequently, solvent evaporation and not further dispersion is the only mechanism by which the droplet shrinks. The particles remain as a residue with a net charge. Given the bipolar nature of the IR-MALDI source, all charges that have not annihilated each other during the shrinkage of the primary droplet are eventually transferred to the residual analyte as a net charge. Because this process lacks the Coulomb fission cascade, virtually all analyte mass from the initial primary droplet will be found in the final residue. This and the fact that this technique generates a broad size distribution of residuals, both can be used to determine the PDSD directly. Saccharose, a non-volatile and non-hygroscopic compound, was used for that determination. Since all the saccharose from the primary droplet will make up the final dried cluster residue, the initial volume, and thus diameter, of the primary droplet size can be calculated from the known saccharose concentration of the sample. It was possible to observe a PDSD centered on 300 nm at its largest using ES. When using ES, this PDSD results from balanced hydrostatic and electrostatic forces at the tip of the emitter. These forces in turn depend on the conductive properties of the analyte solution. Thus, when using ES, a change in solvent composition is often required in order change or adjust the PDSD. Even with a PDSD centered around 0.3 μm, as determined from saccharose cluster measurements, it was in practice virtually impossible to generate a stable spray for sMP larger than 155 nm. For IR-MALDI, this is not the case. IR-MALDI delivers a broader PDSD as shown in Fig. 4. Since IR-MALDI produces larger primary droplets on average, it is much easier to measure sMP larger than 100 nm. For this measurement, a saccharose solution of 50–5000 ppm dissolved in a 20 mM ammonium acetate solution was used. The PDSD for nES was centered around 0.29 μm. For IR-MALDI, it was centered on 0.33 μm and 0.37 μm for single pulse energies of 1.5 mJ and 3.2 mJ respectively, as shown in Fig. 4. This means that although the respective centers of the nES and IR-MALDI PDSD are similar, the increased width of the IR-MALDI-generated PDSD enables the probing of larger sMP.

To illustrate this, the saccharose method was refined and used to determine the primary diameter of particle containing

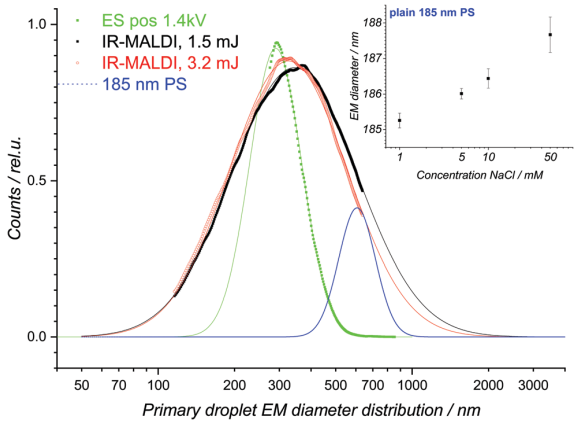

Fig. 4 Primary droplet size distribution, determined by saccharose from nES with 1.4 kV (green) in 20 mM ammonium acetate and IR-MALDI with 1.5 mJ (black) and 3.2 mJ (red) pulse energy in positive mode. The calculated blue curve estimates the range of singly charged primary droplets that are occupied when a plain 185 nm PS suspension is sprayed.

droplets. The 185 nm PS particles were suspended in water with different NaCl concentrations. As can be seen in Fig. 4, with an increase in NaCl concentration, the measured EM diameter increases as well. Analogous to the saccharide method, the solid residue formed as a coating on the particle can be converted to an amount of NaCl present in the primary droplet. This in turn can be used to calculate the initial volume of the droplet using the NaCl concentration. Thus, the measured differences in the EM diameters were used to calculate the total solvent volume and thus the primary droplet diameter. In the investigated case, the primary droplets were 0.68 ± 0.12 μm in diameter, including the solvent and the particle. A normalized lognormal distributed PDSD with its center at 0.68 μm and a width of 0.12 μm was calculated and is depicted as a blue in curve in Fig. 4.

3.3. IR-MALDI

Size range. As mentioned above, one main advantage of IR-MALDI is the potential to measure much larger particles than ES can. As shown in Fig. 5, particles ranging from 51 nm to 550 nm in EM diameter were measured. The particles were investigated under four different aspects: the polarity mode of the measurement, *i.e.* positive *vs.* negative charge, (Fig. 5a *vs.* 5b, sample identical), size (Fig. 5a–d), core material (Fig. 5a *vs.* 5c) and surface modification (Fig. 5c *vs.* 5d and Fig. S2 of the ESI†). We found this to be the first systematic investigation of the charge state distribution using IR-MALDI. The peak widths are first and foremost limited by the polydispersity of the particles and not by the DM analyzer. This proposition was tested and confirmed by using different sheath gas flow settings as mentioned earlier, having a sheath gas to aerosol gas ratio of 10 or higher for all measurements.

A comparison between Fig. 5a and b shows the influence of the two polarity modes the particles can be measured in. The M^{2-}/M^{-} ratio in the positive high voltage (HV) mode (negative charges) is slightly higher than the M^{2+}/M^{+} ratio in the negative HV mode (positive charges), with average values of 0.95 ± 0.20 and 0.70 ± 0.15, respectively. This trend is consistent over all measurements across the different size regimes. This finding can arise from the tendency of PS to inherently accumulate negative surface charges.[33] Aside from that, the spectra are largely identical for both polarities.

Fig. 5a and c show the comparison of the spectra of sMP with different core materials: plain PS (a) and plain silica (c). Both were measured in positive mode (negative charges) and with unmodified particle surfaces. A first observation is that the silica particles show fewer distinguishable charge states in the spectra. Secondly, their size distribution, deduced from the width of the singly charged monomer features in the spectra, was broader across the investigated size ranges. Because of this, the spectral region of the triple and higher charge states is more congested, especially in the case of the 290 nm or 310 nm and 400 nm particles. Since the peak center follows a rigid inherent pattern with increasing charge numbers, this congestion can be corrected for.

Fig. 5c and d are an example for the influence of a surface modification, as plain and amino alkyl linker modified silica particles, annotated as NH_2, which were compared to one another. The modified particles tend to produce more dimers compared to the unmodified particles. Since the particle number concentration is the same in both cases, this difference is unlikely to arise from a purely statistical particle distribution upon primary droplet formation. This means that the particles likely formed these clusters already in the bulk suspension. This theory was confirmed by measuring the sample before and after sonication. In both cases the spectra looked the same. This experiment allowed us to qualitatively assign a stronger tendency of the NH_2 modified particles to spontaneously form clusters than the plain particles.

In summary, the IR-MALDI-DM analyzer provided a much more accurate particle size distribution than the vendor-provided DLS data did. It disentangled multimodal particle size and cluster distributions.

Dynamic range. The dynamic range of IR-MALDI was tested with 194 nm plain PS particles in a mass concentration range from 0.25 to 25 000 μg mL^{-1}, which corresponds to 5.8×10^{8} and 5.8×10^{12} particles per milliliter solvent, as seen in Fig. 6. The double logarithmic linear trend shows that the system has not yet reached saturation. The limit of detection (LoD) and limit of quantification (LoQ) were approximated to be at a concentration of 0.7–1.1 ppm (w/w) and 3–3.6 ppm (w/w), respectively. Both values are larger than the expected LoD for DLS in that size regime.‡ Probing cations yields 36% and 17% lower LoD and LoQ than probing anions (see Fig. 6).

Despite the high mass concentration of 25 000 μg mL^{-1}, no clogging issues arose during the measurements. This illustrates one of the main advantages of the stainless-steel capillary configuration used in this IR-MALDI setup. Given the dynamic range that spans five orders of magnitude, it was possible to characterize the particles and their charge states even further.

‡ DLS sensitivity is usually referenced to lysozyme (6 nm in diameter) with 100 ppm. Applying DLS scaling laws, the limit of detection should therefore be orders of magnitude lower than that for a 100 nm particle.

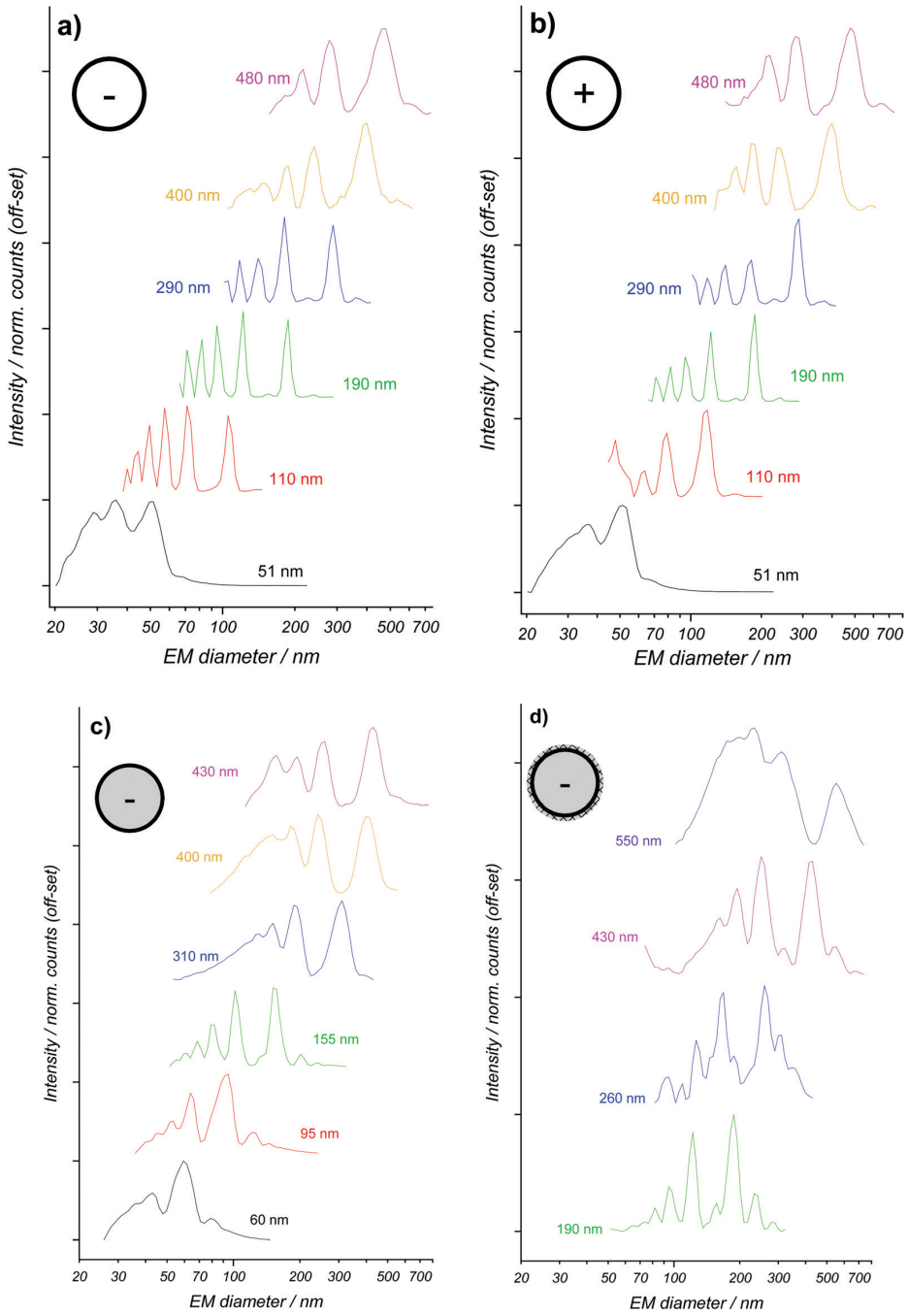

Fig. 5 EM spectra of monomodal samples, each line is one single monomodal particle population, charge-separated into their individual monomobile fractions, visible as peaks. Each sample is a 5 mg mL^{-1} suspension of sMP in water across different sizes, core materials and surface modification charged by IR-MALDI and measured with the long DMA (TSI 3081). Panel (a) positive HV mode, plain PS particles; panel (b) negative HV mode, plain PS particles; panel (c) positive HV mode, plain silicate particles; panel (d) positive HV mode, NH_2-modified silicate particles.

Over three orders of magnitude, from 2.5–25 000 μg mL^{-1}, the IR-MALDI-DM analyzer delivered sharp, defined features for the first five charge states of the particles. The signal integral *versus* concentration trend line has not completely plateaued within the investigated mass concentration range, indicating that not all charged droplets generated by IR-MALDI were

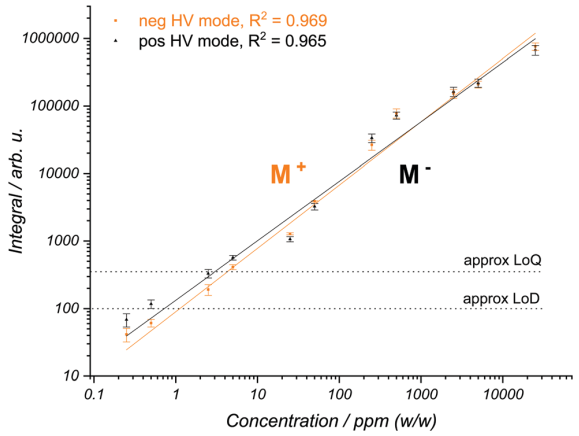

Fig. 6 Signal integrals of plain 194 nm PS particles charged by IR-MALDI *versus* EM diameters classified in the negative and positive HV modes (positively and negatively charged, respectively) in mass concentration from 0.25–25 000 µg mL^{-1} for the singly charged monomers. Based on the positively charged particles, the LoD and the LoQ are 0.15 (Integral = 100) and 2.5 (Integral = 350) particles per cubic centimeter of air, respectively.

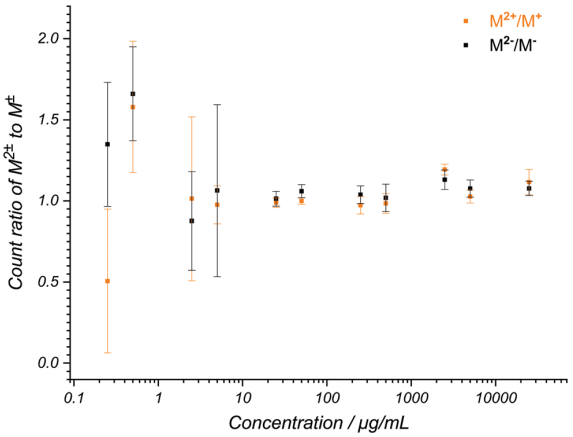

Fig. 7 The ratio of the signal integrals of the doubly to singly charged monomers of plain 155 nm polystyrene particles charged by IR-MALDI *versus* analyte in the positive (black, neg. charged) and negative (orange, pos. charged) HV mode for mass concentrations from 0.25–25 000 µg mL^{-1}. The ratio is 1.03 ± 0.08 for mass concentrations of 2.5 µg mL^{-1} or higher, for both polarities with no significant difference between positive and negative HV mode.

occupied by at least one particle. This finding suggests that the technique can handle samples with even higher particle concentrations, which is in line with results found in the literature, where no saturation for this concentration range was found either.[11,15] For a concentration of 25 000 µg mL^{-1}, up to eight charge states of the monomeric species were clearly visible in the spectrum. This allowed an unambiguous charge distribution characterization of the particles and the IR-MALDI source.

Fig. 7 shows the ratio of doubly-to-singly charged monomeric species was found to be independent of the concentration. This means that even at the highest concentrations, there were enough charges present in a droplet to provide multiple charges to all particles and particle clusters. This observation confirms that the charging capacity of the IR-MALDI source is not exhausted in this concentration range, as mentioned earlier. The data also shows that there is a constant relative fraction of (103 ± 8)% of doubly charged dimer M_2^{2+} in relation to the singly charged monomer M^+. This ratio stabilizes above 2.5 µg mL^{-1} or 2.5 ppm (w/w) and thus acts as another parameter confirming that above this concentration the signal emerges clearly and consistently.

The next investigated property is the ratio of singly charged dimers to singly charged monomers, as shown in Fig. 8. Dimers started to appear at a particle mass concentration of 250 µg mL^{-1}. Although dimers and trimers were detected, only the dimeric species could be quantified with sufficient precision. Fig. 8 shows the counts of monomers (black), dimers (red) and the dimer-to-monomer ratio (blue) *versus* the concentration. Both trendlines follow very similar slopes. The ratio between dimers and monomers is thus almost constant. In fact, the trendline indicates a 0.23 increase in relative dimer concentration per decade in concentration increase. Therefore, the tendency of the particles to form dimers upon a concentration increase is very low. This observation indicates that most of the sub-volumes created by the IR-MALDI

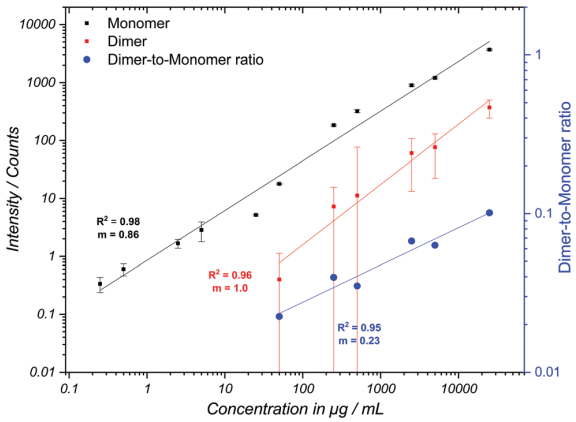

Fig. 8 The left scale shows the signal integrals of plain 194 nm polystyrene particles charged by IR-MALDI classified in the negative HV mode (positively charged) in a mass concentration range of 0.25–25 000 µg mL^{-1} for the singly charged monomers and dimers. The right scale shows the ratio of the singly charged dimers with respect to the singly charged monomers.

dispersion are empty or eventually become neutrally charged after charge annihilation. Consequently, by increasing the particle concentration, these empty sub-volumes are filled with particles instead of filled sub-volumes accumulating two or more particles to and forming charged dimers or larger oligomers. This is yet another indicator confirming that the investigated concentration range is not close to the saturation of the charging capabilities of IR-MALDI.

Another indication that the charging capacity of the source was not reached was obtained when the IR-MALDI source was coupled to a commercially available soft X-ray source, which

generates a known charge distribution and thus known particle number concentration in the gas phase.

An aerosol neutralizer was used to confirm the monomobile population to be monomodally distributed. In this instrument, the soft X-radiation source confines the charge population of the aerosol created by IR-MALDI. This means that higher charged particles get partially neutralized to lower charge states and neutral particles get charged, resulting in mostly singly charged particles. By doing so potentially congested monomobile signals can be divided into their respective monomodal parts. The result is shown in Fig. 9, where the black, upper curve represents the IR-MALDI measurement and the red, lower curve represents a measurement with the aerosol neutralizer switched on. In the case where the aerosol neutralizer is switched on, no other signal than the assigned one is left in the EM diameter range from 30 nm to 180 nm. Thus, no other species lays underneath the congested area between 30 nm and 100 nm in EM diameter. The data shows that the X-rays neutralize particles more particles than it charges. The total area is decreased for unnormalized ordinates (data not shown).

By switching on the soft X-ray source, the highest charged species in the 40–80 nm EM diameter range are decharged to lower charge states and are thus shifted to larger EM diameters, which can be seen in Fig. 9. The lower red graph in Fig. 9 shows that about 90% of all charges are contained in droplets below 40 nm in EM diameter, which means that they cannot contain a particle in the investigated size range (see S3 of the ESI†), and thus the system's particle charging capacity must be far from being exhausted. The upper black graph in Fig. 9 shows a similar trend. When the X-ray source was switched off, IR-MALDI generated an aerosol with about 50% of all charges contained in unoccupied droplets (see S3 of the ESI† for more details). From the spectrum with X-ray switched on, it is possible to obtain the absolute number of droplets and particles in the gas phase. The lower, red spectrum in Fig. 9 is already corrected for multiple charges and diffusion losses. This means it shows the absolute number of occupied droplets (>40 nm) and unoccupied droplets (<40 nm) per cubic centimeter of carrier gas. The initial particle concentration in the gas phase c_g can be computed with eqn (1), since the sample flow rate Q_s, the particle number concentration in the liquid sample c_s and the gas flow rates Q_g are known for that measurement.

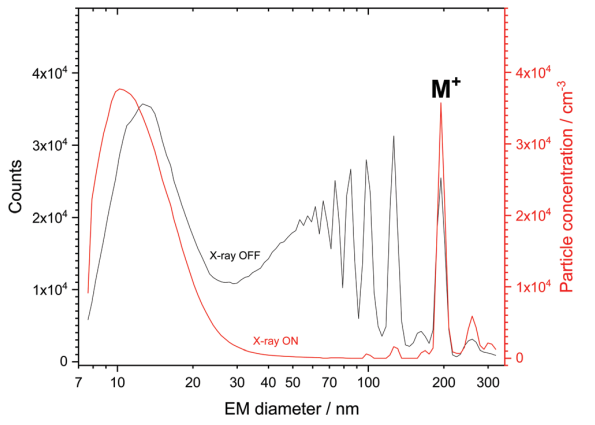

Fig. 9 Comparison of the charge distribution generated IR-MALDI (X-ray OFF) and soft X-ray (X-ray ON) source. After a multiple charge correction and diffusion loss correction, the initial spectrum (black) is decongested (red) and the population can be directly quantified. This quantification shows that about 30% of the initial sample gets detected in the end. Note that both ordinates depict different units and cannot be compared in absolute terms, only in the relative peak intensities within the spectrum.

$$c_g = \frac{c_s \cdot Q_s}{Q_g} \quad (1)$$

An initial, maximum concentration of 4.3×10^5 particles per cm^3 of gas was calculated. The total amount of detected particles, *i.e.* the total integral of the lower, red curve in Fig. 9 from 40–310 nm, was 1.3×10^5 particles per cm^3. This number corresponds to about 30% of the initial 4.3×10^5 particles per cm^3 and thus roughly 30% of the particles fed into the system were eventually detected. It is important to note that these losses are not only due to the ionization efficiency but are also results of impacts in the ionization chamber or further unspecified diffusion losses due to the geometry of the ionization chamber.

Charge distributions. Another important aspect of the characterization of the IR-MALDI process is the charge distribution it generates. In the presented work, the charge evolution is considered to take place in two different stages which were described in the literature.[11,34] One stage is the charge annihilation within a single droplet (in the liquid phase). Upon creation, a single droplet contains multiple charges of both polarities that may statistically annihilate over time by entering each other's Debye volume, eventually creating the net charge of the droplet or particle. This is reported in the literature to follow a Poisson-like process, see eqn (2)–(4).[11,12,35] Another stage is the charging or annihilation of charges due to droplets merging in the gas phase. Since IR-MALDI generates a mist of charged droplets, the latter may combine and thus annihilate charges. If this gas phase charge annihilation were the dominant cause of the final charge distribution, a bipolar gas model, such as the Wiedensohler charge distribution, could be used to describe the charge distribution.[34]

First, the Poisson-based charge distribution model was used to fit the data from plain silicate and PS particles of different sizes. The spectra of the positive and negative charges were combined to create a single charge distribution for each particle size and species. It was assumed that most of the droplets generated by IR-MALDI do not contain a net charge or a particle. The general form of a Poisson distribution P with k events, and an expected value of λ,

$$P_\lambda(k) = \frac{\lambda^k}{k!} e^{-\lambda} \quad (2)$$

was adjusted and yielded the following fit function.

$$P(q) \propto \exp\left[\frac{-q^2}{4N}\right] \cdot \left[1 + erf\left(\frac{2N - q}{2\sqrt{N}}\right)\right] \quad (3)$$

For a detailed description and justification of this model function, please refer to the work of Wiederschein *et al.*[11]

Briefly, the total sample volume that is dispersed upon IR-MALDI is divided into many sub-volumes, called droplets. Each droplet contains a randomly distributed number N of positive and negative charges. All charges combined make up the net charge q of the droplet. Both q and N are dimensionless variables representing the initial charge N and final charge q of a droplet, before and after the charge annihilation process, respectively. Thus, q is the charge state that will be detected.

In summary, the error function eqn (3) from literature tilts the Gaussian charge distribution, *i.e.* a Poisson distribution for a large expected value λ, towards net surplus of positive charges. This one-sided tilt, however, was not reflected in the data that was obtained in this work, because the maxima of the different charge distributions were found to fluctuate between a positive and a negative charge. To empirically correct for that shift, the charge off-set q_0 was introduced. This adjusts the distribution so that the fit can be used independent of polarity dominance.

$$P(q) \propto \exp\left[\frac{-(q-q_0)^2}{4N}\right] \cdot \left[1 + \mathrm{erf}\left(\frac{2N-(q-q_0)}{2\cdot\sqrt{N}}\right)\right] \qquad (4)$$

Fig. 10 shows the experimental data (empty circles) for particles from 110 nm to 487 nm. The peaks for the different particle sizes show only minor eccentricities or changes in widths. This finding suggests that there is only a minor contribution the particle size has on the charge distribution. The Wiedensohler charge distribution data and the fit according to eqn (4) was added to Fig. 10 in order to compare the fit performance.[34] It becomes apparent that especially for the smaller particles, the Wiedensohler distribution and the experimental data differ significantly from one another. The fit based on eqn (4) has a much smaller error for all measured cases. However, since the Poisson distribution (eqn (3)) was adjusted (eqn (4)), the fit function lost its Poisson character by decoupling the mean and the variance from one another. This fact emphasizes the Gaussian character of the underlying mechanism. It is not clear in which of the two charge evolution stages this Gaussian charge mechanism is rooted, or, if present in both, where it is most pronounced. This remains an open question that needs to be addressed in the future to solve the IR-MALDI charge evolution problem.

4. Conclusion

In the presented work, IR-MALDI was successfully implemented into a DM analyzer as a dispersion and charging source for sMP suspended in solution. The technique was able to disperse and charge particles of different sizes and constitutions from a water suspension in positive and negative polarity without any additives. The developed IR-MALDI setup delivered a much better resolving power than dynamic light scattering, the standard for determining the sizes of sMP in this size range. It was possible to disperse and charge particles up to 550 nm in EM diameter, a size regime not accessible for conventional ES. The technique therefore effectively bridges the gap between ES-DM analysis and DLS by providing good resolving power for sMP. The particles could be characterized by investigating the effects of cluster formation and surface modification. Additionally, physicochemical insights into the IR-MALDI process could be gained. The first systematic study on the charge distribution that IR-MALDI produces across several particle diameters and surface modifications could be provided. The Wiedensohler

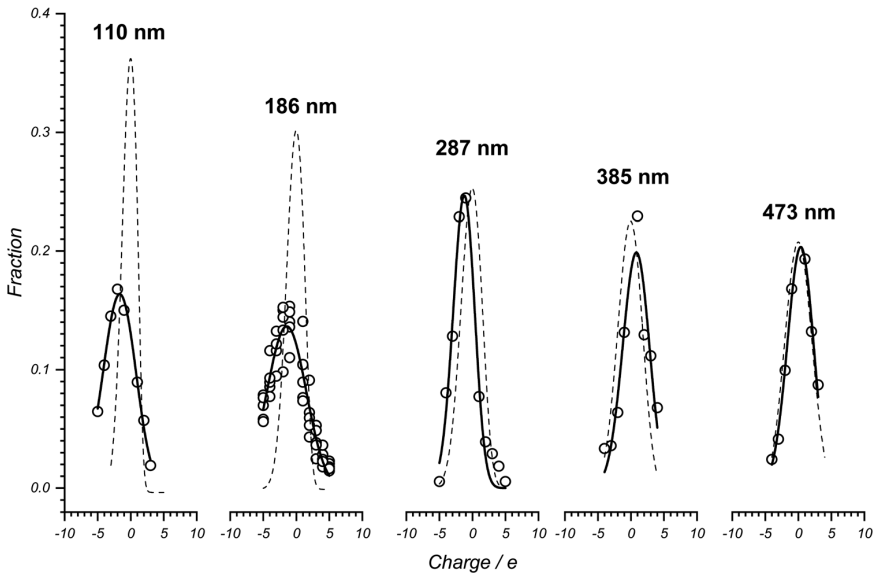

Fig. 10 Area-normalized charge distribution spectra of plain polystyrene particles charged by IR-MALDI across five particle diameters. The data points (empty circles) were fitted using the adjusted Poisson model (bold line) described earlier and compared to the Wiedensohler model (dashed line) at that EM diameter.

charge distribution of soft X-ray and radioactive radiation-sustained bipolar gases and a Poisson-derived charge distribution were used to explain the experimental results of this work. However, the obtained data deviated from both charge distribution models. The Poisson-derived distribution was adjusted to the experimental data. Using this new fit model, it was observed that the Wiedensohler data set and experimental data from the IR-MALDI source show some convergence for particles in the EM diameter range larger than 300 nm, while there are severe differences for EM diameters smaller than that. The fit that explains the experimental data best suggests Gaussian behavior, *i.e.* the mean and variance are independent from one another. The question remains open whether that behavior is due to a severe distortion of the original Poisson charging or if there is a separate mechanism occurring subsequent to the Poisson charging.

Author contributions

C. P. contributed by conceptualization, data curation, investigation, validation, formal analysis, methodology, visualization and writing of the manuscript at all stages. J. V. developed, designed, and helped manufacture the ionization chamber and the IR-MALDI setup as well as reviewing and editing the presented work. M. Z. contributed by conceptualization and investigation. T. B. contributed by conceptualization, data curation, supervision, and writing at all stages of the publication. H.-G. L. contributed by supervision, continuous discussion and interpretation of results, funding acquisition, project administration, writing review and evaluation of the presented work.

Conflicts of interest

The authors declare that they have no conflict of interest.

Acknowledgements

This work was funded as part of the research group (FOR 2177, project number: 275653032) and the School of Analytical Sciences Adlershof (SALSA, Berlin, Germany) by the Deutsche Forschungsgemeinschaft (DFG, German Research Foundation). This paper was co-financed by the European Regional Development Fund (ERDF) and the State of Brandenburg.

Notes and references

1 F. Hillenkamp, M. Karas, R. C. Beavis and B. T. Chait, Matrix-Assisted Laser Desorption/Ionization Mass Spectrometry of Biopolymers, *Anal. Chem.*, 1991, **63**, 1193A–1203A.

2 M. Karas and F. Hillenkamp, Laser desorption ionization of proteins with molecular masses exceeding 10,000 daltons, *Anal. Chem.*, 1988, **60**, 2299–2301.

3 A. Overberg, M. Karas, U. Bahr, R. Kaufmann and F. Hillenkamp, Matrix-assisted infrared-laser (2.94 μm) desorption/ionization mass spectrometry of large biomolecules, *Rapid Commun. Mass Spectrom.*, 1990, **4**, 293–296.

4 J. Soltwisch, H. Kettling, S. Vens-Cappell, M. Wiegelmann, J. Muthing and K. Dreisewerd, Mass spectrometry imaging with laser-induced postionization, *Science*, 2015, **348**, 211–215.

5 T. Bien, S. Bessler, K. Dreisewerd and J. Soltwisch, Transmission-Mode MALDI Mass Spectrometry Imaging of Single Cells: Optimizing Sample Preparation Protocols, *Anal. Chem.*, 2021, **93**, 4513–4520.

6 R. Hiraguchi, H. Hazama, K. Masuda and K. Awazu, Atmospheric pressure laser desorption/ionization using a 6-7 μm-band mid-infrared tunable laser and liquid water matrix, *J. Mass Spectrom.*, 2015, **50**, 65–70.

7 D. M. Wieliczka, S. Weng and M. R. Querry, Wedge shaped cell for highly absorbent liquids: infrared optical constants of water, *Appl. Opt.*, 1989, **28**, 1714.

8 A. Vogel and V. Venugopalan, *Chem. Rev.*, 2003, 103.

9 A. Vogel, I. Apitz and V. Venugopalan, *Oscillations, Waves and Interactions*, 2007.

10 A. Miotello and R. Kelly, Laser-induced phase explosion: new physical problems when a condensed phase approaches the thermodynamic critical temperature, *Appl. Phys. A: Mater. Sci. Process.*, 1999, **69**, S67–S73.

11 F. Wiederschein, E. Vöhringer-Martinez, A. Beinsen, F. Postberg, J. Schmidt, R. Srama, F. Stolz, H. Grubmüller and B. Abel, Charge separation and isolation in strong water droplet impacts, *Phys. Chem. Chem. Phys.*, 2015, **17**, 6858–6864.

12 A. Charvat and B. Abel, How to make big molecules fly out of liquid water: applications, features and physics of laser assisted liquid phase dispersion mass spectrometry, *Phys. Chem. Chem. Phys.*, 2007, **9**, 3335.

13 A. Charvat, E. Lugovoj, M. Faubel and B. Abel, New design for a time-of-flight mass spectrometer with a liquid beam laser desorption ion source for the analysis of biomolecules, *Rev. Sci. Instrum.*, 2004, **75**, 1209–1218.

14 W. Kleinekofort, J. Avdiev and B. Brutschy, A new method of laser desorption mass spectrometry for the study of biological macromolecules, *Int. J. Mass Spectrom. Ion Processes*, 1996, **152**, 135–142.

15 J. Villatoro, M. Zühlke, D. Riebe, J. Riedel, T. Beitz and H. G. Löhmannsröben, IR-MALDI ion mobility spectrometry, *Anal. Bioanal. Chem.*, 2016, **408**, 6259–6268.

16 J. Villatoro, M. Zühlke, D. Riebe, T. Beitz, M. Weber, J. Riedel and H.-G. Löhmannsröben, IR-MALDI ion mobility spectrometry: physical source characterization and application as HPLC detector, *Int. J. Ion Mobility Spectrom.*, 2016, **19**, 197–207.

17 A. Takamizawa, S. Kajimoto, J. Hobley, K. Hatanaka, K. Ohta and H. Fukumura, Explosive boiling of water after pulsed IR laser heating, *Phys. Chem. Chem. Phys.*, 2003, **5**, 888–895.

18 I. Apitz and A. Vogel, Material ejection in nanosecond Er:YAG laser ablation of water, liver, and skin, *Appl. Phys. A: Mater. Sci. Process.*, 2005, **81**, 329–338.

19 C. Urey, V. U. Weiss, A. Gondikas, F. von der Kammer, T. Hofmann, M. Marchetti-Deschmann, G. Allmaier, G. Marko-Varga and R. Andersson, Combining gas-phase electrophoretic mobility molecular analysis (GEMMA), light scattering, field flow fractionation and cryo electron microscopy in a multidimensional approach to characterize liposomal carrier vesicles, *Int. J. Pharm.*, 2016, **513**, 309–318.

20 V. U. Weiss, R. Pogan, S. Zoratto, K. M. Bond, P. Boulanger, M. F. Jarrold, N. Lyktey, D. Pahl, N. Puffler, M. Schelhaas, E. Selivanovitch, C. Uetrecht and G. Allmaier, Virus-like particle size and molecular weight/mass determination applying gas-phase electrophoresis (native nES GEMMA), *Anal. Bioanal. Chem.*, 2019, **411**, 5951–5962.

21 J. Fernández de la Mora, The Fluid Dynamics of Taylor Cones, *Annu. Rev. Fluid Mech.*, 2007, **39**, 217–243.

22 N. Shirai, Y. Onaka, S. Ibuka and S. Ishii, Formation of Ethanol Filament and Its Pulsed Discharge for Microplasma Generation, *Jpn. J. Appl. Phys.*, 2008, **47**, 2244–2249.

23 P. Nemes, I. Marginean and A. Vertes, Spraying Mode Effect on Droplet Formation and Ion Chemistry in Electrosprays, *Anal. Chem.*, 2007, **79**, 3105–3116.

24 P. Kebarle and U. H. Verkerk, Electrospray: From ions in solution to ions in the gas phase, what we know now, *Mass Spectrom. Rev.*, 2009, **28**, 898–917.

25 T. Musapelo and K. K. Murray, Particle Formation in Ambient MALDI Plumes, *Anal. Chem.*, 2011, **83**, 6601–6608.

26 F. Cao, F. Donnarumma and K. K. Murray, Particle size measurement from infrared laser ablation of tissue, *Analyst*, 2016, **141**, 183–190.

27 J. Fernandez de la Mora and C. Barrios-Collado, A bipolar electrospray source of singly charged salt clusters of precisely controlled composition, *Aerosol Sci. Technol.*, 2017, **51**, 778–786.

28 R. Gunn and R. H. Woessner, Measurements of the systematic electrification of aerosols, *J. Colloid Sci.*, 1956, **11**, 254–259.

29 R. Gunn, Diffusion charging of atmospheric droplets by ions, and the resulting combination coefficients, *J. Meteorol.*, 1954, **11**, 339–347.

30 T. J. Johnson, R. T. Nishida, M. Irwin, J. P. R. Symonds, J. S. Olfert and A. M. Boies, Measuring the bipolar charge distribution of nanoparticles: Review of methodologies and development using the Aerodynamic Aerosol Classifier, *J. Aerosol Sci.*, 2020, **143**, 105526.

31 S. Guha, J. R. Wayment, M. Li, M. J. Tarlov and M. R. Zachariah, Characterizing the adsorption of proteins on glass capillary surfaces using electrospray-differential mobility analysis, *Langmuir*, 2011, **27**, 13008–13014.

32 S. Guha, J. R. Wayment, M. Li, M. J. Tarlov and M. R. Zachariah, Protein adsorption-desorption on electrospray capillary walls - No influence on aggregate distribution, *J. Colloid Interface Sci.*, 2012, **377**, 476–484.

33 S. Lu, K. Zhu, W. Song, G. Song, D. Chen, T. Hayat, N. S. Alharbi, C. Chen and Y. Sun, Impact of water chemistry on surface charge and aggregation of polystyrene microspheres suspensions, *Sci. Total Environ.*, 2018, **630**, 951–959.

34 A. Wiedensohler, An approximation of the bipolar charge distribution for particles in the submicron size range, *J. Aerosol Sci.*, 1988, **19**, 387–389.

35 A. Charvat, A. Bögehold and B. Abel, Time-Resolved Micro Liquid Desorption Mass Spectrometry: Mechanism, Features, and Kinetic Applications, *Aust. J. Chem.*, 2006, **59**, 81.

3.3 Counting, sizing, and identifying metal-bearing aerosols in-flight using laser-induced breakdown spectroscopy (LIBS), laser-induced incandescence (LII), and optical imaging

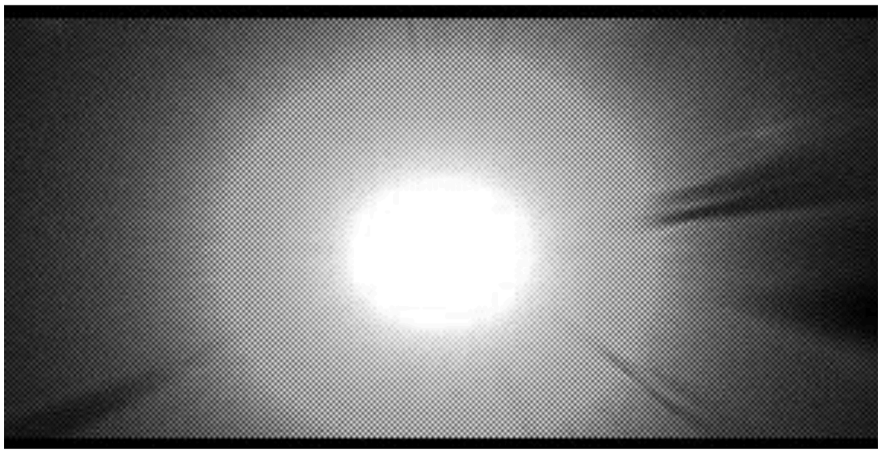

Figure 3.3: In-flight capture of a laser-induced plasma event at the surface of an aluminum oxide particle of 100 µm diameter

Scope of the publication Continuing the work with infrared light, this study aimed for the implementation of laser-based analytical techniques in industrial process monitoring. Phase-selective LIBS was used at low fluences and high repetition rates for the data acquisition required for near real-time measurements. Combined with shadowgraphy, light scattering, photodiode and photoacoustic detection, this work presents a comprehensive set of in-line process analytics complementing one another. A new photoacoustics normalization procedure was developed for the in-line application in industrial environments. LII was used for particle counting, however, has quickly proven to hold great analytical value as an aerosol classification technique. The work presented is one the few cases exploring that avenue, and the first to suggest fluence screening procedures to harvest near real-time aerosol compounding information.

Author's contribution My contribution to this study was the design and realization of the closed-batch dust circuit. A significant portion of my work was the systematic implementation and synchronization of the techniques shown. I coded the data evaluation procedure for each technique separately using the Matlab environment and eventually unified them. Being the main editor of this manuscript, my responsibilities included, but were not limited to, writing, editing and data visualization.

Counting, sizing, and identifying metal-bearing aerosols in-flight using laser-induced breakdown spectroscopy (LIBS), laser-induced incandescence (LII), and optical imaging.

C. Prüfert, T. Beitz, O. Reich, H.-G. Löhmannsröben

Physical Chemistry, Institute of Chemistry, University of Potsdam, Potsdam, Germany

Abstract

The quantification and identification of aerosols in industry plays a key role in process monitoring and control and lays the foundation for process automation aspired by the industry 4.0 initiative. However, measuring particulate matter's mass and number concentrations in harsh environments poses great analytical constraints. The presented approach comprises a comprehensive set of light- and imaging-based techniques, all contactless, in-line, and real-time. It includes, but is not limited to, stroboscopic imaging, laser-induced breakdown spectroscopy (LIBS) and laser-induced incandescence (LII). Stroboscopic imaging confirmed the particles sphericity and was used to measure the particle number density. A phase-selective LIBS setup with low fluence and 500 Hz repetition rate was used to classify each particle with a single shot and in real time. Simultaneously, the created plasma was captured by CCD imaging to determine the detection volume and hit rate of the LIBS setup. Both data sets combined were converted to a particle number density, which was consistent with the particle number density of the stroboscopic measurements. Furthermore, using a photodiode and microphone in parallel to the LIBS setup allowed for the photoacoustic normalization of the spectral line intensity at the laser repetition rate of 500 Hz. This was done as a partial photoacoustic normalization method with the cut-off based on the coefficient of variation (CV), reducing it by 25%. Aside from that photodiode and microphone were proven to be valuable event counting with the advantage of the less spatially constricted. A second laser setup was used for laser-induced incandescence (LII) making it possible to classify the particles based on their incandescence susceptibility. Given its larger probing volume, LII could be employed at very low particle number densities. With respect to the current literature, this is the first approach of using LII as an in-line, real-time analytical technique for the compositional classification of metal-bearing aerosols.

1. Introduction

With the advent of industry 4.0 the creation of cyber-physical systems is on the horizon, wherein closed-loop data models automate and autonomously control processes.[1] Still in its infancy, the potential of industry 4.0 for the metal production sector is immense, which is especially true for copper pyrometallurgy, with its global annual production of more than 24 million metric tonnes of refined copper.[2] For the realization of this transformation a vast set of parameters at all stages of the production chain would be ideal. Currently, the control mechanisms are mostly based on mass and heat balances, and to a great extend the operator's experience. Aspects that are hard to implement into autonomous process control. In-line, only pyrometric flame temperature measurements are taken. This parameter ought to estimate the chemical route the feed takes during the combustion process. This parameter alone, however, is too limited to successfully pave the way for copper pyrometallurgy 4.0. The hostile conditions within the flash smelting furnace, the reaction shaft, the settler, and even the off-gas region make the introduction of in-line analytical techniques challenging. Nevertheless, more and more contactless optical sensors and spectroscopic techniques were explored for process monitoring and control in recent years.[3–5] The broader the captured parameter space, the better the prevention of formation of side products (primary measures) and the better successive pollutant removal parameters can be adjusted (secondary measures).

Stroboscopic imaging makes use of the stroboscopic effect which occurs when an imaging method captures a moving object or population using a bright, usually micro- or nanosecond short flash of light as back illumination. These particles, given their movement is insignificant compared to their own characteristic length, appear stalled (blur-reduced) enabling defined shape and size analysis. Object identification and measurements can be done using standard frame-by-frame processing open-source software such as ImageJ. Particle sizes and shapes can be obtained simultaneously and almost instantly with processing rates of up to 100 - 200 frames per second. It is used in high-speed applications such as medical imaging[6], physical process studies[7] and engineering disciplines involving, but not limited to, in-flight particle analyses. In-flight particle imaging is a subdomain of particle image velocimetry[8], and gives a very intuitive rendering of the shape and size of particle population, since all objects are imaged directly.

Laser-induced breakdown spectroscopy (LIBS) is a universally used technique when it comes to contactless, minimally invasive compositional analysis of materials.[9] Its applications are for example in tissue identification[10], plastics' classification[11], photovoltaic technology[12], and elemental monitoring in the metal making process.[13,14] LIBS was also part of both Mars rover missions, Curiosity and Perseverance[15,16], arguable the most profound evidence for its robustness and reliability. Recent developments in single-particle aerosol analysis have shown that LIBS is well suited for compositional analysis of particles.[17–20] However, most reported studies uniformly employ high-energy ns-pulses with at least 100 mJ and therefore low repetition rates below 10 Hz. Moreover, averaging of multiple LIBS signals is mostly used.

Synchronizing these single-shot LIBS spectra with a microphone, allows for the photoacoustic normalization of these spectra. This concept is rooted in plasma-based photoacoustic theory suggesting that the amount of ablated material during a LIBS event correlates with the amplitude of the emitted acoustic shockwave relates to the intensity which in turn.[21,22]

Laser-induced incandescence (LII) is considered the '*workhorse for in situ measurements of mature-soot particles in combustion and ambient atmospheric environments*'.[23] Given the large absorption cross-section of mature soot, also known as black carbon, it is very prone to incandescence, making it ideal for counting by LII.[24–26] Recently, more advanced dual-pulse LII was used to determine size

distribution and nano-structural elements.[27] Currently, a few real-time LII (ReTi-LII) studies also included metal and metal-oxide nanoparticles with significantly smaller absorption cross sections than mature-soot.[28–31] However, these are fundamental research interests aiming for particles' peak temperatures and thermal accommodation coefficients and modelling thereof. Practical applications for the aerosol characterization have yet to find its way into the process-analytics community.

The presented work aims to showcase a unique combination of instruments that can characterise size, composition, and mass concentration of the particulate matter at the end of the smelting process and in the off-gas. All selected instrumentation is generally suitable for in-line and real-time process analysis. Here, aluminium oxide and chalcopyrite, both industrially and commercially relevant minerals, were studied in terms of their susceptibility to LIBS, LII and photoacoustics. The usual LIBS setup that uses high fluences and low repetition rates was inverted by using pulse energies of 3 mJ or 10 mJ with repetition rates of 500 Hz and 100 Hz, respectively. This not only made this approach more cost-effective, but also, and most importantly, provides useful statistics in a matter of seconds. A feature that is essential given its eventual application as a process monitoring and near real-time feedback. For the synchronization of all techniques, a photodiode was used, given its short rise time of 1 ns and sampling rate of 100 kHz. It also provided a sensitive and highly robust way of counting all light-emitting events.

2. Setups and methods

Fig. 1 shows a scheme of the setup. It comprises of a closed-loop aerosol generator with an observation platform as the central analytical tool. The setup could produce mass concentrations of particles of 450 g/m³ using particles with a solid density of 4 000 kg/m³ and a bulk density of 1 000 kg/m³. A gas flow controller with an upper limit of 5 L/min effectively created laminar flow velocities (Re ≈ 1200) of up to 2.2 m/s and therefore terminal velocity corrected net velocity of the particles of 1 - 1.5 m/s upwards.

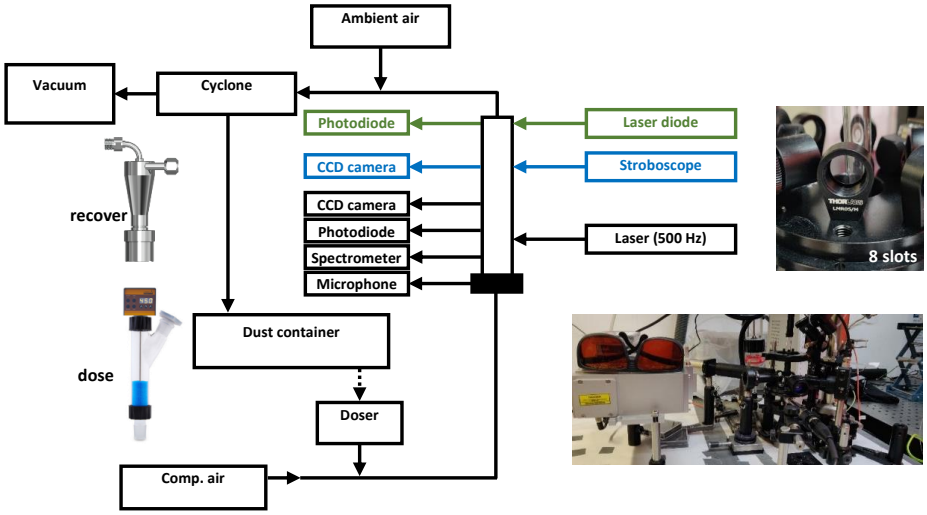

Fig. 1 Closed-loop aerosol generator. Two stock pictures provided by the vendor on the left show the cyclone and the doser. The two pictures on the right show the realised lab setup, indicating the 8 slots available for measurements.

2.1. Closed-loop aerosol generator. For the dust stream generation, a closed-loop system was developed. The particles were put in a volumetric powder doser (DOSER 0.2L, LAMBDA CZ, s.r.o., CZ). From here, the powder drops in a ¼" T-piece where it is picked up by a stream of compressed air controlled by an MFC (MFC 5850E series, Brooks Instruments GmbH, Dresden, DE), usually 5 L/min. The aerosol stream is guided via a ¼" conductive silicone tubing (TSI Inc., USA) into the bottom of vertically mounted quartz glass tube (I.D. = 8 mm, ProQuartz GmbH, Mainz, DE). Downstream from that a cyclone (Rohgas-Zyklon Staubabscheider, Paul Gothe GmbH, Bochum, DE) coupled to a vacuum (Kärcher T 10/1 ADV Hepa, Friedrich Niemann GmbH, Berlin, DE) and to a rotameter (Schwebekörper Durchflussmessgerät, Nieruf GmbH, Besigheim, DE) recovered the particles. The recovered particles were manually and thus batchwise fed back to doser, completing the closed-loop. The cyclone has a 97.5% recover efficiency for particles > 5 µm, which provides the lower limit of the investigated particle size.

2.2. Observation platform. A round 91 mm breadboard (RBBA 1/M, Thorlabs, Bergkirchen, DE) with a 25.4 mm bore was used to equi-planarily align the NIR Laser (NL204, Ekspla, Vilnius, LT or SP-DPSS Compact-100, InnoLas Laser GmbH, Krailling, DE), photodetector (DET10A, Thorlabs, Bergkirchen, DE) and multichannel spectrometer (2010789U, Avantes BV, Apeldoorn, NL), and CCD camera (NS4133BU, NET GmbH, Finninf, DE) around the quartz tube. All optical and photodetectors were equipped with a shortpass filter (FESH1000, Thorlabs, Bergkirchen, DE) to filter for the laser wavelength of 1064 nm. All light was collimated and focused using CaF_2 optics before it reached any detector.

2.3. Photodiode and photoacoustic detection. The photo- and microphone (photoacoustic) signals were probed with a sampling rate of 100 kHz, and both fed to the same USB oscilloscope (Handyscope HS3, TiePie engineering, Sneek, NL), ensuring synchronicity of both signals for recording events with a maximum repetition frequency of 500 Hz.

2.4. Light scattering. Light from a 516 ± 0.4 nm diode laser was transferred via a 0.6 mm optical fibre to a collimator and focussing lens before entering the in-house developed sheath gas T-piece (see **Error! Reference source not found.**) that brought the light into the tube. Opposite of the light entrance a sheath gas and light exhaust was installed. At an angle of 155° relative to the incident light, an optical fibre collected the scattered light and was connected to the detecting Si photodiode. The photodiode signal was digitized using a multifunction I/O device (USB-6216, National Instruments, Austin, USA) and recorded and controlled using an in-house programmed Labview GUI.

2.5. Plasma efficiency setup. A constant stream of particles fell out of a thin funnel and generated a column, 2.4 mm in diameter. As a starting position, laser focal point was set 5 mm in front of the particle stream. Using an x-stage mounted below the optical system, the focal point was brought closer to the particle stream with a step-size of 0.5 mm. Events were recorded using the photodiode.

2.6. Data treatment. All data processing was done with Matlab and Originlab was used for data visualisation. For all synchronization purposes, the photodiode was used as a master given its 100 kHz sampling rate and a rise time of 1 ns. For that, the median corrected photodiode signal trace was searched for peaks using matlab's built-in function *findpeaks* with a *MinPeakdistance* of 190 data points which corresponded to 1.9 ms for a 100 kHz sampling rate. The peak height threshold, *MinPeakHeight,* was set to a *median + 3σ*. Each event was assigned a peak maximum and a time stamp *t*. This time stamp *t* was used to find the corresponding signal in the acoustic signal trace, or others when applicable. Since the acoustic signal was delayed compared to the light flash, only a forward time interval of size *t* + 1.9 ms was used to look for the maximum of the microphone signal in that time interval. Each photodiode-detected event now has a time stamp, a maximum photodiode signal, and a maximum photoacoustic signal. The CCD camera data (video) was evaluated using ImageJ's "Analyse particles" function for frame-by-frame processing. Size and intensity thresholds of the grayscale virtual stacks were adjusted as needed.

2.7. Particle Preparation. The Al_2O_3 particles were purchased from Roth (X908.2, Carl Roth GmbH, Karlsruhe, DE). All other particles were purchased from Kremer (Kremer Pigmente GmbH & Co. KG, Aichstettenm DE). Particles were dry-sieved multiple times using a woven wire mesh sieve tower (0/32/40/50/63/90/125/250 µm) and 6 mm steatite sieving aids on every sieve.

3. Results

Four in-line, contactless, and real-time methods for the determination of the size, shape, number density and composition of industrial aerosols in process analytics were investigated. The particles' parameter space of number density and composition were approached by multiple, intersecting techniques. The size and shape information were mostly drawn from stroboscopic imaging. As can be seen on the right, the different techniques overlap in their information making the entire setup a robust starting for the determination of the four major properties size, shape, number density and composition.

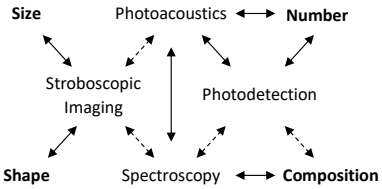

Fig. 2 Structure scheme showing the relation between measurement techniques and particle properties properties.

3.1. Light scattering

As one of the standards for particle concentration determination, light scattering was used to quantify the mass concentration of aerosol particles in the gas stream. Using a 516 ± 0.4 nm diode laser for the analysis of Al_2O_3 particles 32 - 125 µm in diameter led to a relative frequency of 200 - 700. The relative frequency x is the ratio of the particle circumference (2D projected) to the wavelength of the used light. It indicates how the scattering relates to the particle dimensions. In the case of Rayleigh scattering ($x << 1$) the scattering cross section relates to the particle dimension, $\sigma_S \sim d^6$, and for large particles ($x >> 1$) this scattering cross section relates to the particle dimension, $\sigma_S \sim d^2$ therefore also directly to the particle number density, assuming an equally-sized particle population and little light extinction. The light scattering signal is expected to follow the same proportionality with respect to the particle number density. The resulting scattering signals are shown in Fig. 3a for the shown case mass concentrations from 0 to about 500 grams of particles per cubic meter of carrier gas.

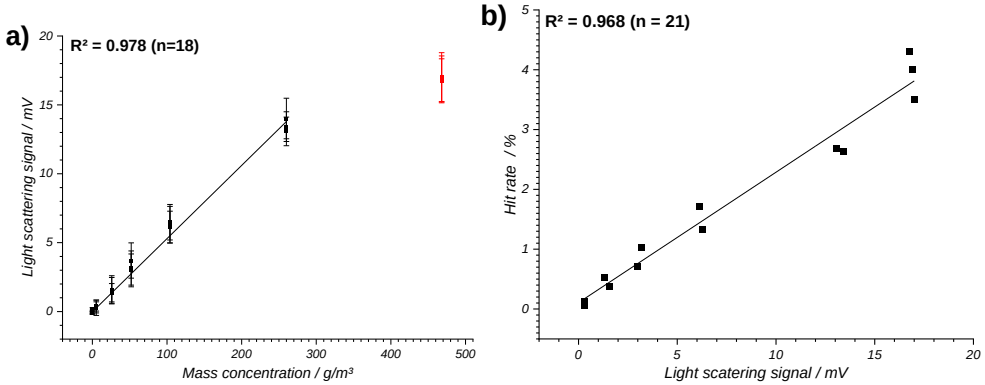

*Fig. 3 Light scattering data using a 516 nm laser for Al_2O_3 (90 - 125µm) particles **a)** Different mass concentrations are within a linear trend for up to 260 g/m³, the plateau value at 456 g/m³ was excluded from the linear fit and is marked in red. **b)** Light scattering - photodiode hit rate - correlation for Al_2O_3 (90 - 125µm) particles shows a good correlation between the two methods.*

Up to 260 g/m³ a linear correlation was found between signal intensity and particle mass concentration with an $R^2 = 0.98$ for n = 18. Beyond 260 g/m³ the loaded gas is optically too dense, and the linear trends flattens into a saturation plateau, corresponding to the data point coloured in red in Fig. 3a. A similar trend was found for the same species measured by photodiode plasma counting (hit

rate), which will be discussed later (Fig. 5) in more detail. Merging both results via the common mass concentration axis shows the well correlating linear trend between the two features, as shown in Fig. 3b. It also shows that light scattering and photodiode plasma counting approach their respective plateaus in a similar trend, leading to a linear correlation over the entire investigated mass concentration range. These results underline the fact that particle number density correlates with the intensity of light scattered by the particles. Assuming a high sphericity of the particles allowed for the calculation of a sphere diameter, as an intuitive size descriptor. To confirm this, stroboscopic imaging was added to obtain the shape information of the particles.

3.2. Shadowgraphy and Shape factors

Five size fractions of Al_2O_3 particles were prepared by analytical sieving from commercially available batches. Each size fraction was analysed by stroboscopic imaging to directly obtain a full set of shape descriptors, as well as the size information. Briefly, shape descriptors determine how close a filled, two-dimensional shape is to a perfect circle, for more details, see S 2. The descriptors aspect ratio, roundness and solidity of the used particles confirm that particles are close to a circle, see Fig. 4a. Circularity was omitted as a shape descriptor because the edges of the particles in the frame were too pixelated which led to an artificial, yet drastic, increase in their perimeter, decreasing their circularity. All three dimensionless shape descriptors show values around 0.8. With this data and orientation-averaged sampling the particles, the previously assumed sphericity, a three-dimensional shape descriptor of how sphere-like a particle is, was confirmed. A trend can be seen throughout all three descriptors, that larger particles have a higher sphericity than smaller ones, hinting towards the resolution limitation of the used optical setup. A relative number density can be calculated assuming a homogenous porosity of the particles throughout the size range from 32 µm to 125 µm. This means that the smallest fraction (32 - 40 µm) contains 27 times as many particles as the largest fraction (90 - 125 µm) when the same volume is dosed, and the same particle size distribution and behaviour is assumed for all fractions. Particle detection in stroboscopic imaging strongly depends on the thresholds for size and intensity, especially if a particle occupies only a small portion of the frame area, *e.g.* less than 1%. This is enhanced by partially overexposed frames and shadow casting within a single frame. To ease this effect, the direct number density determination was used. By using a focal depth height of 0.3 mm and an observation size of 5.2 mm by 6.0 mm, the focal volume of the CCD observation was determined to be 7.35 mm^3. For this approach only the presence of a particle in this focal volume is considered, not its size in the frame. The number of particles in each frame was determined by using the ImageJ function *Particle Analysis* (threshold < 128, size > 10 px^2). This number of particles per frame is exemplified in Fig. 4b.

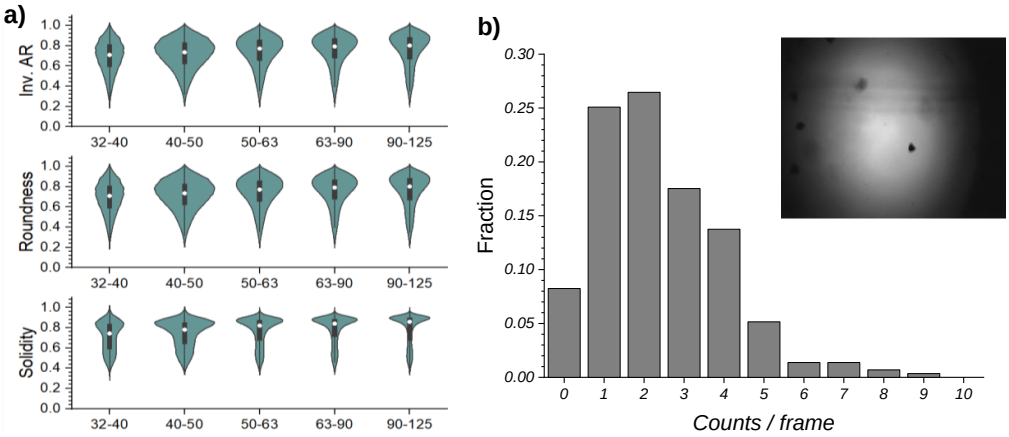

Fig. 4 ***a):*** *Three shape descriptors of the Al_2O_3 particle populations used in this work, all ranging around 0.8 and collectively confirming the particles' sphericity. The sphericity is highest for largest particles.* ***b)*** *The number of particles per frame histogram of the 90 - 125 µm Al_2O_3 particles, showing an average of 2.4 ± 0.34 particles per frame, resulting in a particle number density of (0.3 ± 0.04) mm^{-3}, the inset shows a single frame with a single particle being detected and a blurred particle in the top left not being detected.*

The obtained particle counts per recorded frame were used to determine the particle number density n in mm^{-3}, see eqn (1)[17]. Assuming a constant particle density throughout, the average particle diameter can be calculated.

$$d_P = \left(\frac{3\, Q_f}{\pi\, n\, Q_g\, \rho_P} \right)^{\frac{1}{3}} \qquad (1)$$

Here, d_P is the particle diameter [m], n the average particle number density [m^{-3}], ρ_P the particle density [kg m^{-3}], Q_f the feed of particle mass [kg s^{-1}] and Q_g[m^3 s^{-1}] the gas volume, both per unit of time. For an unknown mass concentration (Q_f/Q_g) this can also be calculated from the light scattering calibration curve shown in Fig. 3a. By using that equation, the average particle size was determined to be (92 ± 13) µm, which is within the size range of the input particles. Because the focal volume of the setup can be determined beforehand, is considered constant and independent of the investigated particles, this method can be considered reasonably calibration-free.

3.3. Laser-Induced Breakdown spectroscopy (LIBS)

After particle number density determination via stroboscopic imaging, the hit rate, measured by LIBS, was used to independently determine the particle number density and to back-up the stroboscopic results. Also, LIBS does provide the compositional information of the particles. Here, LIBS was used in a phase-selective breakdown mode, meaning that the fluence only sufficed for a plasma when there was a particle present in the respective effective focal volume. This ought to determine the particle number density and, combined with other methods, the effective focal volume. Again, the hit rate is defined as the number of detected events divided by the number of laser shots. A count refers to an

event where the light- and shockwave-emitting plasma was recorded. This can either be detected by recording the continuous light information with a photodiode, the emerging acoustic wave with a microphone or the discrete spectral light information by using a spectrometer. Obeying the same proportionality as the abovementioned light scattering, a higher mass concentration correlates with a higher hit rate. Identical to the light scattering measurements, this hit rate also shows an initial linear relation with the mass concentration before it plateaus off, which can be seen in Fig. 5. It shows that even at high mass concentrations of 456 g/m³, the highest hit rate was found to be 3.7%. Using an asymptotic fit that is, up to normalization, of the form $1 - b^x$, wherein x represents the mass concentration of particles (Q_f/Q_g) in g per m³, an expected hit rate of 3.5% ± 0.2% was determined. This means that the effective focal volume, defined as the space which is considered to have sufficient fluence to ignite a plasma, must be small and therefore empty most of the time. This includes the approximation that the particles, moving with a velocity of 1 m/s, can be considered stationary for the duration of the 6 ns laser pulse. The pulse energy was found to be proportional to the hit rate as can be seen in the inset of Fig. 5. This data shows a LIBS-onset using a pulse energy of 1.1 mJ or more, corresponding to 14 J/cm² at the beam waist of 100 µm in diameter, *i.e.* $\omega_0 = 50\ \mu m$.

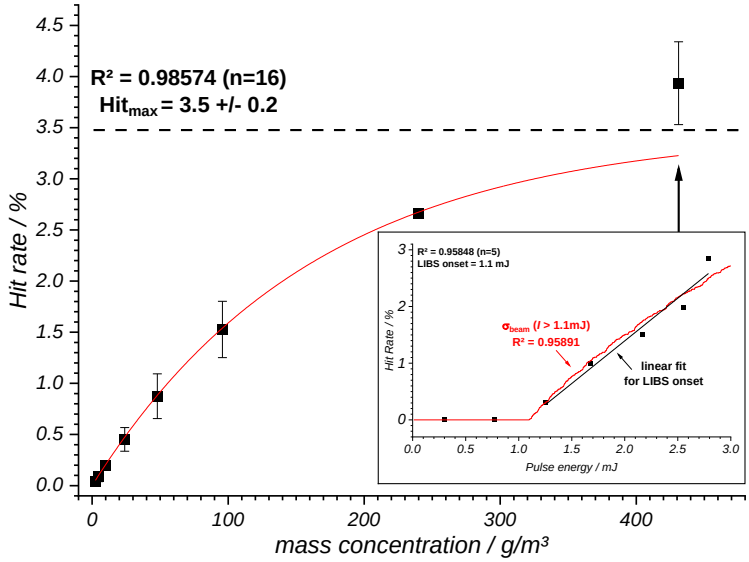

Fig. 5 Hit rate data of Al_2O_3 particles 90 - 125 µm in diameter for different mass concentrations of particles in the carrier gas. The highest measured hit rate under the here shown conditions was 3.7%, which surpassed the estimated plateau of 3.5% ± 0.2 %. Inset: Event frequency versus pulse energy at a particle mass concentration of 456 g/m³. The onset of LIBS for Al_2O_3 was determined to be 1.1 mJ or 14 J/cm² at beam waist. The calculated hit rate, based on the beam's cross section, is shown in red and is in good agreement with the experimental data (R² = 0.96)

Because LIBS is threshold-limited, this hit rate increase can be explained by an increased effective focal volume. The Intensity distribution within the beam can be expressed by using eqn. 2,

$$I(r,z) = I_0 \left(\frac{\omega_0}{\omega(z)}\right)^2 exp\left(\frac{-2r^2}{\omega^2(z)}\right) \quad (2)$$

wherein z is the distance from the beam waist ω_0, and r the distance from the beam axis, wherein the condition of $\omega_0 \gg \lambda_{1064\ nm}/n_{air}$ is met for the experimental setup with $50\ \mu m \gg 1\ \mu m$.[32–34] The propagation of the gaussian beam width $\omega(z)$ is expressed as shown in eqn. (3)

$$\omega(z) = \omega_0 \sqrt{1 + \left(\frac{z}{z_R}\right)^2} \tag{3}$$

with $z_R = \pi {\omega_0}^2 n/\lambda$ this can be used in eqn. (3) to calculate the intensity $I(r,z)$ which was done in a mesh grid ($2.5 \cdot 10^5$ points).[32–34] The number of points of $I(r,z)$ that exceed the 1.1 mJ LIBS threshold, in relation to the total number of points of the gaussian beam, lower bound at $I(r,z)_{\,cut-off} = 0.01$ mJ, is representative of the area and therefore effective focal volume. This fraction correlates well with the experimental hit rate. It is shown as the red line in in the inset of Fig. 5 labelled with as $\sigma_{beam} > 1.1\,mJ$. It shows a very good coefficient of determination of 0.96. This suggests that the increase in hit rate is caused primarily by the increase in effective focal volume.

In-situ effective focal volume determination. As shown above, the size of the effective focal volume is a crucial parameter to be able to convert the hit rate to an absolute particle number density. Also, the data shows an onset for LIBS events of Al_2O_3. Furthermore, as will be shown later, there is a transition from LII events to LIBS events for $CuFeS_2$ particles. The experimental hit rate is a convolution of particle number density statistics and the plasma efficiency statistics. Here, the particle number density statistics describes the likelihood that at least one particle is in the region where a LIBS event is possible, based on the fluence in that region. The plasma efficiency statistics describe the chance of plasma ignition when a particle is in a region of a certain fluence. The plasma efficiency for the Al_2O_3 and $CuFeS_2$ particles was determined using a setup that ensured a densely populated particle stream, 2.4 mm in diameter. Starting the measurements, the focal point was located at a 5 mm distance from the centre of the particle stream and was moved towards the particle stream in 0.5 mm steps. The plasma events were recorded using the photodiode. Here, the plasma efficiency which is the ratio of flash events detected by the photodiode over the number of laser shots, was calculated for each distance. For $CuFeS_2$ and Al_2O_3 the plasma efficiency was determined to be 96% ± 3 % and 99% ± 1% respectively (see S 5). This led to the conclusion that for all practical purposes, the chance of LIBS ignition when there is a particle in the effective focal volume is 1. The low hit rate as mentioned above, therefore requires high laser repetition rate so that enough LIBS events are created for a near real-time measurement.

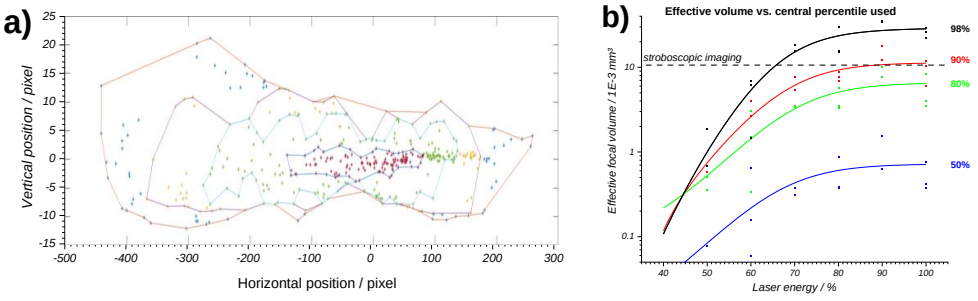

Fig. 6 ***a)*** *Spatial LIBS event distribution with convex hulls around the central 98th (largest), 90th, 80th and 50th (smallest) percentile at the maximum laser fluence.* ***b)*** *Effective focal volume determined by rotating the convex hull of the central 98th, 90th, 80th and 50th percentile, depicted in black, red, green, and blue, respectively. As a reference, the converted volume determined by stroboscopic imaging was calculated.*

With these parameters in place, the effective focal volume can be calculated. For this, a CCD camera was directed to the LIBS plane and captured the intensity as well as the position of an event. Again, since the LIBS event was caused by a 6 ns short pulse and the particles moved with a velocity of about 1 m/s, it can be assumed that the events stand still within a single frame. Because of optical shielding

(shadowing) only the half on the side of the incident laser beam can be captured properly. Because this effect depends on the particle mass concentration of the gas, all measurements were carried out with the same particle population at a constant particle mass concentration. Subsequently, each frame the camera recorded was searched for particles. A spatial distribution of the events can be seen Fig. 6a and in more detail in S 3. The determination of the effective focal volume is based on concave hull obtained from that spatial distribution. The volumes are given in central percentiles, *e.g.* the central 80 percentile includes all data points from 10^{th} to the 90^{th} percentile. The convex hulls and the respective percentile are labelled in Fig. 6a. Each data of a certain percentile was used to calculate the respective solid of revolution of the median corrected data. This delivered an effective focal volume in cubic pixels which was converted to cubic millimetres to give an absolute effective focal volume. For more details in the data treatment and scaling factor determination see S 3. This procedure was repeated for multiple pulse energies and the result is shown in Fig. 6b. Here, each dataset and respective fit represents the effective focal volume that was calculated using the data of that respective central percentile. Using the previously calculated particle number concentration of 0.3 mm^{-3} from the stroboscopic imaging, and taking the hit rate of 3.5% into account, a very similar effective volume of 0.01 mm^3 was calculated which is also depicted as dashed horizontal line in Fig. 6b. This shows that the stroboscopic imaging combined with the hit rate and the scaled spatial event distribution can both be used to determine the effective focal volume.

Single particle compositional analysis. To determine the composition of the particle, laser-induced breakdown spectroscopy (LIBS) was used. In the presented work aluminium- (Al_2O_3) and copper-bearing ($CuFeS_2$) particles were chosen. Both moeities deliver accurate and precise spectral features as shown in the top row of Fig. 7. For each laser shot an individual spectrum was recorded. The resulting single-shot-single-particle spectra were background corrected with a tophat filter using a square structural element of size eight. For the particle classification, the maximum intensity from 307 nm to 310 nm and from 323 nm to 329 nm was used for Al_2O_3 and $CuFeS_2$, respectively. Here, because the peak intensities showed a higher robustness than the peak areas, intensities were used for evaluation. This was further justified by the fact that the shape of peaks was identical within a single run. Since each laser-triggered spectrum has a time stamp, the recorded maximums can be plotted over time, as shown in the bottom row in Fig. 7. Each data point represents the Al-I or Cu-I line intensity from a single laser shot. For a single data set 16383 spectra were recorded over a time of 32.766 s. As shown in the bottom row of Fig. 7, the LIBS spectra have an excellent signal-to-noise ratio (SNR) for Al_2O_3 and a good SNR for $CuFeS_2$. The lower SNR of the $CuFeS_2$ signals, however could be increased using a higher fluence. Each intensity that surpasses the median of the background signal by 5σ of that background represents a plasma and therefore one single particle. Given the low hit rate and small effective volume as shown above, the occurance of a double plasma, although principally possible, is highly unlikely and therefore may be excluded for all practical purposes.

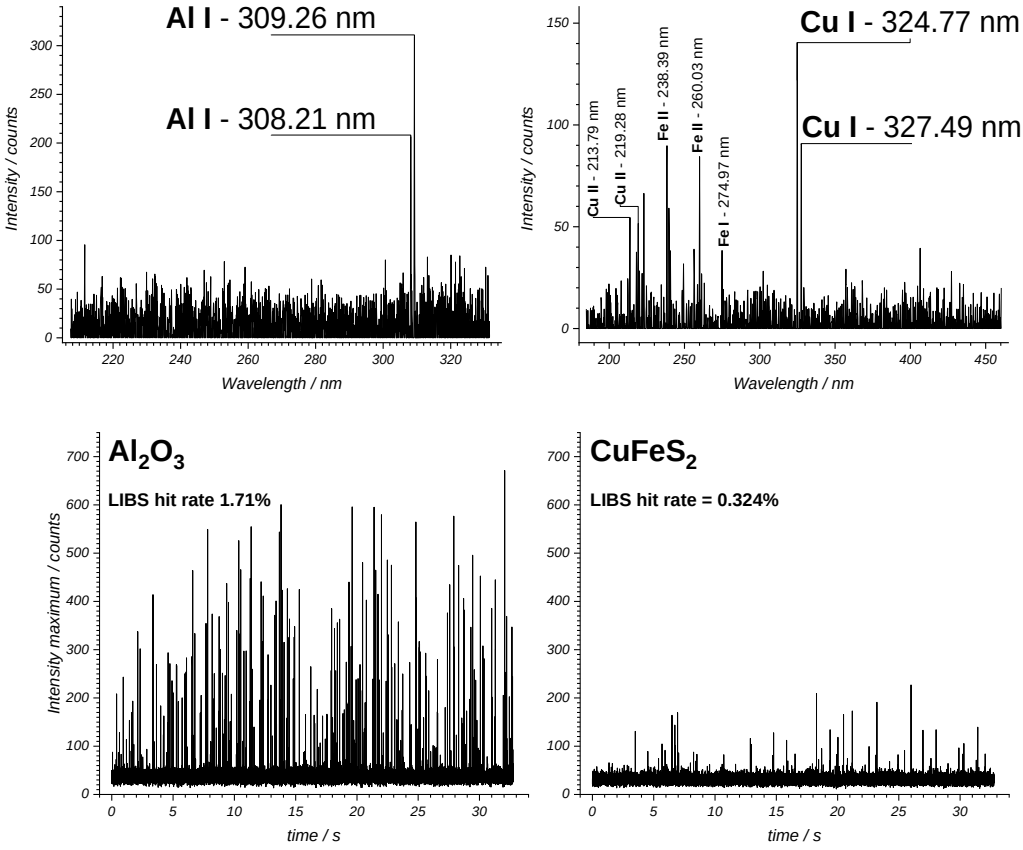

Fig. 7 Single particle LIBS spectra of Al_2O_3 and $CuFeS_2$ (integration 1.5 ms, delay 0.50 µs). The data was tophat-filtered with a square structural element of size eight. A hit was counted when the signal exceeded the $median_{BG}$ by $5\sigma_{BG}$. This resulted in a LIBS hit rate of 1.71% and 0.324% for Al_2O_3 and $CuFeS_2$ respectively.

Photo- and photoacoustic detection. Photo- and photoacoustic detection present excellent means for event counting. It is cost-effective, and especially in the case of the photodiode with its 100 kHz sampling rate and a rise time of 1 ns, it was suited as the master detector for all methods used in this study. Using simple light collection optics its observation range was enhanced, greatly facilitating its alignment and at the same time provide reliable, robust data. Given the radial propagation of the acoustic signal, the microphone for the photoacoustic detection had an even larger sampling volume, including regions being out of plane width the actual laser plane. Thus, both can be considered cost-effective and robust detection methods for particle counting in any process analytical environment. A trace of both signals is shown in Fig. 8a, with a 20x horizontal zoom on the right to show the details of the signal at 968 ms and its decays. Both maxima were plotted as shown in Fig. 8b. This yields a good correlation between the photodiode and photoacoustic signal with $R^2 = 0.86$ and $n = 3377$. This shows that a bright event is likely to also have a strong acoustic response, meaning that more mass was ablated during such an event. This can now be related to the obtained spectral lines of that event aiming to establish a normalization procedure for the LIBS line signal.

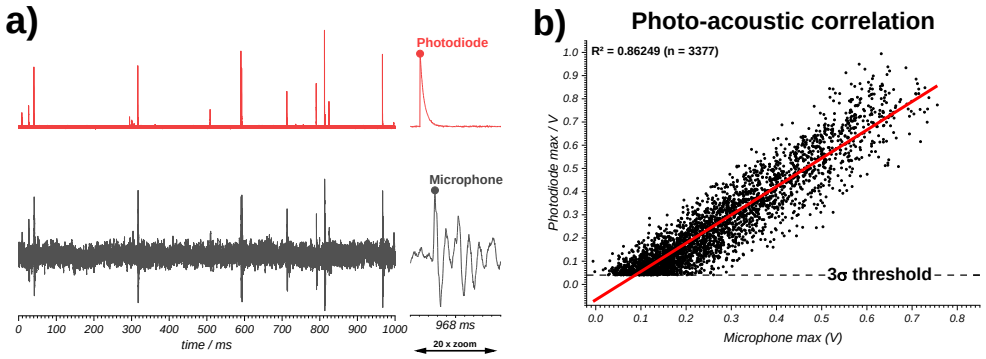

Fig. 8 ***a)*** *Oscilloscope signal trace of the photodiode and microphone recording events from a laser (λ = 1064 nm, E = 2.7 mJ, f = 500 Hz, t = 6 ns). The right part is a 20-fold time-axis zoom to the show the last signals' details and its decay properties. The maximum in each trace is marked as such and represents one datapoint pair plotted in right panel.* ***b)*** *Maximums of the microphone and photodiode signals. A photodiode threshold of 3σ was used for the finding of the peaks and is depicted as a horizontal dashed line. The linear fit shown in red shows a good coefficient of determination of 0.86 using 3377 data points.*

Photoacoustic normalization. The normalization of the LIBS signal with the photoacoustic signal was executed in various versions including, but not limited to, combinations of the respective line intensity, acoustic and photodiode signals. For all options, the coefficient of variation (CV), defined as the population's standard deviation σ over its mean μ, did not improve significantly. This becomes more apparent when visualizing the entire populations before and after the normalization options, as can be seen in Fig. 9a. The left half of the violin plot (red) shows the kernel density estimate (Kernel smooth with ''Scott'' derived kernel width) of the data set before photoacoustic normalization. The data shown in red was range normalized, not photoacoustic normalized, and showed a mode (broad peak) just below 0.2 and at 0.6. The right half of the violin plot (blue) shows the population after the photoacoustic normalization also in its range-normalized form. The main mode remains around 0.2 and the mode at 0.6 is shifted towards 0.4. The most impact, however, did the photoacoustic normalization have on the small mode at 0.9, see the inset of Fig. 9a. From this one can conclude that different parts of the population may be affected differently by photoacoustic normalization.

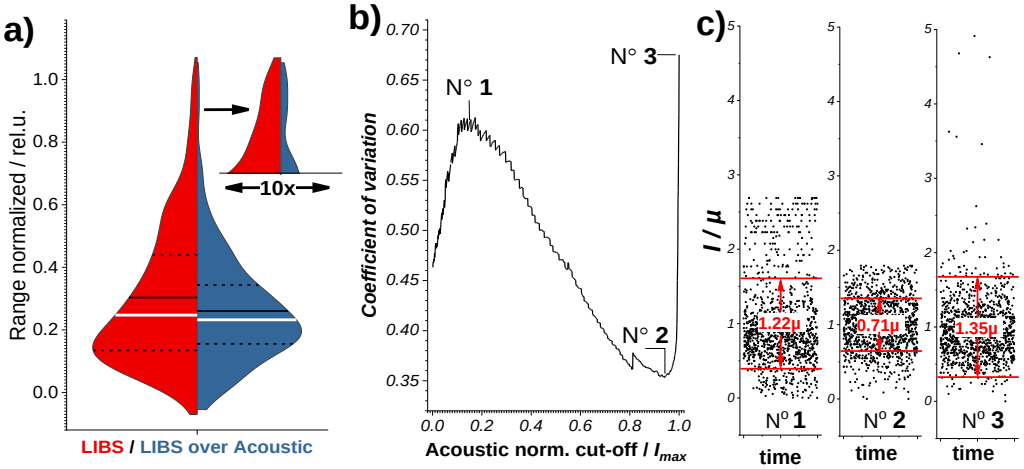

Fig. 9 ***a)*** *Visualization of LIBS range-normalized LIBS line intensities before (left, red), i.e. LIBS, and after (blue, right) photoacoustic normalizations, i.e. LIBS over acoustic. The statistic descriptors mean (white, solid), median (black, solid) and*

the 25 and 75 percentiles (black, dashed) are annotated. The inset at the top shows a horizontal zoom of the upper fraction of the population, where the photoacoustic normalization shows the strongest effect. ***b)*** *Shows how the coefficient of variation depends on what size the normalized subset has. The photoacoustic-normalized subset contains all elements, that exceed a fraction of the maximum intensity I_{max} (cut-off). 1,2 and 3 show extreme CV values. The minimum is produced when all values exceeding 0.94·I_{max} are normalized.* ***c)*** *Shows three distinct populations marked in b) as 1,2 and 3 representing a population with a CV of 0.61, 0.35 and 0.68 respectively, to visualize the effect acoustic normalization.*

To investigate this in more detail, the population, ranked by LIBS intensity, was cut into two subsets, using a percentile threshold. All values larger than this percentile threshold were normalized by the photoacoustic signal. The values equal or smaller than this threshold remain unchanged. After merging both range-normalized subsets again, the CV of the complete dataset was calculated. As can be seen in Fig. 9b, this calculated CV does change significantly, depending on size of that normalization window. In this graph a 0.5 audio-normalization fraction means that only the largest 50 % of the line intensities get normalized by the photoacoustic signal. The data shows that not normalizing by the photoacoustic signal ($x = 1$, thus $I > 1 \cdot I_{max}$) as well as the normalizing all the data points ($x = 0$, thus $I > 0 \cdot I_{max}$) both result in higher CVs than the optimum at round 0.94. This effect is visualized in Fig. 9c, wherein the respective populations, marked in Fig. 9b, are shown their mean-normalized form. As a visual guide, the $\mu \pm 1\sigma$ spans are marked in red with the widths annotated. The physical interpretation of these results can be based on the signal-to-noise ratio of the photoacoustic data. Because the photoacoustic signal is measured in-line, the noise level is high, including but not limited to echoing effects, as can be seen Fig. 8 and Fig. 10. Low photoacoustic values thus merge with the noise, which in turn are then introduced into the LIBS signal as such. This effect is seen in the first half of Fig. 9b ($0 \leq x \leq 0.2$) where the CV rises, because more noise than signal is introduced into the dataset by the normalization. A restriction of the normalization to be applied only if the LIBS signal is sufficiently high, gradually decreases the CV ($0.2 \leq x \leq 0.95$). If the number of normalized data points decreases more and more, the CV increase again ($0.95 \leq x \leq 1.00$). In the end, this CV-based normalization method is very helpful for photoacoustic normalization when the signal-to-noise ratio is compromised as it is often the case for real-life and in-line measurements.

3.4 Laser-induced incandescence

While white Al_2O_3 and slate-grey $CuFeS_2$ particles are both equally well-suited for LIBS, their suitability for laser-induced incandescence (LII) differs greatly. In the setup used so far, incandescence was only found for the $CuFeS_2$ particles. Therefore, the following direct comparison of LII with LIBS is solely based on the $CuFeS_2$ particles. A non-focused laser beam, 1 mm in diameter, was used for LII, probing a total in-tube volume of 5.5 mm^3. As described above a LIBS event is recorded by a photodiode, a microphone, and a spectrometer. In addition, an eight-bit CCD camera was used to capture the events. As can be seen in Fig. 10a, when measuring the LII mode, events detected by the CCD camera did not lead to a detectable acoustic signal nor to LIBS lines detected by the spectrometer. This confirms that these events are, indeed, no LIBS events, but LII events. Using a frame-by-frame event detection using ImageJ, the mean brightness of each event could be evaluated. As can be seen in Fig. 10b, there is a clear distinction between mean brightness produced by LII and LIBS events using the 8-bit CCD camera. This further confirms that the LII setup does not create LIBS events and vice versa.

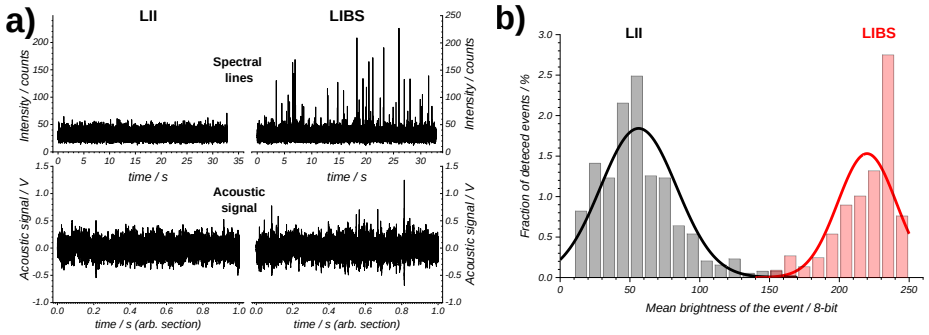

Fig. 10 Data acquired from measuring $CuFeS_2$ (50 - 63 µm) particles. ***a)*** *The top row compares the number of spectral lines of the LIBS mode (focused laser) with the LII mode (unfocused laser). The repetition rate of 500 Hz and the 32.7 s measuring time correspond to 16383 individual spectra. In each spectrum the maximum intensity of the region from 323 nm to 329 nm was taken and plotted here. A substantial number of LIBS events was found in the LIBS mode, and none were found in the LII mode. This indicates that in the LII modes no plasma was formed. The bottom row compares the acoustic signal in the LIBS mode and the LII mode. Here, there is significantly fewer events in the LII compared to the LIBS mode.* ***b)*** *Two plots of merged into one, show the distribution of the mean intensity of a single event detected by the 8-bit CCD camera. Two separated intensity modes are clearly visible. Also, in the LIBS measuring mode, the vast majority of events reached saturation. Both modes can clearly be distinguished from one another in terms of brightness.*

Since the probing volume of LII is much larger, it was interesting to see how this affects the hit rate, described earlier. This time, the hit rate refers to LII events not to LIBS events. For this experiment, a laser with a repetition rate of 100 Hz and a maximum fluence of 1.27 J/cm² was used, since the 500 Hz laser used until now has a maximum fluence of 0.3 J/cm² when non-focused. The reduced repetition rate is compensated by the much larger probing volume LII has compared to LIBS, increasing the chances of having a at least one particle in the probing volume. As shown in Fig. 11, LII was measured to have a hit rate, of 96 +/- 3% (see also S 5) compared to 3.5% for LIBS (Fig. 5). A frame was called a hit when it contained at least one event. Even at fluence as low as 0.13 J/cm² LII was detected for the slate grey $CuFeS_2$ particles. The stack on the right side of Fig. 11 shows the sum z-projection of the 2750 frames for all shots. Due to frame-per-second recording limitation of the CCD camera, only 2750 of the total number of 5500 laser shots were recorded. It can also be seen that the occurrences of LII events increase from 0 - 0.5 J/cm² which is due to an increase in effective LII-volume, analogous to the effective focal volume for LIBS described earlier. From a fluence up to 0.5 J/cm² the effective volume reached a size where there is a particle present in the effective LII volume at almost any point in time. By further increasing the fluence the effective LII volume grows to sizes that contain more than one particle at almost any time (see also **Error! Reference source not found.**). Since the hit rate counts all frame with at least one event identically, this trend above 0.5 J/cm² is not captured by this metric. If that metric was of interest, either a CCD camera could be used, as presented here, or using a photodiode with an iris, to adjust the probing volume respectively. For fluences above 0.5 J/cm² optical shielding effects (shadowing) of the laser light coming from the left, go into effect.

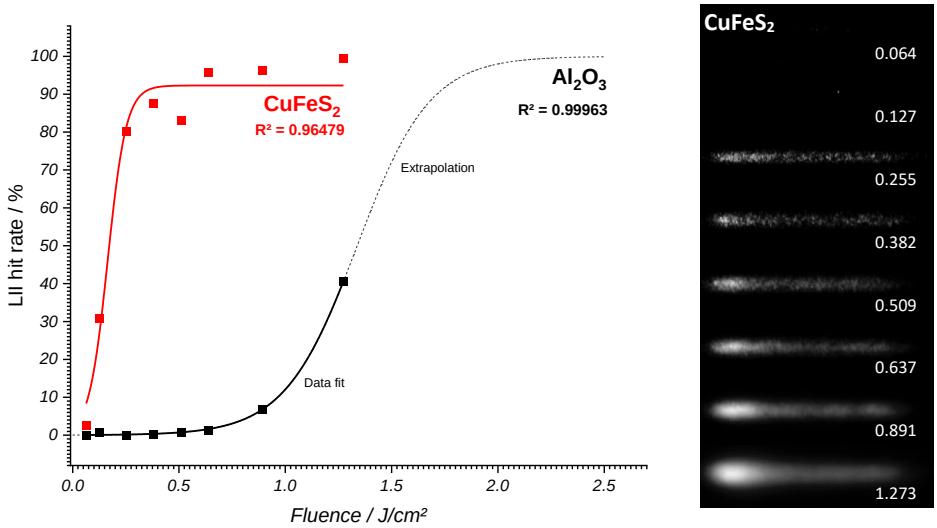

Fig. 11 Incandescence hit rate of LII using $CuFeS_2$ and Al_2O_3 (50 - 63 µm) particles, fitted by a Boltzmann sigmoid. For $CuFeS_2$ the hit rate plateaus from for fluences of 0.6 J/cm² and above at 95 ± 3%, thereby practically all laser shots create an LII event. For Al_2O_3 a much higher fluence of > 1.8 J/cm² (extrapolated) is required to achieve that 95% hit rate. The right stack shows the sum z-projection of the recorded events for 2750 frames at each fluence specified at the bottom right of each projection.

With the higher fluence available in this setup, remeasuring the Al_2O_3 particles showed that they do in fact exhibit LII, just at a higher fluence than previously available, which as can be seen in Fig. 11. LII events started appearing at fluences of 0.9 J/cm² and with increased rate at 1.3 J/cm². To compare both species, a Boltzmann sigmoidal curve was fitted with the maximum set to 100%. The hit rate for fluences above 1.3 J/cm² were extrapolated using that fit and yielded a value of 1.8 J/cm² to reach a 95% hit rate. Aside from achieving LII in white particles, this opened the doors to the realm of using LII as an in-flight analytical method. For the shown case of $CuFeS_2$ and Al_2O_3 a set of two fluences can be used to determine the composition of a binary mixture of the two. This can, in principle, can be expanded to more components. As a proof-of-principle, the blue-green-coloured turquoise $CuAl_6(PO_4)_4(OH)_8{\cdot}4H_2O$ and slate-green-coloured conichalcite $CaCu(AsO_4)(OH)$ were measured at a fluence of 0.25 J/cm² and 1.3 J/cm³. Both showed no incandescence at a fluence of at 0.25 J/cm² and showed incandescence at a fluence of 1.3 J/cm². A more detailed investigation of these minerals was outside the scope of this work; thus, these results remain qualitative. This is also a proof-of-principle for using incandescence to distinguish between different copper-bearing minerals based on the LII hit rate resulting from different fluences.

4. Conclusion

The presented work shows a comprehensive set of contactless, in-line, real-time methods to measure air-dissipated particles and aerosols. The employed techniques span from imaging, via single-event counting, to spectral compositional analyses. Herein, stroboscopic imaging embodied most of the size and shape information, confirmed the good sphericity of the used particles, and was used for measuring the number density. Combined with laser-induced breakdown spectroscopy (LIBS) CCD imaging was used for single-event counting, hence number density determination. Stroboscopic imaging, effective focal volume determination and event counting were in good agreement with one-another in terms of particle number density. The compositional analysis using LIBS was possible using

the single-particle-single-pulse spectra only. With synchronized photoacoustic measurements it was possible to normalize the LIBS line intensities. This reduced the coefficient of variation from 0.46 to 0.35 for the obtained data. For the first time, it was shown that laser-induced incandescence (LII) can be used for in-flight measurements of aluminium- and copper-bearing particles, paving the way for real-time analysis of industrial process. LII was proven to be a valuable alternative for particle counting and compositional aerosol classification. It can also quantify lower number densities than LIBS, due to its larger effective volume. The second novelty emerging from this work is the feasibility of LII as a particle classification method, based on their incandescence. Here, incandescence showed vast differences between Al_2O_3 and $CuFeS_2$ at different laser fluences, meaning that the signals are easily classifiable when choosing the correct fluence. This study also indicates that there is a difference in LII tendencies for different copper-bearing particles. The presented data of the latter, however, remained qualitative, given these minerals were not the main scope of the presented work. Nevertheless, it showed the immense potential laser-induced incandescence has for real-time, in-flight analysis of aerosols.

Acknowledgement

The authors would like to thank the project executing organization the German Aerospace Center as part of the Federal Ministry of Education and Research (Nr: 01DM19009A) of the for the financial support.

Authors' contribution

C.P. contributed by conceptualization and methodology for the complete setup, the investigation, data curation, validation, analysis, and software development as well as the complete writing process from draft to final editing. T.B. contributed by the conceptualization and supervision of and in the entirety of the project as well as in funding acquisition, project administration and writing review and editing O.R. was involved the conceptualization, software, and supervision of the light scattering setup as well as writing review and editing. HG.L. was involved in funding acquisition, project administration and writing review and editing.

References

1 i-Sccop, Industry 4.0 and the fourth industrial revolution explained, https://www.i-scoop.eu/industry-4-0/.

2 R. A. T J, Brown, N E Idoine, C E Wrighton, E R Raycraft, S F Hobbs and E. A. D. and C. K. Shaw, P Everett, *World Mineral Production*, BRITISH GEOLOGICAL SURVEY, Keyworth, Nottingham, British Ge., 2021.

3 A. Stokreef, J. A. Barnes, H.-P. Loock and B. Davis, in *Applied Industrial Optics 2019*, OSA, Washington, D.C., 2019, p. T3A.1.

4 G. Reyes, W. Diaz, C. Toro, E. Balladares, S. Torres, R. Parra and A. Vásquez, Copper oxide spectral emission detection in chalcopyrite and copper concentrate combustion, *Processes*, 2021, **9**, 1–14.

5 P. Gillard and M. Roux, Study of the Radiation Emitted During the Combustion of Pyrotechnic Charges. Part I: Non Stationary Measurement of the Temperature by Means of a Two-Color Pyrometer, *Propellants, Explos. Pyrotech.*, 2002, **27**, 72.

6 R. E. Hillman and Daryush D. Mehta, The Science of Stroboscopic Imaging., https://entokey.com/the-science-of-stroboscopic-imaging/.

7 A. Andreeva and N. Zografov, 2019, p. 160015.

8 A. Minichiello, D. Armijo, S. Mukherjee, L. Caldwell, V. Kulyukin, T. Truscott, J. Elliott and A. Bhouraskar, Developing a mobile application-based particle image velocimetry tool for enhanced teaching and learning in fluid mechanics: A design-based research approach, *Comput. Appl. Eng. Educ.*, 2021, **29**, 517–537.

9 S. Legnaioli, B. Campanella, F. Poggialini, S. Pagnotta, M. A. Harith, Z. A. Abdel-Salam and V. Palleschi, Industrial applications of laser-induced breakdown spectroscopy: a review, *Anal. Methods*, 2020, **12**, 1014–1029.

10 G. Teng, Q. Wang, X. Cui, G. Chen, K. Wei, X. Xu, B. S. Idrees and M. Nouman Khan, Predictive data clustering of laser-induced breakdown spectroscopy for brain tumor analysis, *Biomed. Opt. Express*, 2021, **12**, 4438.

11 Z. Gajarska, L. Brunnbauer, H. Lohninger and A. Limbeck, Identification of 20 polymer types by means of laser-induced breakdown spectroscopy (LIBS) and chemometrics, *Anal. Bioanal. Chem.*, 2021, **413**, 6581–6594.

12 F. Ringleb, S. Andree, B. Heidmann, J. Bonse, K. Eylers, O. Ernst, T. Boeck, M. Schmid and J. Krüger, Femtosecond laser-assisted fabrication of chalcopyrite micro-concentrator photovoltaics, *Beilstein J. Nanotechnol.*, 2018, **9**, 3025–3038.

13 Z. Wang, Y. Deguchi, F. Shiou, J. Yan and J. Liu, Application of Laser-Induced Breakdown Spectroscopy to Real-Time Elemental Monitoring of Iron and Steel Making Processes, *ISIJ Int.*, 2016, **56**, 723–735.

14 M. Gaft, I. Sapir-Sofer, H. Modiano and R. Stana, Laser induced breakdown spectroscopy for bulk minerals online analyses, *Spectrochim. Acta Part B At. Spectrosc.*, 2007, **62**, 1496–1503.

15 NASA, ChemCam for Scientists, https://mars.nasa.gov/msl/spacecraft/instruments/chemcam/for-scientists/.

16 NASA, SuperCam for Scientits, https://mars.nasa.gov/mars2020/spacecraft/instruments/supercam/for-scientists/.

17 J. E. Carranza and D. W. Hahn, Sampling statistics and considerations for single-shot analysis using laser-induced breakdown spectroscopy, *Spectrochim. Acta Part B At. Spectrosc.*, 2002, **57**, 779–790.

18 G. Kim, K. Kim, H. Maeng, H. Lee and K. Park, Development of Aerosol-LIBS (Laser Induced Breakdown Spectroscopy) for Real-time Monitoring of Process-induced Particles, *Aerosol Air Qual. Res.*, 2019, **19**, 455–460.

19 G. Xiong, S. Li, Y. Zhang, S. G. Buckley and S. D. Tse, Phase-selective laser-induced breakdown spectroscopy of metal-oxide nanoparticle aerosols with secondary resonant excitation during flame synthesis, *J. Anal. At. Spectrom.*, 2016, **31**, 482–491.

20 Y. Zhang, S. Li, Y. Ren, Q. Yao and C. K. Law, Two-dimensional imaging of gas-to-particle transition in flames by laser-induced nanoplasmas, *Appl. Phys. Lett.*, 2014, **104**, 023115.

21 F. Huang, Y. Tian, Y. Li, W. Ye, Y. Lu, J. Guo and R. Zheng, Normalization of underwater laser-induced breakdown spectroscopy using acoustic signals measured by a hydrophone, *Appl. Opt.*, 2021, **60**, 1595.

22 P. K. Diwakar, K. H. Loper, A.-M. Matiaske and D. W. Hahn, Laser-induced breakdown spectroscopy for analysis of micro and nanoparticles, *J. Anal. At. Spectrom.*, 2012, **27**, 1110.

23 R. Hadef, K. P. Geigle, W. Meier and M. Aigner, Soot characterization with laser-induced incandescence applied to a laminar premixed ethylene–air flame, *Int. J. Therm. Sci.*, 2010, **49**, 1457–1467.

24 K. P. Geigle, J. Zerbs, R. Hadef and C. Guin, Laser-induced incandescence for soot measurements in an aero-engine combustor at pressures up to 20 bar, *Appl. Phys. B*, 2019, **125**, 96.

25 C. Schulz, B. F. Kock, M. Hofmann, H. Michelsen, S. Will, B. Bougie, R. Suntz and G. Smallwood, Laser-induced incandescence: recent trends and current questions, *Appl. Phys. B*, 2006, **83**, 333–354.

26 H. A. Michelsen, C. Schulz, G. J. Smallwood and S. Will, Laser-induced incandescence: Particulate diagnostics for combustion, atmospheric, and industrial applications, *Prog. Energy Combust. Sci.*, 2015, **51**, 2–48.

27 F. P. Hagen, R. Suntz, H. Bockhorn and D. Trimis, Dual-pulse laser-induced incandescence to quantify carbon nanostructure and related soot particle properties in transient flows – Concept and exploratory study, *Combust. Flame*, 2022, 112020.

28 G. Xiong, Y. Zhang, C. Schulz and S. Tse, Molecular Emissions from Stretched Excitation-Pulse in Nanosecond Phase-Selective Laser-Induced Breakdown Spectroscopy of TiO2 Nanoaerosols, *Appl. Spectrosc.*, 2022, 000370282110725.

29 S. Talebi-Moghaddam, S. Robinson-Enebeli, S. Musikhin, D. J. Clavel, J. C. Corbin, A. Klinkova, G. J. Smallwood and K. J. Daun, Multiphoton induced photoluminescence during time-resolved laser-induced incandescence experiments on silver and gold nanoparticles, *J. Appl. Phys.*, 2021, **129**, 183107.

30 D. Allen, H. Krier and N. Glumac, Nano-Alumina Accommodation Coefficient Measurement Using Time-Resolved Laser-Induced Incandescence, *J. Heat Transfer*, , DOI:10.1115/1.4033642.

31 T. A. Sipkens, N. R. Singh and K. J. Daun, Time-resolved laser-induced incandescence characterization of metal nanoparticles, *Appl. Phys. B*, 2017, **123**, 14.

32 K. F. Renk, *Basics of laser physics: for students of science and engineering*, 2012.

33 R. Paschotta, 2008, p. 271.

34 EdmundOptics, Laser Optics Resource Guide, Section 2.1. Gaussian Beam Propagation, https://www.edmundoptics.eu/knowledge-center/application-notes/lasers/gaussian-beam-propagation/.

4

Discussion

4.1 Overall scientific impact

The scientific work presented contributed to further the understanding and application of the ionization process of IR-MALDI from small ions to particulate matter and therefore over several orders of magnitude, spanning from molecular *E*-*Z* differentiation to aerosol particles. Advances for the field of physical chemistry as a whole, were, in all cases, achieved by a novel configuration and unification of a variety of measuring principles. The combination of IR-MALDI with microfluidics, IMS and DMA, as well as LIBS and LII with imaging and acoustic techniques, extended the anlytical range of every method into new parameter spaces.

It started with the combination of the electric field-free IR-MALDI with microfluidics that established its seamless coupling with ion mobility spectrometry. Microfluidics offers a high level of reaction condition control and a multitude of functionalizations. The feature of dead volume-free mixing made it possible to use 2940 nm IR-MALDI to monitor reactions in pure acetonitrile since the reaction mix could be diluted by water just before exiting the microfluidic chip. Moreover, because IR-MALDI is electric field free, it was possible to install a repeller electrode to support the pressure-driven ion cloud transfer from the ambient-pressure ionization region to the reduced-pressure IM spetrometer, which did not distort the IR-MALDI itself. From this unique combination emerged a fast enantiomer-selective screening process for a multitude of catalysts to be tested within a few minutes each and with a mere fraction of resources necessary for bulk synthesis. Consequently, a high-throughput screening over a large range of reaction conditions can be reached, even more so when paralleled and automated using automation synthesis setups.

After that, the application of IR-MALDI was extended to the ionization of sub-micron particles. One driver for that was the replacement of the uniformly used radiation-based charging, which is the conven-

tional ionization and gas-phase transfer method, by IR-MALDI. Another driver was the investigation of how IR-MALDI performs on entities exceeding the molecular size regime by orders of magnitude and how the core composition and surface functionalization affects that performance. Again, enabled by IR-MALDI being electric field free, it can be applied to bulk dimensions, practically eliminating any clogging, which is an omnipresent issue in routine ES or nebulizer applications. Using IR-MALDI that way permitted it to compete with the particle size-limited ES. IR-MALDI has proven itself to be suitable for the gas-phase transfer of suspended particles of up to 550 nm in nominal diameter, and investigated in terms of charge distribution statistics. Here, established gas-phase charge models were challenged and adjusted, revealing new aspects of the IR-MALDI charging process.

From here on, the analytical focus shifted from liquid-phase ablation of the particle matrix towards direct solid-phase ablation of the particles. Here, LIBS and LII were applied. LIBS was used in the phase-selective mode (PS-LIBS) at a high repetition rate and additionally monitored by photodiode and photoacoustic detection. For LIBS, the methodological innovation was grounded in the partial photoacoustic normalization of the LIBS line intensities, rather than that of all the intensities. It was demonstrated that this approach was more suitable for measurements taken in the gas stream rather than in an anechoic chamber, which is usually used in LIBS-related photoacoustics. Additionally, shadowgraphy, light scattering and CCD imaging was used to characterize the particles' shape, size and number concentration. In situ determined probing volumes of LIBS lead to an absolute number density determination based on hit rates. For shadowgraphy and CCD imaging, alternative approaches were also developed. Finally, fluence-dependent incandescence was proven to be valuable for the classification of metal-bearing aerosols. This revealed a completely new analytical dimension in the implementation of LII, universally applicable to in-flight particles in industrial processes.

4.2 Key scientific contributions

As described in the theory section, IR-MALDI was used for analytes dissolved or suspended in an aqueous matrix, given the unique absorption and ablation properties of water. In order to disengage from that limitation, a novel sample feeding method, preferably a miniaturized one, was sought for, which lead to a collaboration with the Belder and Zeitler groups, both at Leipzig University, Germany. Here, the Zeitler group provided the Ir- and Ru-containing photocatalysts and *E*-*Z* pairs. The Belder group provided a microfluidic chip reactor functionalized with a tightly meandering irradiation channel as well as a dead volume-free mixing junction to dilute the acetonitrile-solvated reaction mixture with water in various ratios before ejecting it in a free-standing liquid beam, the microbeam. An important chemical boundary condition is a precipitation-free merge of all mixtures involved. The task of our group was the coupling of that microbeam to an IM spectrometer. The reduced-pressure IM spectrometer, developed in-house, operating at 100 mbar, was chosen because it could resolve the *E*-*Z* pairs best and is an inherently fast detection technique. This hyphenation has not yet been reported, presumingly because a transfer of the ion cloud from the ambient-pressure ionization region to the reduced-pressure IM spectrometer driven by that pressure gradient alone was observed to be insufficient. By installing a high voltage-supplied repeller plate opposite of the IM spectrometer inlet, the first experimental challenge was solved. This way, it was possible to direct the ion cloud without interrupting the electric-field-free IR-MALDI process itself. Because of the miniaturization, flow rates as low as 0.5-3 µL/min could be used, thus a full run, including all rinsing steps, could be achieved with as little as 25 µL/min of sample with isomer concentrations in the low millimolar and catalyst concentrations in the micromolar ranges. The sample flow rate-dependent dead time was determined to be 60 s for a 1 µL/min flow rate, giving enough data to provide a statistically relevant baseline. The rising edge of the detection of the starting material in the yield spectrum revealed a rise time of 10 s, which is only limited by diffusion and mixing effects within the mixing and meandering channels. Because of the tightly meandering channel on the microfluidic chip, an irridiated cross section area of a 404 nm LED of only 1 cm^2 sufficed to guide photocatalysts to a full reaction yield. Since the setup is modular, a 365 nm LED could easily be retrofitted. Given the differences in spectral overlap between the photocatalysts and the LEDs, chemical reaction kinetics could be estimated based on rise times and maximum yields, however, not quantified explicitly. To quantify these yields, differences in ionization efficiencies, that were also confirmed by B3LYP/6-311+G(d,p)-based DFT calculations, needed to be experimentally calibrated. Once completed, the yield was quantified in terms of $\boldsymbol{Z}/(\boldsymbol{Z}+\boldsymbol{E})$ for all photocatalysts. Yet again, taking advantage of the fastness of the technique, where a three-fold measurement could normally be achieved within 10 min, including all rinsing steps, a 1 Hz sampling rate for the isomerization yield was achieved, which is well below the routinely used HPLC sampling rate of 0.00028 Hz, or once an hour, for a stirred batch reaction. The collective benefits of all these methods resulted in a powerful tool for quick screenings, with its cost, time and resource efficiency. This potential and its strive for greener chemistry, makes it the go-to setup to monitor reactions that require a fast yield sampling and very soft ionization method.

After establishing IR-MALDI as a bridging technique between microfluidics and ion mobility spectrometry, the second step into new territory was to implement it in the realm of differential mobility spectrometry. Here, gas-phase ionization is almost exclusively achieved by radiation sources such as ^{85}Kr, ^{210}Po or soft X-ray-coupled electrospray (xES), techniques that can be omitted for samples in a liquid matrix when using

IR-MALDI. In order to couple IR-MALDI to the DM spectrometer, an air-tight ionization chamber was developed to synergize the best of both worlds. In that chamber it was possible to apply IR-MALDI to a semi-bulk sample size, the hanging drop, where the dispersion and ionization takes place. The hanging-drop configuration eliminated the clogging often found in xES or nebulizer setups. Likewise, mechanical recoiling was introduced by using that hanging drop with a nominal diameter of 1 - 2 mm and thus enough moment of inertia. This vectored ion plume could be directed towards the DMA and monitored via stroboscopic imaging of the ionization chamber. To counteract thrust exerted by IR-MALDI on the hanging drop due to the mechanical recoil, a sheath gas flow capillary was coaxially mounted around the sample capillary. This secured the positioning of the hanging drop at the tip of the SST capillary. To further assist the ion cloud transfer, a second gas stream, the transfer sheath gas stream was employed. To evaluate the analytical performance of xES and IR-MALDI, they were compared directly to each other. The first noteworthy result was the similarity in primary droplet size distribution (PDSD) of IR-MALDI and xES, being centered around 400 nm and 300 nm respectively. Here, IR-MALDI produced a much broader PDSD, inherently making it the more promising ion source for investigating a broad range of nominal particle sizes. However, the advantages of the xES in that context, should not be underestimated. It performed well up to a particle size of 100 nm in nominal diameter using flow rates of 0.1-1 µL/min and had a higher sensitivity than IR-MALDI. Nonetheless, beyond that nominal particle size of 100 nm, increasing instabilities in the xES led to a full breakdown of the Taylor cone spray mode for particles close to 300 nm in nominal diameter. This rendered the investigation of sub-micron particles directly from suspensions with xES alone impossible. Therefore, implementing IR-MALDI for this case was not only beneficial because radiative ion sources could be omitted, but essential. IR-MALDI worked well up to nominal particle diameters of 550 nm and inherently produced only low charge states of the particles up to octuply charged species. Beyond that nominal size, the particle size distribution became too broad to assign charge states larger than two. A particle concentration limit was not observed for measurements with a maximum of 25 mg/mL in particle mass concentration. This unlocked a new analytical quality of the size distribution determination of sub-micron particles directly from suspension, previously only accessible by dynamic light scattering. The analytical advance is also founded in the much better resolving of DM compared to that of DLS, allowing for a significant reduction of the polydispersion index from 0.014 (DLS) to 0.002 (DM). Using that resolving power and an evaporation residual approach, it was possible to estimate that particles of a measured EM diameter of 185 nm were contained in primary droplets of 0.68 ± 0.12 µm in EM diameter, based on diameter differences of only a few nanometres. This is a level of precision unprecedented in characterizing particles of such dimensions.

Due to this precision octuply charged species were observed in well-resolved spectra. This observation, however, formed the gateway for a detailed investigation of the charge distribution produced by IR-MALDI, in general and when ionizing such large particles. The two literature-provided charging models are the Wiedensohler charge distribution for aerosols and the Poisson charge distribution for salt clusters. It was found that the bipolar gas charging model of Wiedensohler predicted a lower charge distribution for particles below a EM diameter of 287 nm and an equal one above that size, compared to the experimental findings in the IR-MALDI setup used. Adjusting the Poissonian distribution reproduced these experimental data best. This was indicative of the charge distribution having a significant Gaussian component. Challenging both charging models gave valuable insights into the IR-MALDI process as a whole and, at the same time, raised further questions about it. However, it was not possible to determine whether the charge distribution was a

direct outcome of the liquid-phase ablation, thus the actual charge distribution in the primary droplets, or that of a gas-phase recombination effect of these primary droplets, as it may occur in the early, high droplet density-number stage of the plume.

Shifting the focus towards even larger particles, the ablation method was shifted towards a shorter wavelength and applied in LIBS. Because the particles, or rather the particulate matter at this point, are of bulk dimensions, the ablated phase is now the solid phase and not the liquid phase any more. To ensure that only the solid phase was ablated actually, LIBS was used in the phase-selective mode. In this mode, LIBS did not only provide the composition information, but also a powerful and easily accessible particle counting method, either by wavelength-resolved, photodiode or photoacoustic detection. Combined with CCD imaging, it was possible to directly measure the effective focal volume of LIBS via a convex hull approximation. With this probing volume known, the direct and absolute determination of the particle number density was possible. The result aligned well with the purely stroboscopically determined value. The experimentally required threshold pulse energy for this LIBS setup was modeled theoretically and was able to reproduce the experimental values well. It confirmed that the observed increase in hit rate was likely due to an enlarging probing volume. The classification of a particle being either aluminum- or chalcopyrite-bearing was evaluated using the (309.26|308.21) nm emission line pair and the (324.77|327.49) nm emission line pair respectively. The hit rate for both pairs revealed that the plasma ignition was more prominent in aluminum-bearing (1.7%) than in the chalcopyrite-bearing (0.32%) particles for the same fluence and particle size distribution. In addition, and because LIBS was accompanied by photodiode and acoustic detection, the overall light intensity captured by the photodiode correlated well with the acoustic response. The photoacoustic output of a LIBS plasma, eventually relating to the plasma temperature, was used for developing an approach to normalize the LIBS line intensities. Although this type of normalization is not a new notion, the approach to preselect the respective signals is. The methodology developed is based on the coefficient of variation (CV) and determines the optimum intensity cut-off value for the normalization. It was shown that this resulted in a reduction of that CV by 25%. This is especially remarkable given all these measurements were conducted in line, with particle and gas velocities of 1 m/s at the tip of the microphone.

Related to LIBS, however occuring at much lower fluences, LII was also used to measure the particulate matter. For this, a 1064 nm laser beam with a 10 mJ pulse energy and a beam diameter of 1 mm was used to achieve fluences of up to 1.27 J/cm^2 when non-focused. This technique was first applied to the chalcopyrite aerosol particles, them being the easiest ones to trigger incandescence in. They exhibited a quantifiable amount incandescence from fluence of 0.13 J/cm^2 and above. Additional quantification of the particles involved CCD imaging. Every frame containing one or more LII events was counted as a hit. This delivered the hit rate, used for event quantification, but also showcased optical shielding effects, used for event localization. Here, the optical shielding implies that the event cloud shifted towards the direction of laser incidence, effectively decreasing the chance of LII of a particle the farther downstream it is located from the laser source. This inherently confines the detection volume for that technique in optically dense environments. With increasing fluence, the upper limit of single LII event quantification manifested itself at around five events per frame in a total detection volume of 5.5 mm^3. The measurement for aluminum oxide particles showed a quantifiable amount of LII events from fluences of 0.9 J/cm^2 and above. The upper fluence limit of 1.27 J/cm^2 caused the hit rate to not exceed 41% for the aluminum oxide case. However,

extrapolation of the available data pointed at fluences of 1.8 J/cm^2 or higher to achieve a full yield. Preliminary data shows that the LII onset in turquoise and conichalcite is in the same fluence range. Depending on the exact location and extent of the LII susceptibility curve, this broadens the analytical application of LII even more. This fluence specificity of the LII efficiency inspired a novel application. Given the LII susceptibility is vastly different for different chemical compositions and colors, an LII-based fluence screen can form the base for particle classification and, after calibration, also quantification. For this application, using a simple CCD camera or photodidiode, thus without any wavelength-resolved detection, would make for a robust, direct and cost-efficient classifier in a contactfree, in situ and real-time analysis for particulate matter in industrial processes.

5

Conclusion and outlook

Within the scope of this thesis, the application of IR-MALDI was broadened and its fundamental understanding deepened. The first inception and realization of an IR-MALDI microfluidics hybrid technique to study the photocatalytic performance in *E*-*Z* isomerization of olefins was shown. Using this microenvironment, photocatalyst screening times could be reduced from several hours in batch to only a few minutes. Because IR-MALDI is physically decoupled from the microchip reactor, the electrical properties of both regions are decoupled as well. This makes conductivity adjustments of the solvent, a ubiquitous procedure in ES, obsolete. This is an advantage that can be of general interest in the fields of single cell analysis or single droplet characterization, which is dominated by ES, and thus were solvent composition is a trade-off between the intended, native composition, and the ES requirements, a restriction absent in IR-MALDI. The use of concentration gradients and various final dilutions could be changed quickly by flow rate adjustments of each channel individually. To further these advances, a screen across other reaction solvents would be reveal the actual limits of IR-MALDI in the future. Because of its miniature design, all these screens can be done with a minimum amount of resources compared to batch reactions. By doing so, this thesis actively contributes to the field of green chemistry.

After optimizing the IR-MALDI source for a microbeam, it was transferred to a second liquid-based sample supply, the hanging drop. It was used for the charging of sub-micron particles directly from suspensions upon the gas-phase transfer, followed by their characterization with differential mobility (DM) analysis. By doing so, it surpassed the ES-imposed barrier for ionizing sub-micron particles of 100 nm in nominal size and extended the analytical range to a particle mass concentration of 25 mg/mL, previously only compatible with dynamic light scattering, however, at much lower resolving power. This thus shows the successful probing of suspended particles over four orders of magnitude. Aside from the ionization performance of IR-MALDI on unparallelly large particles, this thesis also presents a critical review of the established charging methods surrounding IR-MALDI and particulate matter. The developed method made octuply charged particles experimentally accessible in well-resolved spectra, which laid the foundation to derive a new charge distribu-

tion model. Both, the Wiedensohler charge distribution and a Poisson-derived charge distribution could not fully resolve the experimentally observed charge distribution. The iterative and comparative progression on charge model optimization eventually favored an adjusted Poisson-derived charge distribution model with significant Gaussian character to best fit the experimental results. Here, an expansion to other sub-micron species, such as gold or silver nanoparticles or large unilamellar vesicles, used in drug delivery systems, would very likely be the best tools to elaborate on the model's generality. At the same time this would boost its range of applications. In a more general sense, correlations between irregular particles and their mobility as well as non-reflective particle material, partially inaccessible by light scattering techniques, would further advance this range of applications. Moving forward to LIBS and LII particulate matter, both producing light emitting events, were used to quantify and classify these aerosols. The unique configuration of stroboscopic imaging, photoacoustics, LII and LIBS both contributed to the field of industrial in-process analytics and the latter also to the field of photoacoustic normalization. A 500 Hz and phase-selective low-fluence LIBS setup acquired statistically relevant amounts of data in a matter of seconds. Each plasma caused by the breakdown was localized and monitored spectroscopically, visually and photoacoustically. The data correlations within the scope of the thesis not only revealed great insights in the ablation process, but also disclosed new dimensions of information such as frequency to relate to the composition or size. This frequency-based approach, still in its infancy, however, would still require more detailed investigations in the future to find its applicability limitations in an industrial setting. LII was used in that context with a similar methodology as LIBS to quantify and classify particles of different compositions. Here, the particles were evaluated on their LII susceptibility expressed as a hit rate. Within the fluence range of only a few J/cm^2, it was possible to differentiate the LII onset of the slate grey chalcopyrite and pure white aluminium oxide. Preliminary data on blue green turquoise and slate green conichalcite particles also exhibit an LII onset within that regime. Future studies on particles of different chemical compositions but close in color, or even the other way around, would be the most practical way to pinpoint the specificity limits of that method. Eventually this would elevate LII to a full particulate matter classification technique.

In summary, this thesis provides a comprehensive view of laser-based ablation techniques promoted to new fields of operation, including, but not limited to, size, composition and number concentration analyses. At the same time, it reveals new facets of the IR-MALDI charging process, of the normalization methods in LIBS and of the applications for LII, thereby doing its part in making physical chemistry Minor, Citius, Vidirius.

Bibliography

[1] Tingting Tao et al. "Microengineered Multi-Organoid System from hiPSCs to Recapitulate Human Liver-Islet Axis in Normal and Type 2 Diabetes". In: *Advanced Science* 9.5 (2021), p. 2103495. DOI: 10.1002/advs.202103495.

[2] Mariana R. Carvalho et al. "Biomaterials and Microfluidics for Drug Discovery and Development". In: *Advances in Experimental Medicine and Biology*. Springer International Publishing, 2020, pp. 121–135. DOI: 10.1007/978-3-030-36588-2_8.

[3] Leyla Amirifar et al. "Droplet-based microfluidics in biomedical applications". In: *Biofabrication* 14.2 (2022), p. 022001. DOI: 10.1088/1758-5090/ac39a9.

[4] Yueyue Zhang et al. "From passive to active sorting in microfluidics: A review". In: *REVIEWS ON ADVANCED MATERIALS SCIENCE* 60.1 (2021), pp. 313–324. DOI: 10.1515/rams-2020-0044.

[5] Pedram Mehrabi et al. "The HARE chip for efficient time-resolved serial synchrotron crystallography". In: *Journal of Synchrotron Radiation* 27.2 (2020), pp. 360–370. DOI: 10.1107/s1600577520000685.

[6] Pedram Mehrabi et al. "Serial femtosecond and serial synchrotron crystallography can yield data of equivalent quality: A systematic comparison". In: *Science Advances* 7.12 (2021). DOI: 10.1126/sciadv.abf1380.

[7] Kim LM Hoang et al. "Traceless Photolabile Linker Expedites the Chemical Synthesis of Complex Oligosaccharides by Automated Glycan Assembly". In: *Journal of the American Chemical Society* 141.22 (2019), pp. 9079–9086. DOI: 10.1021/jacs.9b03769.

[8] Paul Watts and Charlotte Wiles. "Recent advances in synthetic micro reaction technology". In: *Chem. Commun.* 5 (2007), pp. 443–467. DOI: 10.1039/b609428g.

[9] Asli A. Dogan and Martin Dufva. "Customized 3D-printed stackable cell culture inserts tailored with bioactive membranes". In: *Scientific Reports* 12.1 (2022). DOI: 10.1038/s41598-022-07739-7.

[10] Alexander H. McMillan et al. "Rapid Fabrication of Membrane-Integrated Thermoplastic Elastomer Microfluidic Devices". In: *Micromachines* 11.8 (2020), p. 731. DOI: 10.3390/mi11080731.

[11] Karina Schuldt et al. "Applicability of PolyActive™ Thin Film Composite Membranes for CO2 Separation from C2H4 Containing Multi-Component Gas Mixtures at Pressures up to 30 Bar". In: *Membranes* 8.2 (2018), p. 27. DOI: 10.3390/membranes8020027.

[12] Crystal E. Rapier et al. "Microfluidic channel sensory system for electro-addressing cell location, determining confluency, and quantifying a general number of cells". In: *Scientific Reports* 12.1 (2022). DOI: 10.1038/s41598-022-07194-4.

[13] Clara Heinemeyer et al. "Surface Modification Procedure for Biosensor Chips Made of Chemically Sensitive Polymers". In: *Procedia Technology* 27 (2017), pp. 165–166. DOI: 10.1016/j.protcy.2017.04.072.

[14] Franziska D. Zitzmann et al. "Multielectrode biosensor chip for spatial resolution screening of 3D cell models based on microcavity arrays". In: *Biosensors and Bioelectronics* 202 (2022), p. 114010. DOI: 10.1016/j.bios.2022.114010.

[15] Hannes Westphal et al. "Unveiling Organocatalysts Action – Investigating Immobilized Catalysts at Steady-State Operation via Lab-on-a-Chip Technology". In: *ChemCatChem* 13.24 (2021), pp. 5089–5096. DOI: 10.1002/cctc.202101148.

[16] Nora T. Hartner et al. "Coupling Droplet Microfluidics with Ion Mobility Spectrometry for Monitoring Chemical Conversions at Nanoliter Scale". In: *Analytical Chemistry* 93.40 (2021), pp. 13615–13623. DOI: 10.1021/acs.analchem.1c02883.

[17] Martin Schirmer et al. "Conversion Efficiencies of a Few Living Microbial Cells Detected at a High Throughput by Droplet-Based ESI-MS". In: *Analytical Chemistry* 92.15 (2020), pp. 10700–10708. DOI: 10.1021/acs.analchem.0c01839.

[18] Lea Könemund et al. "Functionalization of an extended-gate field-effect transistor (EGFET) for bacteria detection". In: *Scientific Reports* 12.1 (2022). DOI: 10.1038/s41598-022-08272-3.

[19] Hend S. Magar, Rabeay Y. A. Hassan, and Ashok Mulchandani. "Electrochemical Impedance Spectroscopy (EIS): Principles, Construction, and Biosensing Applications". In: *Sensors* 21.19 (2021), p. 6578. DOI: 10.3390/s21196578.

[20] Emily E. Kempa et al. "Coupling Droplet Microfluidics with Mass Spectrometry for Ultrahigh-Throughput Analysis of Complex Mixtures up to and above 30 Hz". In: *Analytical Chemistry* 92.18 (2020), pp. 12605–12612. DOI: 10.1021/acs.analchem.0c02632.

[21] Minmin Tang et al. "On-line multi-residue analysis of fluoroquinolones and amantadine based on an integrated microfluidic chip coupled to triple quadrupole mass spectrometry". In: *Analytical Methods* 12.44 (2020), pp. 5322–5331. DOI: 10.1039/d0ay01641a.

[22] Hope Lackey et al. "A versatile and low-cost chip-to-world interface: Enabling ICP-MS characterization of isotachophoretically separated lanthanides on a microfluidic device". In: *Analytica Chimica Acta* 1137 (2020), pp. 11–18. DOI: 10.1016/j.aca.2020.08.049.

[23] José Villatoro. "A combined approach for the analysis ofbiomolecules using IR-MALDI ionmobility spectrometry and moleculardynamics simulations of peptide ions inthe gas phase". PhD thesis. University of Potsdam, 2018.

[24] Frank Wiederschein. "Investigation of Laser-Induced-Liquid-Beam-Ion-Desorption (LILBID) with-Molecular Dynamics Simulations". PhD thesis. University of Göttingen, 2009.

[25] Benoit Fatou et al. "Remote Atmospheric Pressure Infrared Matrix-Assisted Laser Desorption-Ionization Mass Spectrometry (Remote IR-MALDI MS) of Proteins". In: *Molecular Cellular Proteomics* 17.8 (2018), pp. 1637–1649. DOI: 10.1074/mcp.tir117.000582.

[26] Franz Hillenkamp. *MALDI MS - a practical guide to instrumentation, methods, and applications*. Hoboken: Wiley, 2013. ISBN: 3527333312.

[27] TSI. *Manual: Electrostatic classifier model 3082 and scanning mobility particle sizer model 3938*. TSI Incorporated. 2016.

[28] William . J. Sames et al. "The metallurgy and processing science of metal additive manufacturing". In: *International Materials Reviews* 61.5 (2016), pp. 315–360. DOI: 10.1080/09506608.2015.1116649.

[29] Myriam Millogo et al. "Combustion properties of titanium alloy powder in ALM processes: Ti6Al4V". In: *Journal of Loss Prevention in the Process Industries* 56 (2018), pp. 254–261. DOI: 10.1016/j.jlp.2018.09.003.

[30] Silvana De Iuliis, Roberto Dondè, and Igor Altman. "On Pyrometry in Particulate-Generating Flames". In: *Combustion Science and Technology* (2020), pp. 1–15. DOI: 10.1080/00102202.2020.1834391.

[31] Lian-Bo Guo et al. "Development in the application of laser-induced breakdown spectroscopy in recent years: A review". In: *Frontiers of Physics* 16.2 (Jan. 2021). DOI: 10.1007/s11467-020-1007-z.

[32] Ashwin K. Myakalwar et al. "LIBS as a Spectral Sensor for Monitoring Metallic Molten Phase in Metallurgical Applications—A Review". In: *Minerals* 11.10 (2021), p. 1073. DOI: 10.3390/min11101073.

[33] Reinhard Noll et al. "LIBS analyses for industrial applications an overview of developments from 2014 to 2018". In: *Journal of Analytical Atomic Spectrometry* 33.6 (2018), pp. 945–956. DOI: 10.1039/c8ja00076j.

[34] Ehsan Asadi Dalini et al. "A Review on Environmental, Economic and Hydrometallurgical Processes of Recycling Spent Lithium-ion Batteries". In: *Mineral Processing and Extractive Metallurgy Review* 42.7 (2020), pp. 451–472. DOI: 10.1080/08827508.2020.1781628.

[35] Fanghao Xu et al. "Application of Molecular Emissions in Laser-Induced Breakdown Spectroscopy: A Review". In: *Frontiers in Physics* 10 (2022). DOI: 10.3389/fphy.2022.821528.

[36] Jonas Petersson, M. Gilbert-Gatty, and A. Bengtson. "Rapid chemical analysis of steel slag by laser-induced breakdown spectroscopy for near-the-line applications". In: *Journal of Analytical Atomic Spectrometry* 35.9 (2020), pp. 1848–1858. DOI: 10.1039/d0ja00188k.

[37] David Girón et al. "In-situ monitoring and characterization of airborne solid particles in the hostile environment of a steel industry using stand-off LIBS". In: *Measurement* 115 (2018), pp. 1–10. DOI: 10.1016/j.measurement.2017.09.046.

[38] Huiwen Ji et al. "Review of aerosol analysis by laser-induced breakdown spectroscopy". In: *Applied Spectroscopy Reviews* 56.3 (2020), pp. 193–220. DOI: 10.1080/05704928.2020.1780604.

[39] Michał Wójcik et al. "Classification of Copper Minerals by Handheld Laser-Induced Breakdown Spectroscopy and Nonnegative Tensor Factorisation". In: *Sensors* 20.18 (2020), p. 5152. DOI: 10.3390/s20185152.

[40] Lu-Ning Li et al. "A review of artificial neural network based chemometrics applied in laser-induced breakdown spectroscopy analysis". In: *Spectrochimica Acta Part B: Atomic Spectroscopy* 180 (2021), p. 106183. DOI: 10.1016/j.sab.2021.106183.

[41] Yu Zhao et al. "Laser-Induced Breakdown Spectroscopy for the Discrimination of Explosives Based on the ReliefF Algorithm and Support Vector Machines". In: *Frontiers in Physics* 9 (2021). DOI: 10.3389/fphy.2021.675135.

[42] Sabrina Messaoud Aberkane et al. "Laser-Induced Breakdown Spectroscopy for Determination of Spectral Fundamental Parameters". In: *Applied Sciences* 10.14 (2020), p. 4973. DOI: 10.3390/app10144973.

[43] Yasser H. El-Sharkawy and Sherif Elbasuney. "Novel laser induced photoacoustic spectroscopy for instantaneous trace detection of explosive materials". In: *Forensic Science International* 277 (2017), pp. 215–222. DOI: 10.1016/j.forsciint.2017.06.005.

[44] Fuzhen Huang et al. "Normalization of underwater laser-induced breakdown spectroscopy using acoustic signals measured by a hydrophone". In: *Applied Optics* 60.6 (Feb. 2021), p. 1595. DOI: 10.1364/AO.413853.

[45] César Alvarez-Llamas et al. "LIBS-Acoustic Mid-Level Fusion Scheme for Mineral Differentiation under Terrestrial and Martian Atmospheric Conditions". In: *Analytical Chemistry* 94.3 (Jan. 2022), pp. 1840–1849. DOI: 10.1021/acs.analchem.1c04792.

[46] Sylvestre Maurice et al. "The SuperCam Instrument Suite on the Mars 2020 Rover: Science Objectives and Mast-Unit Description". In: *Space Science Reviews* 217.3 (2021). DOI: 10.1007/s11214-021-00807-w.

[47] Timothy A. Sipkens et al. "Laser-induced incandescence for non-soot nanoparticles: recent trends and current challenges". In: *Applied Physics B* 128.4 (2022). DOI: 10.1007/s00340-022-07769-z.

[48] Klaus P. Geigle et al. "Laser-induced incandescence for soot measurements in an aero-engine combustor at pressures up to 20 bar". In: *Applied Physics B* 125.6 (2019), p. 96. ISSN: 0946-2171. DOI: 10.1007/s00340-019-7211-2. URL: http://link.springer.com/10.1007/s00340-019-7211-2.

[49] Stephen Robinson-Enebeli, S. Talebi-Moghaddam, and K. J. Daun. "Time-Resolved Laser-Induced Incandescence Measurements on Aerosolized Nickel Nanoparticles". In: *The Journal of Physical Chemistry A* 125.28 (2021), pp. 6273–6285. DOI: 10.1021/acs.jpca.1c03558.

[50] Stefan Will and Klaus Peter Geigle. "Laser-induced incandescence". In: *Applied Physics B* 126.6 (2020). DOI: 10.1007/s00340-020-07461-0.

[51] Jérôme Yon et al. "Investigation of soot oxidation by coupling LII, SAXS and scattering measurements". In: *Combustion and Flame* 190 (2018), pp. 441–453. DOI: 10.1016/j.combustflame.2017.12.014.

[52] Hope A. Michelsen et al. "Laser-induced incandescence: Particulate diagnostics for combustion, atmospheric, and industrial applications". In: *Progress in Energy and Combustion Science* 51 (2015), pp. 2–48. ISSN: 03601285. DOI: 10.1016/j.pecs.2015.07.001. URL: https://linkinghub.elsevier.com/retrieve/pii/S0360128515300071.

[53] Elaine C. Cabral et al. "Pterodon pubescens Oil: Characterisation, Certification of Origin and Quality Control via Mass Spectrometry Fingerprinting Analysis". In: *Phytochemical Analysis* 24.2 (2012), pp. 184–192. DOI: 10.1002/pca.2404.

[54] Jasmin Tröstl et al. "Fast and precise measurement in the sub-20nm size range using a Scanning Mobility Particle Sizer". In: *Journal of Aerosol Science* 87 (2015), pp. 75–87. DOI: 10.1016/j.jaerosci.2015.04.001.

[55] Maura J. Sheehan et al. "Generation of Nanoparticles with a Nebulizer-Cyclone System". In: *Aerosol Science and Technology* 43.11 (2009), pp. 1091–1098. DOI: 10.1080/02786820903173687.

[56] Juan Fernández de la Mora. "The Fluid Dynamics of Taylor Cones". In: *Annual Review of Fluid Mechanics* 39.1 (2007), pp. 217–243. ISSN: 0066-4189. DOI: 10.1146/annurev.fluid.39.050905.110159.

[57] John B. Fenn et al. "Electrospray Ionization for Mass Spectrometry of Large Biomolecules". In: *Science* 246.4926 (1989), pp. 64–71. DOI: 10.1126/science.2675315.

[58] John B. Fenn et al. "Electrospray ionization-principles and practice". In: *Mass Spectrometry Reviews* 9.1 (1990), pp. 37–70. DOI: 10.1002/mas.1280090103.

[59] Paul Kebarle and Liang Tang. "From ions in solution to ions in the gas phase - the mechanism of electrospray mass spectrometry". In: *Analytical Chemistry* 65.22 (1993), 972A–986A. DOI: 10.1021/ac00070a001.

[60] Christopher Harris and Anthony J. Stace. "Coulomb Fission in Multiply-Charged Ammonia Clusters: Accurate Measurements of the Rayleigh Instability Limit from Fragmentation Patterns". In: *The Journal of Physical Chemistry A* 122.10 (2018), pp. 2634–2644. DOI: 10.1021/acs.jpca.8b00815.

[61] Christian Lübbert and Wolfgang Peukert. "Characterization of Electrospray Drop Size Distributions by Mobility-Classified Mass Spectrometry: Implications for Ion Clustering in Solution and Ion Formation Pathways". In: *Analytical Chemistry* 93.38 (2021), pp. 12862–12871. DOI: 10.1021/acs.analchem.1c00727.

[62] Zhenwei Wei et al. "Accelerated Reaction Kinetics in Microdroplets: Overview and Recent Developments". In: *Annual Review of Physical Chemistry* 71.1 (2020), pp. 31–51. DOI: 10.1146/annurev-physchem-121319-110654.

[63] Gary J. Van Berkel and Vilmos Kertesz. "Using the Electrochemistry of the Electrospray Ion Source". In: *Analytical Chemistry* 79.15 (2007), pp. 5510–5520. DOI: 10.1021/ac071944a.

[64] Paul Kebarle. "A brief overview of the present status of the mechanisms involved in electrospray mass spectrometry". In: *Journal of Mass Spectrometry* 35.7 (2000), p. 804. DOI: 10.1002/1096-9888(200007)35:7<804::AID-JMS22>3.3.CO;2-H.

[65] Alfonso M. Gañán-Calvo and José M. Montanero. "Revision of capillary cone-jet physics: Electrospray and flow focusing". In: *Physical Review E* 79.6 (2009), p. 066305. DOI: 10.1103/physreve.79.066305.

[66] Geoffrey I. Taylor. "Disintegration of water drops in an electric field". In: *Proceedings of the Royal Society of London. Series A. Mathematical and Physical Sciences* 280.1382 (1964), pp. 383–397. DOI: 10.1098/rspa.1964.0151.

[67] Piia Liigand et al. "The Evolution of Electrospray Generated Droplets is Not Affected by Ionization Mode". In: *Journal of the American Society for Mass Spectrometry* 28.10 (2017), pp. 2124–2131. DOI: 10.1007/s13361-017-1737-5.

[68] Christina M. Alymatiri, Maria G. Kouskoura, and Catherine K. Markopoulou. "Decoding the signal response of steroids in electrospray ionization mode (ESI-MS)". In: *Anal. Methods* 7.24 (2015), pp. 10433–10444. DOI: 10.1039/c5ay02839f.

[69] Frank Wiederschein et al. "Charge separation and isolation in strong water droplet impacts". In: *Physical Chemistry Chemical Physics* 17.10 (2015), pp. 6858–6864. DOI: 10.1039/C4CP05618C.

[70] Andreana Andreeva and Nikolay Zografov. "Oscillation mode and resonant frequencies of spherical pendant droplets". In: 2019, p. 160015. DOI: 10.1063/1.5091342. URL: http://aip.scitation.org/doi/abs/10.1063/1.5091342.

[71] David Porter. *Phase transformations in metals and alloys*. p. 306. Boca Raton, FL: CRC Press, 2009. ISBN: 9781439883570.

[72] Sarmistha Sarkar et al. "Composition dependent non-ideality in aqueous binary mixtures as a signature of avoided spinodal decomposition". In: *Journal of Chemical Sciences* 127.1 (2015), pp. 49–59. DOI: 10.1007/s12039-014-0749-y.

[73] Walter Kauzmann. "The Nature of the Glassy State and the Behavior of Liquids at Low Temperatures." In: *Chemical Reviews* 43.2 (1948), pp. 219–256. DOI: 10.1021/cr60135a002.

[74] Mats Hilding Hillert. "A theory of nucleation for solid metallic solutions". PhD thesis. Massachusetts Institute of Technology, 1956.

[75] William J. MacKnight and Frank E. Karasz. "Polymer Blends". In: *Comprehensive Polymer Science and Supplements*. Elsevier, 1989, pp. 111–130. DOI: 10.1016/b978-0-08-096701-1.00207-x.

[76] Perter W. Atkins. *Physical chemistry*. New York: W.H. Freeman and Co, 2010. ISBN: 9781429218122.

[77] Michal Duška. "Water above the spinodal". In: *The Journal of Chemical Physics* 152.17 (2020), p. 174501. DOI: 10.1063/5.0006431.

[78] Shiva Rudraraju, Anton Van der Ven, and Krishna Garikipati. "Mechanochemical spinodal decomposition: a phenomenological theory of phase transformations in multi-component, crystalline solids". In: *npj Computational Materials* 2.1 (2016). DOI: 10.1038/npjcompumats.2016.12.

[79] David M. Wieliczka, Shengshan Weng, and Marvin R. Querry. "Wedge shaped cell for highly absorbent liquids: infrared optical constants of water". In: *Applied Optics* 28.9 (May 1989), p. 1714. DOI: 10.1364/ao.28.001714.

[80] Leonid V. Zhigilei and Barbara J. Garrison. "Microscopic mechanisms of laser ablation of organic solids in the thermal and stress confinement irradiation regimes". In: *Journal of Applied Physics* 88.3 (2000), pp. 1281–1298. DOI: 10.1063/1.373816.

[81] Zhaoyang Chen and Akos Vertes. "Early plume expansion in atmospheric pressure midinfrared laser ablation of water-rich targets". In: *Physical Review E* 77.3 (2008), p. 036316. DOI: 10.1103/physreve.77.036316.

[82] Alfred Vogel and Vasan Venugopalan. *Mechanisms of pulsed laser ablation of biological tissues*. 2003. DOI: 10.1021/cr010379n.

[83] Klaus Dreisewerd. "The Desorption Process in MALDI". In: *Chemical Reviews* 103.2 (2003), pp. 395–426. DOI: 10.1021/cr010375i.

[84] Klaus Dreisewerd et al. "Fundamentals of matrix-assisted laser desorption/ionization mass spectrometry with pulsed infrared lasers". In: *International Journal of Mass Spectrometry* 226.1 (2003), pp. 189–209. DOI: 10.1016/s1387-3806(02)00977-6.

[85] José Villatoro et al. "IR-MALDI ion mobility spectrometry". In: *Analytical and Bioanalytical Chemistry* 408.23 (2016), pp. 6259–6268. DOI: 10.1007/s00216-016-9739-x.

[86] José Villatoro et al. "IR-MALDI ion mobility spectrometry: physical source characterization and application as HPLC detector". In: *International Journal for Ion Mobility Spectrometry* 19.4 (Dec. 2016), pp. 197–207. DOI: 10.1007/s12127-016-0208-1.

[87] Ingo Apitz and A. Vogel. "Material ejection in nanosecond Er:YAG laser ablation of water, liver, and skin". In: *Applied Physics A* 81.2 (July 2005), pp. 329–338. ISSN: 0947-8396. DOI: 10.1007/s00339-005-3213-5.

[88] Raphael D. Urban et al. "On-chip mass spectrometric analysis in non-polar solvents by liquid beam infrared matrix-assisted laser dispersion/ionization". In: *Analytical and Bioanalytical Chemistry* 413.6 (2021), pp. 1561–1570. DOI: 10.1007/s00216-020-03115-4.

[89] Erdmann Rapp et al. "Atmospheric Pressure Free Liquid Infrared MALDI Mass Spectrometry: Toward a combined ESI/MALDI-Liquid Chromatography Interface". In: *Analytical Chemistry* 81.1 (2008), pp. 443–452. DOI: 10.1021/ac801863p.

[90] Nikolai A. Fuchs. "On the stationary charge distribution on aerosol particles in a bipolar ionic atmosphere". In: *Geofisica Pura e Applicata* 56.1 (Sept. 1963), pp. 185–193. DOI: 10.1007/BF01993343.

[91] Ross Gunn. "Diffusion charging of atmospheric droplets by ions, and the resulting combination coefficients". In: *Journal of Meteorology* 11.5 (Oct. 1954), pp. 339–347. DOI: 10.1175/1520-0469(1954)011<0339:DCOADB>2.0.CO;2.

[92] Ross Gunn and R.H. Woessner. "Measurements of the systematic electrification of aerosols". In: *Journal of Colloid Science* 11.3 (June 1956), pp. 254–259. DOI: 10.1016/0095-8522(56)90050-2.

[93] Alfred Wiedensohler. "An approximation of the bipolar charge distribution for particles in the submicron size range". In: *Journal of Aerosol Science* 19.3 (1988), pp. 387–389. DOI: 10.1016/0021-8502(88)90278-9.

[94] Dylan H. Ross, Jang Ho Cho, and Libin Xu. "Breaking Down Structural Diversity for Comprehensive Prediction of Ion-Neutral Collision Cross Sections". In: *Analytical Chemistry* 92.6 (2020), pp. 4548–4557. DOI: 10.1021/acs.analchem.9b05772. (Visited on 02/11/2022).

[95] Gary A. Eiceman, Z. Karpas, and Herbert H. Hill Jr. *Ion Mobility Spectrometry*. CRC PR INC, Dec. 2013. 444 pp. ISBN: 1439859973.

[96] Glenn E. Spangler. "New Developments in ion mobility spectrometry". In: *Journal of Process Analytical Chemistry* (2001).

[97] Christoph Schaefer et al. "Ion Mobility Shift of Isotopologues in a High Kinetic Energy Ion Mobility Spectrometer (HiKE-IMS) at Elevated Effective Temperatures". In: *Journal of the American Society for Mass Spectrometry* 31.10 (2020), pp. 2093–2101. DOI: 10.1021/jasms.0c00220.

[98] Raquel Cumeras et al. "Review on Ion Mobility Spectrometry. Part 1: current instrumentation". In: *The Analyst* 140.5 (2015), pp. 1376–1390. DOI: 10.1039/c4an01100g.

[99] Raquel Cumeras et al. "Review on Ion Mobility Spectrometry. Part 2: hyphenated methods and effects of experimental parameters". In: *The Analyst* 140.5 (2015), pp. 1391–1410. DOI: 10.1039/c4an01101e.

[100] Yuri Alexeev, Dmitri G. Fedorov, and Alexandre A. Shvartsburg. "Effective Ion Mobility Calculations for Macromolecules by Scattering on Electron Clouds". In: *The Journal of Physical Chemistry A* 118.34 (2014), pp. 6763–6772. DOI: 10.1021/jp505012c.

[101] Ansgar T. Kirk, Christian-Robert Raddatz, and Stefan Zimmermann. "Separation of Isotopologues in Ultra-High-Resolution Ion Mobility Spectrometry". In: *Analytical Chemistry* 89.3 (Jan. 2017), pp. 1509–1515. DOI: 10.1021/acs.analchem.6b03300.

[102] Ansgar T. Kirk and Stefan Zimmermann. "Pushing a compact 15 cm long ultra-high resolution drift tube ion mobility spectrometer with R = 250 to R = 425 using peak deconvolution". In: *International Journal for Ion Mobility Spectrometry* 18.1-2 (2015), pp. 17–22. DOI: 10.1007/s12127-015-0166-z.

[103] Alexandre A. Shvartsburg et al. "Modeling ionic mobilities by scattering on electronic density isosurfaces: Application to silicon cluster anions". In: *The Journal of Chemical Physics* 112.10 (2000), pp. 4517–4526. DOI: 10.1063/1.481042.

[104] Alexandre A. Shvartsburg et al. "Evaluation of Ionic Mobilities by Coupling the Scattering on Atoms and on Electron Density". In: *The Journal of Physical Chemistry A* 104.26 (2000), pp. 6152–6157. DOI: 10.1021/jp0004765.

[105] Edward Mack. "AVERAGE CROSS-SECTIONAL AREAS OF MOLECULES BY GASEOUS DIFFUSION METHODS". In: *Journal of the American Chemical Society* 47.10 (1925), pp. 2468–2482. DOI: 10.1021/ja01687a007.

[106] Boris M Smirnov. "DIFFUSION AND MOBILITY OF IONS IN A GAS". In: *Soviet Physics Uspekhi* 10.3 (1967), pp. 313–331. DOI: 10.1070/pu1967v010n03abeh003249.

[107] Thomas Wyttenbach et al. "Effect of the long-range potential on ion mobility measurements". In: *Journal of the American Society for Mass Spectrometry* 8.3 (1997), pp. 275–282. DOI: 10.1016/s1044-0305(96)00236-x.

[108] Michael F. Mesleh et al. "Structural Information from Ion Mobility Measurements: Effects of the Long-Range Potential". In: *The Journal of Physical Chemistry* 100.40 (1996), pp. 16082–16086. DOI: 10.1021/jp961623v.

[109] Alexandre A. Shvartsburg and Martin F. Jarrold. "An exact hard-spheres scattering model for the mobilities of polyatomic ions". In: *Chemical Physics Letters* 261.1-2 (1996), pp. 86–91. DOI: 10.1016/0009-2614(96)00941-4.

[110] William C. Hinds. *Aerosol Technology 2e*. John Wiley Sons, Jan. 1999. 504 pp. ISBN: 0471194107.

[111] Lothar Gail, Udo Gommel, and Hans-Peter Hortig, eds. *Reinraumtechnik*. Springer Berlin Heidelberg, 2012. DOI: 10.1007/978-3-642-19435-1.

[112] José P. Santos et al. "Performance evaluation of a high-resolution parallel-plate differential mobility analyzer". In: *Atmospheric Chemistry and Physics* 9.7 (2009), pp. 2419–2429. DOI: 10.5194/acp-9-2419-2009.

[113] Luis J. Perez Lorenzo et al. "Instant acquisition of high resolution mobility spectra in a differential mobility analyzer with 100 independent ion collectors: Instrument calibration". In: *Aerosol Science and Technology* 54.10 (2020), pp. 1144–1156. DOI: 10.1080/02786826.2020.1760198.

[114] Mario Amo-González and Sergio Pérez. "Planar Differential Mobility Analyzer with a Resolving Power of 110". In: *Analytical Chemistry* 90.11 (2018), pp. 6735–6741. DOI: 10.1021/acs.analchem.8b00579.

[115] Wolfgang Winklmayr et al. "A new electromobility spectrometer for the measurement of aerosol size distributions in the size range from 1 to 1000 nm". In: *Journal of Aerosol Science* 22.3 (1991), pp. 289–296. DOI: 10.1016/s0021-8502(05)80007-2.

[116] Juan Fernandez de la Mora et al. "Fast high-resolution nanoDMA measurements with a 25 ms response time electrometer". In: *Aerosol Science and Technology* 51.6 (2017), pp. 724–734. DOI: 10.1080/02786826.2017.1296928.

[117] Christina Williamson et al. "Fast time response measurements of particle size distributions in the 3–60 nm size range with the nucleation mode aerosol size spectrometer". In: *Atmospheric Measurement Techniques* 11.6 (2018), pp. 3491–3509. DOI: 10.5194/amt-11-3491-2018.

[118] TSI. *Manual: Water-based condensation particle counter model 3788*. TSI Incorporated. 2013.

[119] Gibaek Kim et al. "Development of Aerosol-LIBS (Laser Induced Breakdown Spectroscopy) for Real-time Monitoring of Process-induced Particles". In: *Aerosol and Air Quality Research* 19.3 (2019), pp. 455–460. DOI: 10.4209/aaqr.2018.08.0312.

[120] Blair Thornton et al. "Development of a deep-sea laser-induced breakdown spectrometer for in situ multi-element chemical analysis". In: *Deep Sea Research Part I: Oceanographic Research Papers* 95 (2015), pp. 20–36. DOI: 10.1016/j.dsr.2014.10.006.

[121] NASA. *ChemCam for Scientists*. 2012. URL: https://mars.nasa.gov/msl/spacecraft/instruments/chemcam/for-scientists/ (visited on 02/11/2022).

[122] NASA. *SuperCam for Scientits*. 2020. URL: https://mars.nasa.gov/mars2020/spacecraft/instruments/supercam/for-scientists/ (visited on 02/11/2022).

[123] Steven Rehse. *What is LIBS?* 2020. URL: https://www.uwindsor.ca/people/rehse/299/libs (visited on 02/11/2022).

[124] quantumcomposers. *Laser Ablation – Peak Power and Energy Considerations*. 2022. URL: https://www.quantumcomposers.com/post/laser-ablation-peak-power-and-energy-considerations (visited on 02/11/2022).

[125] Alex Donges and Reinhard Noll. *Laser Measurement Technology*. Springer Berlin Heidelberg, 2015. DOI: 10.1007/978-3-662-43634-9.

[126] Bo Li et al. "Nanosecond laser-induced breakdown assisted by femtosecond laser pre-ionization in air: the effect on spatial resolution and continuous radiation". In: *The European Physical Journal Applied Physics* 92.2 (2020), p. 20701. DOI: 10.1051/epjap/2020200258.

[127] Beatrice Campanella et al. "Shock Waves in Laser-Induced Plasmas". In: *Atoms* 7.2 (2019), p. 57. DOI: 10.3390/atoms7020057.

[128] Rivie Krasniker, Valery Bulatov, and Israel Schechter. "Study of matrix effects in laser plasma spectroscopy by shock wave propagation". In: *Spectrochimica Acta Part B: Atomic Spectroscopy* 56.6 (2001), pp. 609–618. DOI: 10.1016/s0584-8547(01)00194-x.

[129] Naomi Murdoch et al. "Laser-induced breakdown spectroscopy acoustic testing of the Mars 2020 microphone". In: *Planetary and Space Science* 165 (2019), pp. 260–271. DOI: 10.1016/j.pss.2018.09.009.

[130] Lizhi Li et al. "A simplified spectrum standardization method for laser-induced breakdown spectroscopy measurements". In: *Journal of Analytical Atomic Spectrometry* 26.11 (2011), p. 2274. DOI: 10.1039/c1ja10194c.

[131] David Prochazka et al. "Triple-pulse LIBS: laser-induced breakdown spectroscopy signal enhancement by combination of pre-ablation and re-heating laser pulses". In: *Journal of Analytical Atomic Spectrometry* 35.2 (2020), pp. 293–300. DOI: 10.1039/c9ja00323a.

[132] Gang Xiong et al. "Phase-selective laser-induced breakdown spectroscopy of metal-oxide nanoparticle aerosols with secondary resonant excitation during flame synthesis". In: *Journal of Analytical Atomic Spectrometry* 31.2 (2016), pp. 482–491. DOI: 10.1039/C5JA00186B.

[133] Fabien Goulay, P. E. Schrader, and H. A. Michelsen. "Effect of the wavelength dependence of the emissivity on inferred soot temperatures measured by spectrally resolved laser-induced incandescence". In: *Applied Physics B* 100.3 (2010), pp. 655–663. DOI: 10.1007/s00340-010-4119-2.

List of figures

Declaration of authorship

I hereby declare that I have composed the presented doctoral thesis independently on my own and without any other resources than the ones indicated, that all thoughts taken directly or indirectly from external sources are properly denoted as such and that this doctoral thesis has not been submitted to any other academic institution.

Potsdam, 20th of April 2022

Christian Prüfert